NANOSCALE LIGHT FOCUSING AND IMAGING WITH NANO-OPTICAL DEVICES

A Dissertation

by

VIJAY MEENASHI SUNDARAM

Submitted to the Office of Graduate and Professional Studies of
Texas A&M University
in partial fulfillment of the requirements for the degree of

DOCTOR OF PHILOSOPHY

Chair of Committee,	Sy-Bor Wen
Committee Members,	Steve Suh
	Choongho Yu
	Chin Su
Head of Department,	Andreas A. Polycarpou

December 2014

Major Subject: Mechanical Engineering

Copyright 2014 Vijay Meenashi Sundaram

ABSTRACT

Energy transport analysis of micro/nano optics as well as their optimization to achieve high-throughput deep nanoscale patterning and microscopy is the goal of this study.

To understand the energy transport in nano-optical devices, the transient heating behavior of a commercial available nano-optical probe, NSOM, under pulsed laser operation is examined first. Based on the thermal analysis, it is observed that the major limitation of the NSOM probe under higher energy operation arises from the joule heating of its thin metal coating and the resulting thermal/mechanical damage during operation.

Based on the understanding, a diffraction-based micro-zone plate (MZP) optical probe suffers less from joule heating and with advantages of higher optical throughput as well as longer working distance is designed and constructed. The MZP is fabricated at the end face of an optical fiber with a micro-fabrication technique based on e-beam negative tone lift-off lithography on non-planar substrates. The fabricated MZP can achieve spot sizes ~ 0.7λ at a focus distance of ~ 6λ with an optical transport efficiency of 20 %, which is more than 3 orders higher than that of NSOM.

To further reduce the size of the focus spot to deep sub-wavelength scales and to eliminate metallic structures which can cause joule heating during high energy operation, two all-dielectric optical probes are then designed/constructed, namely, (a) solid immersion probe, and (b) scattering dielectric probe. Both dielectric probes focus light by combining more than one of the diffraction mechanisms associated with dielectric material (e.g., refraction, solid immersion, Mie and near-field Rayleigh scattering) to achieve deep nanoscale light focusing with minimum energy loss. The solid immersion optical probe is constructed with a ball lens and microsphere for macro to micro scale focusing with far field refraction and micro to mesocale focusing with solid immersion. The ball lens and the microsphere are stacked on an optical fiber for achieving the cascade focusing configuration. The solid

immersion probe can achieve a focus spot size of ~ 0.45λ/n (~ 0.3λ when n = 1.5) on a target in the near field of the surface of the microsphere when the light is radially polarized. To achieve an even smaller focal spot in the near field, the scattering dielectric optical probe combines the verified solid immersion probe with a nano-scatterer at its focal spot. Due to the near-field Rayleigh scattering, the nano scatterer can induce a deep nanoscale spot with a diameter comparable to the forward radius of curvature of the scatterer under radially polarized light. It is verified with full wave electrodynamics simulations that the resulting scattering optical probe can achieve a ~10 nm spot with an intensity enhancement of ~ 10^5, which can be valuable in all kinds of bio-detection as well as nano fabrications.

At the end of the Ph.D study, mechanisms for deep sub-wavelength imaging resolutions with microspheres, which is recently demonstrated in different groups, are identified with full wave electrodynamics simulations. It is found that the high spatial imaging resolution of microlenses can be attributed to refractive index of the microsphere which is placed on the target plane (i.e. solid immersion effect), refractive index of the base material of the target and polarization of the emitters.

DEDICATION

विध्या ददाथि विनयं विनयाध्यति पात्रतां |

पात्रत्वद्धनमप्नोति धनाद्धर्मं ततः सुखं ||

ACKNOWLEDGEMENTS

First and foremost, I would like to thank my committee chair Dr. Sy-Bor Wen, for his guidance and support throughout my Ph.d study. I would also like to thank my committee members Dr. Steve Suh, Dr. Choongho Yu, and Dr. Chin Su, for their guidance and helpful discussions.

I would like to thank my colleagues in the lab, Alok Soni, Yu Yang, Young Kyong Jo, Chien-Fan Chen and Joshua Bragg. A special thanks to Alok Soni whose thermoreflectance setup I used to study the transient thermal response of NSOM probes in chapter 3 of this dissertation.

Thanks also go to the research scientists and staff at the Materials Characterization facility and the Nanolab at TAMU for training and assisting me in using various equipment at these facilities. I would also like to acknowledge the supercomputing center at TAMU which I extensively used in conducting the various numerical simulations in this dissertation.

I would like to thank all my friends who have been an important part of my life at College Station.

Last and definitely the most, I would like to thank my mother, father and brother for their encouragement, support and patience throughout my Phd.

TABLE OF CONTENTS

Page

ABSTRACT ii

DEDICATION iv

ACKNOWLEDGEMENTS v

TABLE OF CONTENTS vi

LIST OF FIGURES viii

LIST OF TABLES xiii

1. INTRODUCTION 1

1.1 Laser 1
1.2 Nano-optic devices 1
1.3 Heating of nano-optic devices 3
1.4 Design and characterization of MZP optical probes 6
1.5 Design and characterization of dielectric optical probes 7
1.6 Analysis of imaging with microspheres 8
1.7 Scope of dissertation 8

2. THEORY AND BACKGROUND 10

2.1 Physical limit of resolution in far field imaging and focusing 10
2.2 Far-field focusing of light: radial and linear polarization 12
2.3 Near-field light focusing with evanescent waves 18

3. TRANSIENT TEMPERATURE RESPONSE OF NSOM PROBES 20

3.1 Introduction 20
3.2 Experimental set-up 21
3.3 Results and discussion 24
3.4 Summary 34

4. DESIGN AND CHARACTERIZATION OF MICRO-ZONE PLATE OPTICAL PROBES 36

4.1 Introduction 36
4.2 Design of micro-zone plate (MZP) 37
4.3 Methodology for fabrication of devices at the end faces of optical fibers 41
4.4 Fabrication of MZP optical probe 51
4.5 Light focusing with MZP Probe 53
4.6 Summary 57

5. DESIGN AND CHARACTERIZATION OF DIELECTRIC OPTICAL PROBES 59

Page

5.1 Introduction 59
5.2 Focusing with dielectric optics..60
5.3 Solid immersion probe 65
5.4 Scattering dielectric probe...73
5.5 Summary 82

6. ANALYSIS OF DEEP SUB-MICRON RESOLUTION IN MICROLENSES BASED IMAGING...84

6.1 Introduction 84
6.2 Theoretical analysis...85
6.3 Results and discussion..87
6.4 Summary 94

7. CONCLUSIONS AND FUTURE WORK 95

7.1 Conclusions 95
7.2 Future work 98

REFERENCES...99

APPENDIX 111

Scattering of light by dielectric spheres (Lorentz – Mie theory) 111
Experimental techniques for characterization of light focusing devices...................114

LIST OF FIGURES

Page

Figure 1: Schematic of optical fiber based nano-optic device integrated with a scanning probe microscopy system 5

Figure 2: Diffraction of light by a circular aperture resulting in Airy disc pattern on a screen [33] 10

Figure 3: Angular and lateral Rayleigh resolution limit [33] 11

Figure 4: Schematic of differences in light focusing with a lens when the incident light is (a) linearly polarized, or (b) radially polarized. 13

Figure 5: Electric field intensity distribution at the focus spot obtained by solving the Debye integral. (a),(b) show the line plots and intensity profiles for radial polarization and (c),(d) show the line plots and intensity profiles for linear polarization. The dotted red line indicates the profile for the longitudinal field in each case. 17

Figure 6: Schematic showing the generation of evanescent waves by total internal reflection. 19

Figure 7: Schematic of the experimental setup of nanosecond TRTR for transient temperature measurement of NSOM probes. 23

Figure 8: (a) Optical image of NSOM probe with reflective background, (b) optical image of the NSOM probe without reflective background (used in TR), and (c) thermoreflectance image of 150 nm apertured NSOM probe driven by 4 μs laser pulse with λ ~ 450 nm and E ~ 200 nJ. Arrows in the figure indicate some of the non-thermal fluctuations in recorded temperature due to non-smooth coating shown in the optical image. 24

Figure 9: (a) Transient temperature profile of 150 nm aperture NSOM probe driven by 4 μs laser pulse with λ ~ 450 nm and E ~ 200 nJ. (b) Temperature history at a fixed ~ 10 μm away from the tip under the same conditions indicating the different curve fits. 27

Figure 10: Transient temperature profiles of a 150 nm apertured NSOM probe driven by 4 μs laser pulse with λ ~ 450 nm, and (a) E = 100 nJ or (b) E = 300 nJ. The corresponding temperature histories at a fixed ~ 10 μm away from the tip are presented in (c) and (d) respectively. 29

Figure 11: (a) Transient temperature profiles of 150 nm aperture NSOM probe driven by 4 μs laser pulse with λ ~ 650 nm and E ~ 300 nJ. The corresponding temperature history at a fixed ~ 10 μm away from the tip is presented in (b). 30

Page

Figure 12: (a) Transient temperature profile of a 100 nm and a 150 nm apertured NSOM at the end of a 4 μs laser pulse with λ ~ 450 nm and E ~ 300 nJ. Temperature history of a 100 nm aperture NSOM probe at a fixed ~ 10 μm location away from the tip under the same laser conditions as part (a). 31

Figure 13: (a) Transient temperature profiles of 150 nm aperture NSOM probe driven by 5 ns laser pulse with λ ~ 450 nm and E ~ 100 nJ. The corresponding temperature history at a fixed ~ 10 μm away from the tip is presented in (b). 33

Figure 14: SEM images of the thermally damaged NSOM black spots on the gold thin film coating and small exfoliation of metal film around the aperture of the NSOM probe after ns laser experiments (Inset). 34

Figure 15: (a) Schematic showing the design of zone widths of MZP. (b) Schematic showing the focusing of light by the MZP. The length of the red arrows indicate the magnitude of the in-plane component of the spatial frequencies from the different zones. (c) Finite element simulation of light focusing with copper MZP consisting of 50 zones with a numerical aperture NA ~ 0.98. 39

Figure 16: Schematic of MZP fabricated at the end face of an optical fiber which can be mounted on the tuning fork of a scanning probe microscopy system for accurate positioning and scanning. 41

Figure 17: Schematic of fabrication process with PANI as the conducting layer. Reprinted with permission from [89]. 45

Figure 18: (a) Step 1: insert and fix an optical fiber in a ferrule with epoxy, Step 2: polish the end of the optical fiber with a sequence of 5 μm, 3 μm and 0.3 μm aluminum oxide lapping films and Step 3: mount the fiber-ferrule assembly to a ferrule holder during e-beam lithography. (b) Orthographic projection photos of fiber-ferrule assembly mounted in ferrule holder with extended length of optical fiber bent along the groove. 46

Figure 19: (a) Schematic showing edge bead formation during spin coating process on small area substrates. (b) Optical microscope images of edge bead formed by direct spin coating on optical fiber and removal of edge bead by spin coating on fiber-ferrule assembly with bevel edged ferrule. 48

Page

Figure 20: (a) Optical microscope image of polished optical fiber without coating. (b) First spin coated layer of 90 nm PMMA, (c) second spin coated layer of 100 nm PANI (on top of PMMA), (d) doped PANI, (e) third spin coated layer of 70 nm PMMA (on top of doped PANI) and (f) final spin coated layer of 30 nm HSQ (on top of PMMA). The smoothness and variation of the coating thickness of each layer is ~ 5 nm based on AFM measurement. 49

Figure 21: SEM image depicting undercut of the PMMA/PANI/PMMA trilayer after an etch time of (a) 60 s (b) 70 s (c) 80 s. 51

Figure 22: (a) Optical image of detached optical fiber with fabricated MZP (inset) corresponding SEM image. (b), (c), (d) SEM images of the fabricated MZP on the face of the optical fiber at different magnification ratios. 52

Figure 23: (a) Intensity distribution after passing through the MZP. (b) Intensity profile at the focal length (i.e. z = 3 μm) of the MZP. The FWHM obtained from simulation is ~ 300 nm. 54

Figure 24: Confocal image of 2D light intensity distribution at different focusing z planes of the MZP. 55

Figure 25: (a) NSOM images of light intensity distribution at different z planes after passing through the MZP (b) SEM image of MZP used for the NSOM images. 56

Figure 26: (a) NSOM images of light intensity distribution at different z planes after passing through the phase MZP (b) SEM image of phase MZP used for the NSOM after CHF3 etching and Fulton Dolan process. 57

Figure 27: (a) Focusing of light by refraction with a dielectric sphere. (b) Focusing of light by refraction and solid immersion with a dielectric microsphere of high refractive index. The size of the focus spot is reduces by a factor of n due to solid immersion. 61

Figure 28: (a) Schematic showing focusing of light by Mie scattering with a sphere. Mie scattering results obtained from Lorentz-Mie theory for scattering of light by a sphere of diameter (a) 10λ, (b) 8λ, and (c) 4λ. 63

Figure 29: Focusing of light by near-field Rayleigh scattering with dielectric nanospheres of different diameters when the polarization is (a) transverse and (b) longitudinal. The polarization direction is indicated in the figure with an arrow. 64

Figure 30: Schematic showing (a) focusing of a light ray by a cascade arrangement of two dielectric spheres used in the solid immersion probe and (b) the constructed solid-immersion probe on an optical fiber 67

Page

Figure 31: Simulated intensity distribution of light focusing by solid immersion probe. The intensity profile at the focus region is also shown. 68

Figure 32: Illustration showing the steps to be followed for mounting of the ball lens on the optical fiber. Step 1: The fiber is immersed in epoxy to generate an epoxy droplet at the end face. Step 2: The optical fiber with the epoxy droplet is centered on one of the microspheres with a precision translation stage. Step 3: The fiber comes in contact with the sphere which is grasped onto the fiber surface by the epoxy. 70

Figure 33: Illustration showing the steps to be followed for generation of the photopolymer pedestal structure. Step 1: The fiber with the ball lens is immersed into the epoxy and made to contact the silicon wafer at the bottom. Step 2: The fiber is retracted with a precision z-translation stage to ~ 5-6 μm which corresponds to the height of the photopolymer structure to be generated. UV light is coupled to the optical fiber to generate the structure. Step 3: The fiber is retracted from the solution and cleaned to remove excess uncured epoxy. 71

Figure 34: (a) Schematic of solid immersion probe. (b) Intensity distribution of light of wavelength λ ~ 450 nm focused by the solid immersion probe obtained from CLSM (confocal laser scanning microscope). (c) SEM image of the fabricated solid immersion probe. 72

Figure 35: Plot of electric field intensity distribution of a spherical scatterer with a radius= 30 nm. Reprinted with permission from [111].. 76

Figure 36: (a) Schematic of snowman configuration of scatterer (b) Schematic of teardrop configuration indicating th tapering angle. (c) Plot of electric field intensity of snowman scatterer with top sphere radius 10 nm and bottom 500 nm. (d) Plot of electric field intensity of teardrop scatterer with top sphere radius 10 nm and bottom 500 nm and tapering angle of 145° Reprinted with permission from [111].. 79

Figure 37: (a) Plot of electric field intensity distribution for cascade focusing configuration consisting of the teardrop scatterer placed at the focus region of 5 μm diameter microsphere (b) Schematic of scattering dielelctric probe that combines a tear drop scatterer with a solid-immersion probe. Reprinted with permission from [111]. 82

Figure 38: (a) Schematic of the simulation domain consisting of the target, microsphere and lens pair. Light intensity (~ $|E|^2$) distribution induced by (b) a transverse dipole (x-y dipole), and (c) a longitudinal dipole (z-dipole), in air with a microlens of diameter ~ 6 μm and refractive index n = 1.4. The dashed lines indicates the imaging plane 86

Page

Figure 39 : Light intensity distribution at the image plane of (a) a transverse dipole (i.e., x-y dipole) and (b) a longitudinal dipole (i.e., z dipole) 88

Figure 40: (a) Phase plot of x component of electric field when focused light (NA ~ 0.7) is incident on a gold thin film nanostructure with a width ~ 0.2 λ and thickness ~ 30 nm. (b) Phase plot of z component of electric field when focused light (NA ~ 0.7) is incident on an elongated gold nanostructure with a width ~ 0.1 λ and thickness ~ λ. 93

Figure 41: Schematic of experimental setup for characterization of light focusing by MZP probe with confocal laser scanning microscopy. 114

Figure 42: Schematic of experimental setup for characterization of light focusing by MZP probe with collection mode NSOM imaging. 116

LIST OF TABLES

Page

Table 1: Comparison of focal spot size by lenses for radial and linearly polarized illumination 16

Table 2: Scattering from dielectric spheres. 75

Table 3: Scattering from snowman scatterers with different bottom sphere radii. 78

Table 4: Scattering from snowman scatterers with different top sphere radii. 78

Table 5: Scattering from teardrop scatterer with different taper angles 81

Table 6: Simulated FWHM of the PSF, magnification M, and the dipole resolution at the imaging plane of the microsphere based imaging system for different refractive index of the microsphere 88

Table 7: Simulated FWHM of the PSF, magnification M, and the dipole resolution at the imaging plane of the microsphere based imaging system when the transverse point dipole is placed on different targets 89

Table 8: Simulated FWHM of the PSF, magnification M, and the dipole resolution at the imaging plane of the microsphere based imaging system when the longitudinal point dipole is placed on different targets 91

Table 9: Simulated FWHM of the PSF at the imaging plane of the microlens of refractive index n = 1.4 for transverse dipoles of different sizes 93

1. INTRODUCTION

1.1 Laser

Light Amplification by Stimulated Emission of Radiation (Laser) is a class of devices that emit coherent and monochromatic radiation at frequencies in the infrared, visible or ultraviolet regions of the electromagnetic spectrum. The emitted laser light is a low divergence beam that can be directed with active and passive optical devices.

The basic laser structure consists of three main components, namely, (a) an active medium consisting of a collection of atoms, molecules or ions, (b) a pumping source that pumps energy into the medium to excite these atoms into higher energy levels, and (c) an optical resonator consisting of two highly reflecting mirrors that bounce the laser beam back and forth repeatedly through an active medium. The pump source could be a flash-lamp, a gas discharge, or an electrical current source. Depending on the nature of the active medium and the amplification process, lasers can be classified as gas lasers, chemical lasers, excimer lasers, solid state lasers and semiconductor lasers. The output of laser can be continuous constant amplitude light (known as continuous wave lasers) or pulsed light (known as pulsed lasers). Continuous wave lasers are used in a variety of applications like laser printing, bar-code reading, microscopy, flow diagnostics etc. However for applications that require controlled deposition of intense laser energy in a very short time, pulsed lasers are preferred. The pulsed operation is achieved with techniques like q-switching, mode locking or gain switching and leads to much higher peak powers. Some of the applications of pulsed lasers include laser machining (i.e. laser cutting and laser drilling), material processing, laser surgery and fast/ultrafast imaging.

1.2 Nano-optic devices

With the recent advances in nanotechnology, there arises a need to extend the science and technology of laser applications to nanoscales. The primary requirement to achieve this goal is to confine laser light to a nanoscale spot. However, when the laser light is focused

in the far-field with the traditional reflective or refractive optics, the minimum achievable size of the laser spot in air is determined by diffraction and is > ~ λ/2. Hence, traditional far-field optics cannot be applied in nano-science and nano-engineering applications requiring < 10-100 nm spatial resolution. New optical device that can confine light to sub-diffraction limit spot sizes have to be developed to improve the spatial resolution of well-established optical based detection, fabrication and manipulation. These improved optical based detection/fabrication methods, compared with competing methods that use electron/ion beams and x-ray, have advantages in low operating cost, no need of a vacuum conditions, and better versatility in operating conditions.

To achieve a spot size with diameter less than ~λ/2 (i.e. smaller than the far-field diffraction limit), evanescent field in addition to propagation field should be included in light focusing. Optical devices utilizing evanescent field to achieve the nanoscale confinement have been developed for more than ten years and are categorized as nano-optical devices [1]. Nanoscale light confinement in nano-optic devices is traditionally achieved through three main mechanisms, namely (a) light leakage from a sub-diffraction limit aperture (b) light scattering by a metallic nanostructure, and (c) surface plasmons. Apertured near-field scanning optical microscope (NSOM) is an example of nano-optic devices that uses the first mechanism to confine light through light leakage from a 50-200 nm aperture [2]. Maskless nanoscale lithography and direct surface machining with apertured NSOM probes have been demonstrated [3-14]. With deep sub-wavelength light confinement at the tip, patterns/structures with 50-150 nm spatial resolution can be fabricated/imaged with NSOM probes. Examples of nano-optic devices that use the second mechanism are apertureless NSOM and optical antennas which confine light through local field enhancement in the near-field of nanostructures (such as metallic tips, nanospheres or nano-rods). The local field enhancement in the near-field is caused by oscillation of electrons in the nanoscale confined structure when modulated by an external field [15, 16]. Dot and line patterns with ~10-50 nm width have been generated with apertureless NSOM probes (i.e., a sharp atomic force microscope tip) when the probe is irradiated

with femtosecond laser [17-19]. Devices that use the third mechanism for light confinement are named as plasmonic lenses [20, 21]. In plasmonic lenses, surface plasmons are excited and focused to achieve a nanoscale spot [22]. Since the wavelength of the surface plasmon is smaller than that of the incident light, focused spot sizes smaller than the far-field diffraction limit can be achieved. Plasmonic lenses consisting of single and multiple concentric slits on metal thin films have been demonstrated to generate 80 nm patterns on thermal photoresists [23, 24].

All the light focusing devices discussed above suffer from three major limitations namely, (a) vulnerability to high energy operation, (b) low optical throughput and (c) low working distance. The first limitation arises from the heavy use of metallic structures to achieve light confinement, which leads to dissipation of optical energy during transport and the resulting strong joule heating which can thermally damage the device. The second limitation arises due to the mechanism that is applied to generate the high resolution evanescent fields. For example in aperture NSOM probes the evanescent waves are generated by blocking the propagation of different waveguide modes, by tapering the optical fibers. The tapered optical fiber is surrounded by a metal thin film coating which absorbs most of the incident light resulting in a net optical throughput of ~ 10^{-4} %. The third limitation arises from the utilization of the evanescent field for nanoscale confinement since evanescent waves achieve high spatial resolution at the expense of an exponentially decaying field in the direction of propagation (i.e away from the surface of the nano-optic device). As a result of the exponentially decaying nature of the evanescent field, a working distance of the order of ~ 10-20 nm from the nano-optic device is required to have sufficient signal to noise ratio in both fabrication and detection applications.

1.3 Heating of nano-optic devices

Among the three problems discussed above, vulnerability to high energy operation remains the most limiting factor in the application of nano-optic devices in nanoscale direct machining applications. While it is known that the joule heating of the metallic

structures of the nano-optic device is the main reason for the damage, the possible mechanisms that cause the damage as a result of joule heating such as thermal expansion, induced themal stresses and melting are still under debate. A detailed study of the optical energy transport in nano-optic devices and the associated heat transfer mechanisms that occur can provide useful information for the future design of nano-optic devices that are better resistant to thermal damage and better suited for pulsed laser operation.

Among the different nano-optic devices, NSOM probes are the most commonly used and the only commercially available devices that can achieve nanoscale confinement of light. NSOM probes have been successfully applied for microscopy and nano-patterning applications [25]. However, the problems of joule heating and vulnerability to high energy operations have been reported for the NSOM probes particularly when coupled with pulsed/high power laser sources. The damage of the NSOM probe has been mainly observed to occur at the tip region when used in nano-patterning with pulsed lasers [26-28]. In this study, we chose the NSOM probe as our nano-optic device and try to further understand the factors that cause thermal damage of device by studying the transient thermal response of the NSOM probe under pulsed laser illumination.

In the first part of this dissertation a non-contact transient temperature measurement technique based on thermoreflectance is used to experimentally examine the transient thermal response of the NSOM probes coupled with a pulsed laser sources. The dominant heat transfer mechanisms in the heating and cooling of the NSOM probes coupled with pulsed laser as functions of laser energy, wavelength, pulse duration and probe geometry are inferred from the measured transient temperature profiles. The results obtained in this first part of the dissertation give a better physical picture of the laser-thermal energy conversion and thermal transport mechanisms in NSOM probes as well as the origin of thermal damage of the NSOM probe when coupled with pulsed (ns and μs) lasers.

Based on the conclusions from the transient thermal analysis of NSOM probes, in the following part of this research, we wish to relieve some of the limitations discussed above by designing new micro/nano-optic devices that are better suited for high energy pulsed operation. In addition, the designed devices are incorporated as probe based micro/nano-optics i.e. the micro/nano-optic devices are fabricated/mounted at the end faces of optical fibers. The optical fiber based devices (referred to as optical probes) can then be mounted directly onto traditional scanning probe microscopy systems to achieve precise control of positioning which is important in the application of nano-optic devices in fabrication and detection (Figure 1) [29].

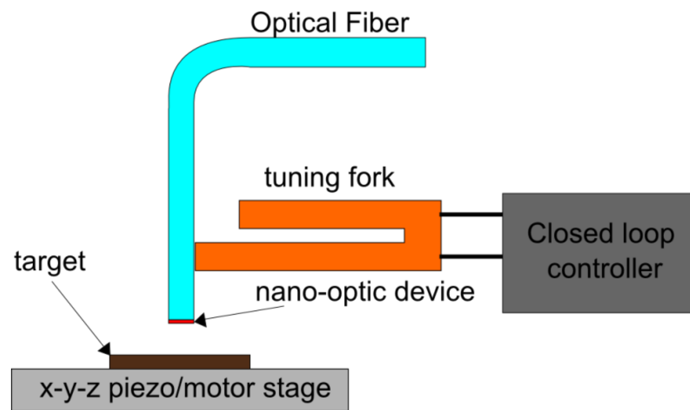

Figure 1: Schematic of optical fiber based nano-optic device integrated with a scanning probe microscopy system

Three new optical probes capable of sub-micron and nanoscale resolution are investigated. The first probe, a micro-zone plate (MZP), confines light to a focus spot by constructive interference of waves passing through concentric transparent and opaque rings. The MZP is composed of metallic nanostructures and can achieve submicron focusing in the far field (i.e. focal length ~ 10s λ) without evanescent waves and with high transport efficiency (~ 20 %). The second probe is a solid immersion probe that achieves deep subwavelength resolution based on cascade focusing with refraction and solid immersion. The third probe

is a scattering based dielectric optical probe consisting of dielectric reflecting and scattering elements that can achieve nanoscale resolution in the near-field. The scattering probe is fully composed with dielectric material resulting in negligible joule heating.

1.4 Design and characterization of MZP optical probes

Super-oscillatory localizations of light generated by binary phase lenses have been demonstrated as potential mechanisms for near/sub diffraction limit light confinement [30]. Super-oscillations based light confinement results from super-positions of optical waves of different spatial frequencies and amplitudes forming arbitrarily small spatial localizations that occur far away from the source without the need for evanescent waves. Compared with NSOM probes super oscillation based lenses can achieve higher optical throughput and long working distances of the order of ~ 10λ. The first probe examined in this study is a binary phase plate based super oscillation lens consisting of transparent and opaque zones named micro-zone plate (MZP). The MZP designed in this study has a numerical aperture ~ 0.98 and a near-diffraction limit focus. Compared with the traditional super-oscillation lens, the optical throughput of the MZP is very high (due to the diffraction limited focus) with a focus intensity of ~ 100 times that of the incident light. In addition the focus spot does not have significant side lobes. The MZP is fabricated on an optical fiber that can be subsequently mounted in a scanning probe microscopy system to achieve accurate positioning and fast scanning.

A new fabrication method based on electron beam lithography (EBL) is developed for high accuracy, high precision fabrication of MZP structures at the end face of the optical fiber. The focusing capability of the fabricated MZP at the end of the optical fiber is experimentally measured with two different methods namely collection mode NSOM scanning and confocal laser scanning which provide the light intensity profiles at each imaging plane in parallel to the surface of the MZP. The experimentally determined focal lengths and focus spot sizes agree well with full wave numerical finite element

simulations. The developed method is also extended for the fabrication of phase-MZP which consists only of dielectric material.

While the MZP provides long working distance and sub-micron localization of light with high optical throughput, it is composed primarily of metallic structures which undergo joule heating during high intensity operation thereby limiting its application. In addition, the MZP is not suitable for sub 50 -150 nm nanoscale light focusing when coupled with UV/visible light since it does not make use of evanescent waves. In some applications such as nanoscale scanning microscopy and direct fabrication, a high energy throughput probe with sub 50-150 nm spatial resolution that does not suffer from problems of joule heating is desired. In the next part of this study we design all-dielectric optical probes that can achieve nanoscale resolution.

1.5 Design and characterization of dielectric optical probes

Dielectric microspheres of radius much larger than the wavelength of incident light act as a spherical microlenses when illuminated with linearly polarized plane waves resulting in a high intensity focus spots of size ~ 0.6λ/NA due to refraction [31, 32]. By increasing the refractive index or reducing the radius of the dielectric sphere to 2-3λ , the focus spot can be shifted closer to the surface of the sphere resulting in smaller focus spot sizes due to larger NA. When the plane wave is replaced with a focused beam (such as Gaussian or Bessel beam) with the focus location around the outer edge of the microsphere, the size of the focus spot is further reduced due to solid immersion effect (resulting in NA > 1). When the radius of the sphere is comparable or less than the wavelength of the incident light, confinement of light occurs due to scattering resulting in spot sizes in the sub-100 nm scales i.e. much smaller than the far-field diffraction limit.

In this part of the study, we design optical probes that achieve nanoscale confinement by focusing of the incident light with dielectric microlenses based on a combination of reflection, solid immersion and scattering effects. Two types of optical probes are

investigated, namely, (a) solid immersion probe based on high energy throughput cascade focusing with solid immersion effect, and (b) Scattering dielectric optical probe based on high energy throughput and high spatial resolution focusing with near-field Rayleigh scattering from nanostructures. The all-dielectric material composition of the probes makes them ideal candidates for high energy throughput fabrication and microscopy applications with negligible joule heating.

1.6 Analysis of imaging with microspheres

The deep sub-micron focusing resolution achieved with dielectric spheres with mechanisms such as solid immersion and near-field scattering described in the previous paragraph can be extended to imaging based on the reciprocity of linear optics. The application of dielectric microspheres in high resolution imaging has drawn significant attention in the recent years. Better than ~ $\lambda/4$ spatial resolution in imaging has been achieved by different groups with microspheres placed on the target plane and a high numerical objective lenses placed in the imaging path of the microsphere to magnify the virtual/real images generated by the microsphere. In the final part of this dissertation, we conduct numerical experiments to identify the contribution of each mechanism, namely, refractive index of the microsphere, refractive index of the base material of the target, and the polarization direction of emitted light on the deep sub-micron scale imaging with microsphere. The results from the numerical simulations are used to explain the high imaging resolution reported in the experimental observations.

1.7 Scope of dissertation

In Chapter 2, a theoretical background on the classical diffraction limit, far field and near field focusing of light along with the effect of polarization on light focusing is provided.

In Chapter 3, transient temperature response of NSOM probe under pulsed laser operation is studied with thermoreflectance method. The dominant heat transfer mechanisms in the heating and cooling of the NSOM probes coupled with pulsed laser as functions of laser

energy, wavelength, pulse duration and probe geometry are inferred from the measured transient temperature profiles. The origin of thermal damage of the NSOM probe when coupled with pulsed (ns and μs) lasers is analyzed and can be used as an input to design new nano-optic devices that can withstand high energy pulsed operation.

In Chapter 4, a micro-zone plate (MZP) optical probe is designed and fabricated. The fabrication of MZP probe is done with a newly developed method based on electron beam lithography that enables accurate fabrication of nanostructures on small area insulating substrates such as optical fibers. The focusing characteristics of the fabricated MZPs are experimentally verified and compared with results from full wave electromagnetic numerical simulations.

In Chapter 5, two all-dielectric optical probes based on the solid immersion effect and nanostructure scattering of light with dielectric microspheres are designed and fabricated. While the solid immersion probe has a resolution limit ~ 0.3λ, the scattering probes can focus light to ~ 10's nm spot sizes. Compared with NSOM probes, both probes have extremely high optical throughput and negligible joule heating due to the absence of metallic structures.

In Chapter 6, numerical simulations based on finite element method are applied to study the mechanisms of deep sub-wavelength imaging resolution with microspheres when the microsphere is placed in contact with the imaging target. The contribution of the target on imaging resolution is studied. The results from the numerical simulations are used to explain the high imaging resolution reported in previous imaging experiments.

In Chapter 7, a conclusion to the contributions of the current work is presented along with a discussion of potential future research directions.

2. THEORY AND BACKGROUND

2.1 Physical limit of resolution in far field imaging and focusing

To determine the classical resolution limit we first begin by studying the diffraction of light through a circular aperture. In a typical arrangement, plane waves are diffracted by a circular aperture Σ to the far-field resulting in a diffraction pattern observed on a screen σ (Figure 2). The circular aperture can also be replaced with a focusing lens, the function of which is to bring σ closer to Σ without changing the diffraction pattern. The intensity distribution of the diffraction pattern formed on the screen σ by a circular aperture of radius 'a' can be obtained by solving the Fraunhofer diffraction integral as

$$I = I(0)\underbrace{\left[\frac{2J_1(kaq/R)}{kaq/R}\right]}_{\text{Airy function}}, \tag{1}$$

where J_1 is the Bessel function of the first kind of order 1, k is the wave number and a, q and R are geometric parameters indicated in Figure 2. The intensity distribution has an axial symmetry with a central peak known as the Airy disc surrounded by lower intensity rings. The radius of the Airy disc is given by the first zero of the Bessel function as

$$\frac{kaq}{R} = 3.83 \Rightarrow q_1 = 1.22\frac{R\lambda}{2a}, \tag{2}$$

where λ is the wavelength of the incident light.

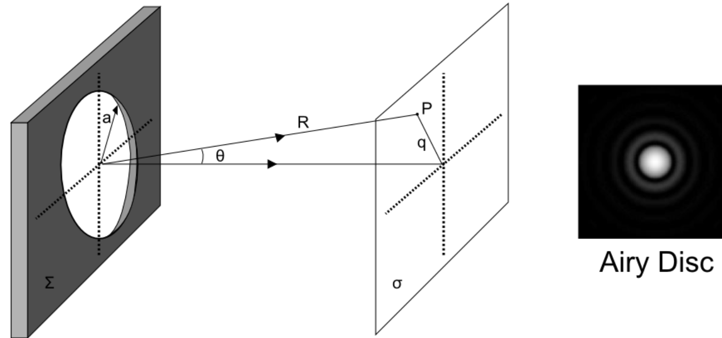

Figure 2: Diffraction of light by a circular aperture resulting in Airy disc pattern on a screen [33]

Now, the aperture is replaced by an imaging system such as a lens which diffracts the light emitted by an object and generates an image of an object on the screen σ. Each point in the object can be treated as a point source. The image of a point source formed by an aberration-free aperture or converging lens is not a point but rather a diffraction pattern known as the point spread function (PSF). When two points on the source in the object plane are close enough such that the center of the PSF (i.e Airy disc for a circular aperture or lens) of one point source on the screen σ coincides with the first minimum of the PSF of the second point source, the two points can be just resolved. This criterion is known as the Rayleigh resolution criterion and is illustrated in Figure 3. For the case of a circular aperture or lens, the expression for Rayleigh resolution limit can be derived from equation 2 by replacing *a/R* with sin(ϕ) where the angle ϕ is shown in Figure 3 as

$$(\Delta l)_{\min} = 0.61 \frac{\lambda}{\mathrm{n} \sin \phi} = 0.61 \frac{\lambda}{NA} , \tag{3}$$

where *n* is the refractive index of the medium in which the light is focused and NA stands for numerical aperture of the lens given by $NA = \mathrm{n} \sin \phi$.

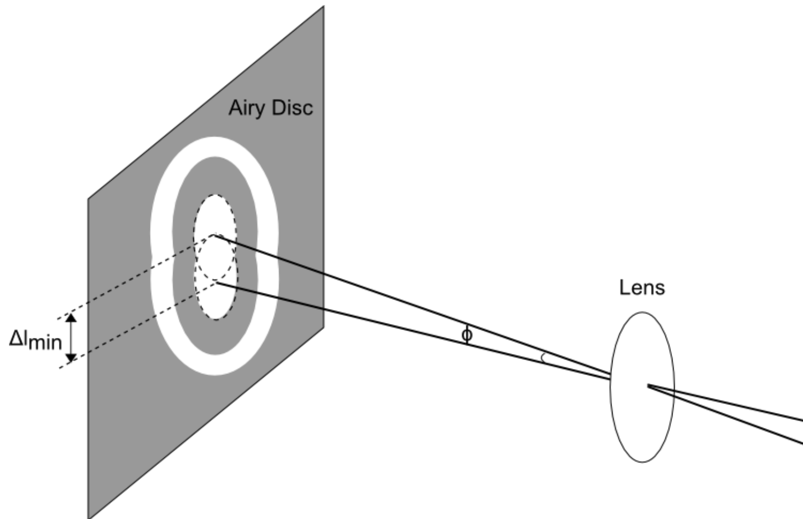

Figure 3: Angular and lateral Rayleigh resolution limit [33]

While the Rayleigh resolution criterion is the most commonly used one for determining the spatial resolution of an imaging system, there are other resolution criteria which can result in slightly different resolution limit. Here we present two other criteria that are also commonly used, namely Sparrow resolution criterion and Houston resolution criterion [34, 35]. The Sparrow resolution criterion states that two point sources are just resolved when the separation between the objects is such that the second derivative of the composite PSF of both objects just vanishes at the peak i.e. $\frac{\partial^2 I}{\partial x^2} = 0$. In other words, Sparrows limit arises when the saddle point in the composite PSF juts develops. The general expression for Sparrow criterion for a circular aperture (i.e. Airy diffraction pattern) is:

$$(\Delta l)_{\min} = 0.47 \frac{\lambda}{NA}. \tag{4}$$

Houston resolution criterion states that two point sources are just resolved when the distance between the central peaks of the PSFs of the two objects is equal to the full width at half maximum (FWHM) of each PSF. For the case of a circular aperture the Houston resolution criterion is given by

$$(\Delta l)_{\min} = 0.52 \frac{\lambda}{NA}. \tag{5}$$

Note that the FWHM of the PSF can be used to determine the size of the focus spot based on the principle of optical reciprocity [36]. Therefore, when using traditional refractive/reflective optics to focus light in the far-field, the smallest focus spot that can be achieved as well as the best imaging resolution that is obtainable is ~ $\lambda/2$.

The expressions for focus spot size (or imaging resolution) discussed above are derived with scalar diffraction theory by making paraxial approximations. In the next section, we consider the polarization effects of light on the focus spot size.

2.2 Far-field focusing of light: radial and linear polarization

In section 2.1 we determined the expression for diffraction limit which gives the smallest focus spot size that can be obtained with a lens in the far-field. However, the expression in equation 1 is obtained from scalar diffraction theory based on the paraxial and cannot

be applied for focusing with high numerical aperture optics in which the angle θ in eq 1 is large. In addition, the scalar theory does not consider the vectorial properties of light such as polarization of emission from the point source which influence the size as well as shape of the focal spot. In this section, we use a semi-analytical approach to determine the focus spot size that can be applied for high numerical aperture optics as well as light of different polarizations.

When light is focused with high numerical aperture optics (NA > 0.9) such as microlenses, the polarization of the incident light affects the intensity distribution at the focal region [37]. A semi-analytical vector diffraction integral known as the Debye integral can be used to calculate the theoretical intensity distribution (and hence the focus spot size) at the focal region of high numerical aperture optics with different polarizations. Before the theoretical calculations, we use simple illustrations to show the differences in the focusing effects of linear and radially polarized light rays with high numerical aperture optics.

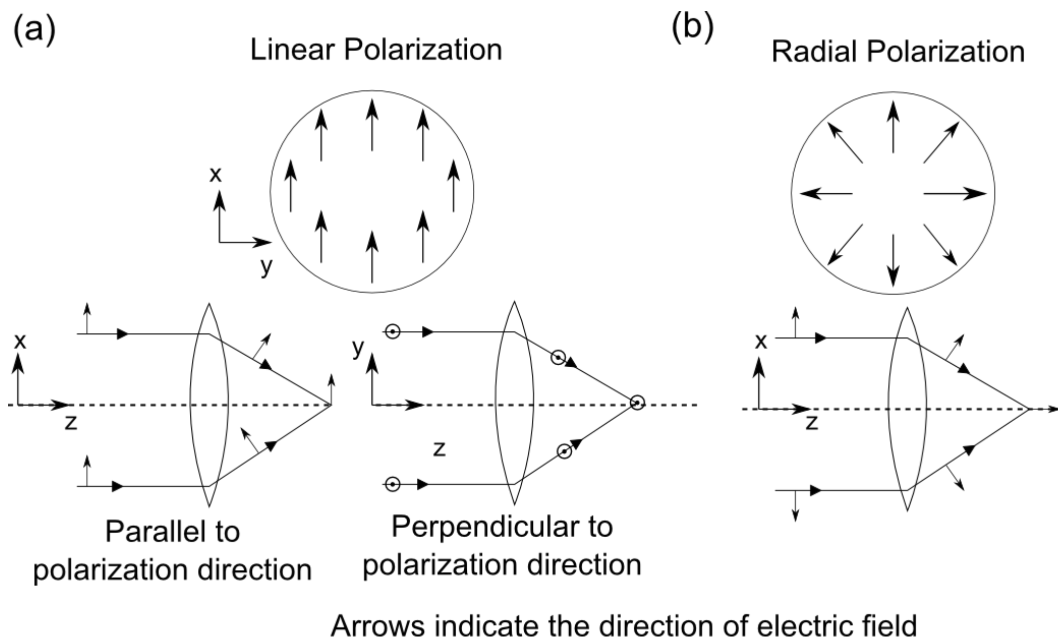

Figure 4: Schematic of differences in light focusing with a lens when the incident light is (a) linearly polarized, or (b) radially polarized.

The area of the focus spot for radially polarized light is smaller and exhibits rotational symmetry while that for linear polarization is larger and not rotationally symmetric. To understand this effect, consider a collimated beam of linearly and radially polarized light waves focused by a lens as shown in Figure 4a and Figure 4b respectively. For light rays propagating in the plane containing the optical axis and perpendicular to the direction of linear polarization (i.e yz plane), the electric field vectors add up at the focus (Figure 4a). On the other hand, for the plane that is parallel to the direction of linear polarization (i.e xz plane in the figure) and containing the optical axis, part of the electric field vectors cancel out at the focus. As a result the intensity distribution at the focus is non-rotationally symmetric. For the case of the radial polarization, the electric field vectors add up in all the planes containing the optical axis resulting in an axially symmetric focus spot (Figure 4b). In addition, the focus area has a strong axial component (or longitudinal component) of the electric field (particularly at high numerical apertures) which results in a much smaller spot size than that predicted by scalar diffraction theory. The exact focal spot size for linear and radial polarization can be express with Debye integral [38] as follows.

Consider a collimated polarized light beam incident on an aplanatic lens that produces a converging spherical wave at the focus of the lens. To obtain the field distribution at the focus the spherical wave at the exit pupil of the lens is decomposed into an angular spectrum of plane waves. The Debye approximation states that only those plane waves which have propagation vectors that fall within the geometric cone determined by the numerical aperture of the lens contribute to the field distribution at the focus. The Debye approximation also neglects the diffraction effects that occur at the edges of the lens. The superposition of these plane waves at the focus, while keeping track of the phase and polarization direction, is given by the Debye integral as [39]

$$\vec{E}(\vec{r}_2) = -\frac{i}{2\pi}\iint_{\Omega} dk_x dk_y \frac{\vec{A}(k_x,k_y)}{k_z}\exp(i\vec{k}.(\vec{r}_2-\vec{r}_1)) \ , \tag{6}$$

where the subscript 2 denotes the focal plane coordinates, subscript 1 denotes the aperture plane (exit pupil of the lens) coordinates. $\vec{A}(k_x,k_y)$ denotes the angular spectrum of plane waves at the aperture plane.

Without going into the details, the Debye integrals of field distribution at the focus of the lens for linear and radial polarized incident light are shown below.
For linearly polarized light [40],

$$E(r,\theta) = -ik\begin{pmatrix} I_0 + I_2\cos(2\theta) \\ I_2\sin(2\theta) \\ -2iI_1\cos(\theta) \end{pmatrix}, \tag{7}$$

where

$$\begin{aligned} I_0 &= \int_0^\alpha \sqrt{\cos\phi}\,\sin\phi\left(\cos\phi+1\right)J_0(kr\sin\phi)\,\mathrm{d}\phi, \\ I_1 &= \int_0^\alpha \sqrt{\cos\phi}\,\sin^2\phi J_1(kr\sin\phi)\,\mathrm{d}\phi, \\ I_2 &= \int_0^\alpha \sqrt{\cos\phi}\,\sin\phi\left(\cos\phi-1\right)J_2(kr\sin\phi)\,\mathrm{d}\phi, \end{aligned} \tag{8}$$

For radially polarized light,

$$E(r,\theta) = -ik\int_0^\alpha \sqrt{\cos\phi}\,\sin\phi\begin{pmatrix} i\cos\phi J_1(kr\sin\phi)\cos\theta \\ i\cos\phi J_1(kr\sin\phi)\sin\theta \\ \sin\phi J_0(kr\sin\phi) \end{pmatrix} d\phi\ , \tag{9}$$

where $J_0(x), J_1(x)$ and $J_2(x)$ denote the Bessel functions of the first kind of order 0,1 and 2 respectively. r,θ and ϕ are the spherical coordinates centered at the focus. Note that, in the above two equations 7 and 9, the limit of integration α denotes the semi-angle of convergence of the lens and is related to the numerical aperture NA as $NA = \sin\alpha$.

Table 1: Comparison of focal spot size by lenses for radial and linearly polarized illumination

Numerical Aperture	**Polarization**	**Intensity components**	**Full Width at Half Maximum (FWHM)**
NA = 1.0	Radial Polarization	Transverse and Longitudinal	0.5λ
		Longitudinal	0.43λ
	Linear Polarization (plane of polarization)	Transverse and Longitudinal	0.6λ
	Linear Polarization (perpendicular to plane of polarization)	Transverse and Longitudinal	0.52 λ
NA = 0.9	Radial Polarization	Transverse and Longitudinal	0.76λ
		Longitudinal	0.5λ
	Linear Polarization (plane of polarization)	Transverse and Longitudinal	0.65λ

Table 1 lists the spot sizes of the electric field intensity at the focus spot denoted by $\left|\vec{E}\right|^2$ as well as the spot sizes of the transverse field intensity $\left|\vec{E}_z\right|^2$ for NA = 0.9 and NA = 1.0 obtained from the Debye integral. Note that the spot size is defined as the full width at half maximum (FWHM) of the intensity distribution (Houston resolution criterion). In addition, since the linearly polarized light has a non-axially symmetric intensity distribution at the focal spot, the spot size is smaller when measured in the normal direction of polarization compared with that along the polarization direction of the incident light, which results in non-rotationally symmetric focal spot when the incident polarization is linearly polarized. The deviation of the focus spot sizes from that predicted with Rayleigh theory (i.e. ~ 0.61λ/NA) arises due to the consideration of the polarization in the computation of the spot size with Debye integral. Figure 5 shows line and contour plot of

the electric field intensity distribution obtained from the Debye integral under linear and radially polarized light illumination when NA = 1.0. A further reduction in the spot size can be achieved if an annular aperture is placed before the lens thereby allowing only higher spatial frequencies to be focused by the lens [37]. However, the side lobes of the intensity distribution in the focus plane become more pronounced with the additional annular aperture, which might not be desirable in some applications.

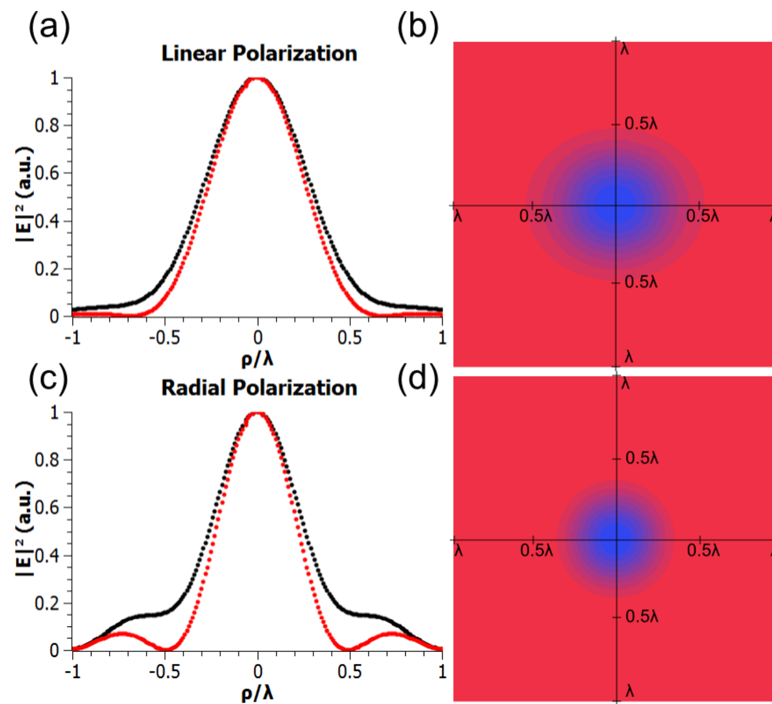

Figure 5: Electric field intensity distribution at the focus spot obtained by solving the Debye integral. (a),(b) show the line plots and intensity profiles for radial polarization and (c),(d) show the line plots and intensity profiles for linear polarization. The dotted red line indicates the profile for the longitudinal field in each case.

In dielectric scanning optical probes (both solid immersion probe and scattering probe) to be described in chapter 5, radially polarized illumination is applied due to its symmetric and sharp focus resulting from the stronger longitudinal fields. In addition, as will be

shown in chapter 5, radial polarized illumination is a requirement to achieve near-field intensity enhancement in the forward direction due by scattering with a nanostructure. The near-field intensity enhancement due to scattering by a nanostructure can further confine the light to tens of nm spot sizes due to the utilization of evanescent waves. A brief explanation of how evanescent waves can achieve nanoscale confinement of light in near field with nano-optic devices is in the next section.

2.3 Near-field light focusing with evanescent waves

The time harmonic format of Maxwell's equation in Helmholtz equation format governs the propagation of light and can be expressed as

$$\nabla^2\vec{E}+k_0^2\vec{E}=0 \ , \tag{10}$$

with k_0 the wave number (ω/c), and $\vec{E}$ is the electric field vector. For a plane wave propagating in free space, the solution of the Helmholtz equation can be expressed as

$$\vec{E}(\vec{r})=\vec{E}_0(r)e^{i(k_x x+k_y y+k_z z-\omega t)} \ , \tag{11}$$

with k_i is the wavenumber in i^th direction and is related to k_0 as $k_0=\sqrt{k_x^2+k_y^2+k_z^2}$. For propagating light that travels in the far-field, the three spatial frequency components k_x, k_y and k_z are real. Note that the spatial resolution of a far-field optical imaging system depends on the in-plane wave number of the propagating light i.e k_x and k_y . In the limiting case of high spatial resolution, k_x or $k_y \approx k_0$, which determines the best possible spatial resolution that can be obtained with a far-field optical imaging system. If however, $k_x, k_y > k_0$, the spatial resolution of the system can be further increased. But under this condition, the out-of-plane wave number component k_z becomes imaginary and the wave solution to Helmholtz equation can be expressed as

$$\vec{E}(\vec{r})=\vec{E}_0(r)e^{-k_z z}e^{i(k_x x+k_y y-\omega t)} \ , \tag{12}$$

which indicates an exponentially decays wave in the z direction, which is known as a vanishing or evanescent wave. Evanescent waves do not participate in energy transport

and have a very short range ($<<\lambda$) in the decaying direction (i.e., z direction in equation 11). Theoretically, evanescent waves can achieve a spatial resolution $>>\lambda$; however, their inherent short range properties are a major challenge in their application in traditional far field optics. There are many different methods to generate evanescent waves. A common method is via total internal reflection at the interface of two media of different refractive indices (n1 > n2) as shown in Figure 6. Some other methods include scattering from metallic/dielectric nano-structures and light propagation through nano-apertures.

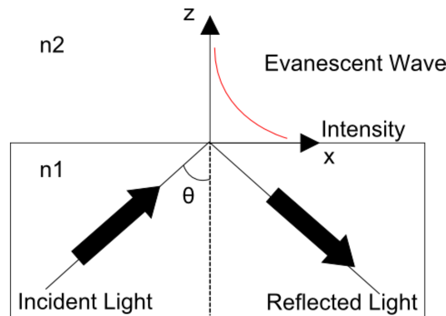

Figure 6: Schematic showing the generation of evanescent waves by total internal reflection.

With the discussed physical background in this chapter, evanescent wave is required to achieve deep sub-micron scale light focusing in near field range. A corresponding solid immersion probe and scattering dielectric probes are then proposed and developed in this graduate study as in chapter 5. Also, with the recent new results of deep sub-micron imaging resolution with microlenses, a thorough analysis of the limits of imaging resolution with microlenses (compared with macrolenses) are presented in chapter 6, which is the last part of this graduate study.

3. TRANSIENT TEMPERATURE RESPONSE OF NSOM PROBES

3.1 Introduction

In chapter 1, we discussed some of the limitations of nano-optic devices based on evanescent waves. It was pointed out that joule heating of metallic nanostructures in nano-optic devices was the major limitation that prevented the application of nano-optic devices in high enegy pulsed laser operation. Near field optical microscope (NSOM) probes are one of the few commercially available nano-optic devices nowadays. In apertured NSOM probes, far field light is delivered to a microscale entrance of a tapered metallic waveguide to obtain intense near field evanescent waves from a sub-diffraction limited aperture (~ tens of nm). Apertured NSOM probes have been successfully adopted in nanoscale detection (such as nano fluorescence microscopy) and nanoscale fabrication (such as nano-lithography and ablation) in the past decade [5, 28, 41-46]. NSOM probes also suffer strong joule heating of the metallic thin film coating utilized for far-to-near field conversion, which can induce and result in thermal damage of the NSOM probes under high power operation [26, 47-49]. In this chapter we study the temperature response of NSOM probes under pulsed laser operation to reveal the possible mechanisms that cause the damage as a result of joule heating such as thermal expansion, induced themal stresses and melting. The results of this analysis are expected to provide useful information for the future design of nano-optic devices that have better resistance to thermal damage for pulsed laser operation.

The heating of apertured NSOM probes has been studied by many groups both theoretically and experimentally. For theoretical study, the light transport and the associated joule heating and thermal energy transport in the NSOM probes are simulated

---

Reproduced with permission from "*Transient temperature response of near field scanning optical microscope probes under pulsed illumination",* Sundaram, V.M., A. Soni, and S.B. Wen, Journal of Applied Physics, 2014. **115**(23), Copyright 2014, AIP Publishing LLC

with finite difference or finite element methods [4, 26, 47]. Due to the limitation of computational resources, the simulation domain is limited to a few μm around the tip of the NSOM probe with a great simplification of boundary conditions [26]. For experimental study, non-intrusive thermoreflectance (TR) imaging, with micron level (or even sub-micron) spatial resolution and up to ~ 1 K level temperature resolution has been adopted to determine the thermal response of NSOM probes [50]. Detailed discussion of TR in temperature measurement can be found in ref 26 [51]. TR imaging with continuous laser was demonstrated by our group in studying thermal response of NSOM probes under different configurations and continuous laser illumination [48].

When the NSOM probes are operating with pulsed light, the traditional TR with continuous laser cannot provide enough temporal resolution to determine the transient thermal response of the NSOM probe. Compared with NSOM probes driven by continuous light, NSOM probes driven by pulsed light can provide orders higher energy intensity to the target and have drawn significant attention in nanoscale fabrication requiring high energy intensity [3, 28, 52-54]. To measure the transient thermal response of NSOM probes driven by pulsed laser, we adopt time resolved TR imaging driven by ns pulse laser, which was demonstrated in our group in 2013 [55]. The time resolved TR is used to determine the transient thermal response, peak temperature and cooling process of the NSOM probe as functions of laser energy, wavelength, pulse duration, and probe configuration. The dominant heat transfer mechanism in NSOM probes under different laser conditions are then inferred from the measured transient temperature profiles. Description of the experimental setup, the measured transient temperature profiles of NSOM probes under different conditions, and the main mechanisms dominating energy storage and heat transfer in NSOM probes are described in the following sections.

3.2 Experimental set-up

Figure 7 shows the experimental setup of the time resolved TR (TRTR) imaging with ns pulsed laser for transient temperature measurement of NSOM probes. A high energy

Nd:YAG laser (Powerlite 8010 Continuum Inc.) operating at second harmonic wavelength (i.e., λ = 532 nm) is selected as a light source (i.e., probe beam). To prevent speckles and large interference patterns in the TRTR optical images, the probe beam is first delivered through a CS_2 liquid cell (to reduce the temporal coherence via spectral broadening) and then an optical fiber bundle (to reduce the spatial coherence) [55]. The resulting probe beam with low temporal and spatial coherences is directed to illuminate the NSOM probe through a beam splitter and an objective lens. Commercial NSOM probes (Nanonics Imaging Ltd.) with thin metal coating to provide strong specular reflection are applied in this study. The NSOM probe, which is the imaging target, is mounted on a 4-axis translation/tilt stage to precisely control the incident angle and location of the probe beam during the measurement. In this study, the center axis of the NSOM probe is maintained in the normal direction of the optical axis of the TR imaging system with the tilt stage. The TRTR images of the NSOM probe are captured with a 16-bit depth B/W CCD camera (Opteon 1000 base T camera 120 frame/s, Opteon Corporation). The NSOM probe is pumped by either μs or ns pulsed light (i.e., pump beam). The μs pulsed light is provided by laser diodes (λ = 650 nm and 450 nm) operating with pulsed current sources (~ 4μs pulse duration). The ns pulsed light is provided by an optical parameter oscillator (λ = 450 nm, pulse width ~ 5 ns). The triggering of the pumping beam, probe beam and the CCD cameras is synchronized with a delay circuit composed with a picosecond precision delay/pulse generator (Model 575 pulse/delay generator, Berkeley Nucleonics Corporation). The imaging lens of the TRTR system (25X magnification and NA ~ 0.25), provides an optical resolution ~ 1 μm. The digital resolution is ~ 0.4 μm/pixel with the lens and CCD camera selected. The temperature resolution of the TR system (with the 16 bit depth CCD camera), from an averaging of 5000 measurements, is ~ 1 K [56].

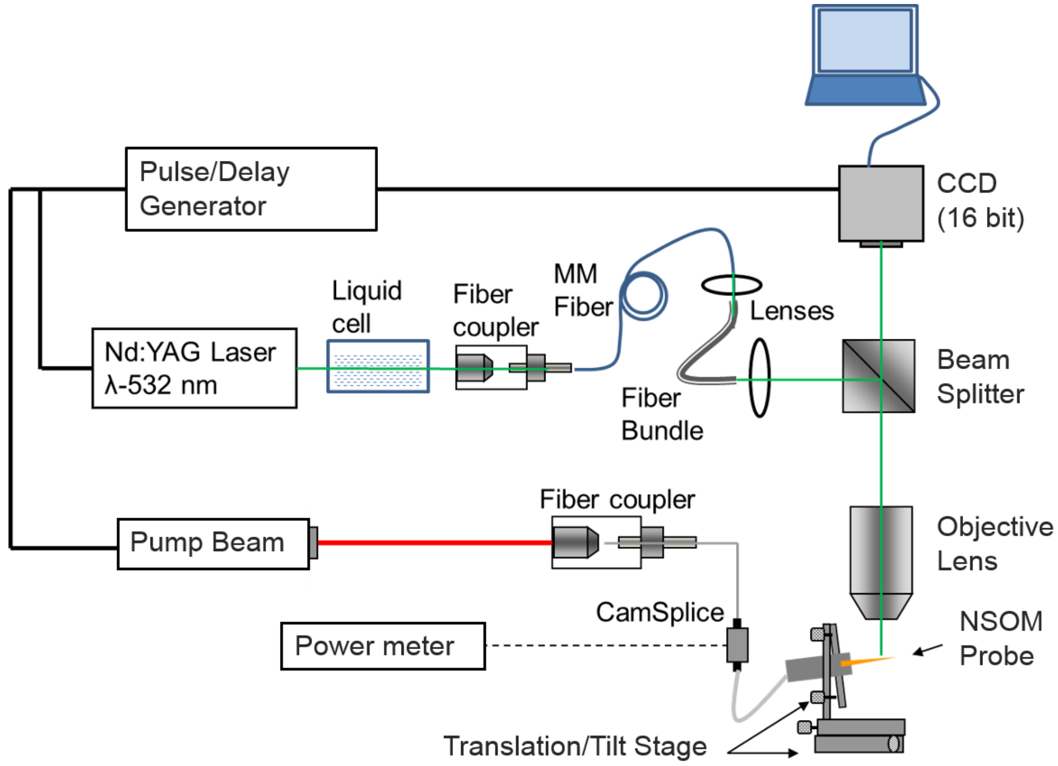

Figure 7: Schematic of the experimental setup of nanosecond TRTR for transient temperature measurement of NSOM probes.

The NSOM probes in this study are supplied by Nanonics Ltd. Two NSOM aperture diameters, 100 nm and 150 nm are selected.

The conversion between the reflection intensity recorded in the TR images and the 2D temperature maps of the NSOM probes follows the TR equation as,

$$\Delta T = \left(\frac{1}{R}\frac{\partial R}{\partial T}\right)^{-1}\frac{\Delta R}{R} = (\kappa)^{-1}\frac{\Delta R}{R} \quad (13)$$

where, ΔR is the change in reflectance, ΔT is the change in temperature and κ is the thermoreflectance coefficient equal to -2.4x10^{-4} /K [48, 57].

3.3 Results and discussion

Since high magnification ratio (25x) is adopted for TR imaging in this study to reveal the temperature profile of the NSOM probe with deep micron scale resolution, the minor defects of the metallic coating of the NSOM probes and the resulting fluctuation of the TR signal is no longer negligible as in the traditional low magnification TR measurement [48]. The non-perfectly smooth surface of the NSOM probe causes non-thermally induced variations of the reflectance signal and the associated fluctuation of the obtained temperature profile especially around the NSOM tip (Figure 8). As a result, higher uncertainty in the temperature measurement with large noise signal is expected in this study. To diminish the noise in the obtained temperature profiles due to the surface roughness, a least squares filtering method (Savitszky-Golay with 3rd order polynomial) is adopted in constructing trend lines of each temperature profile to better illustrate the dynamics of heating/cooling of NSOM probes during the pulsed light illumination.

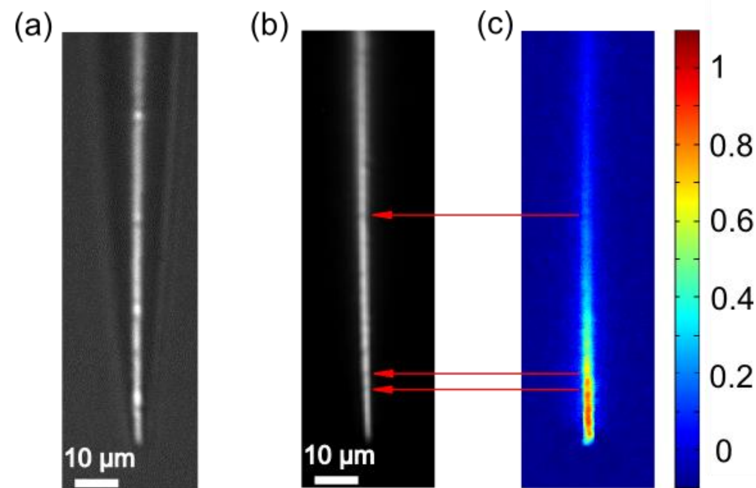

Figure 8: (a) Optical image of NSOM probe with reflective background, (b) optical image of the NSOM probe without reflective background (used in TR), and (c) thermoreflectance image of 150 nm apertured NSOM probe driven by 4 µs laser pulse with λ ~ 450 nm and E ~ 200 nJ. Arrows in the figure indicate some of the non-thermal fluctuations in recorded temperature due to non-smooth coating shown in the optical image.

Figure 9a shows the obtained transient temperature profiles of a ~ 150 nm apertured NSOM probe driven by a 4 μs laser pulse with λ ~ 450 nm and E ~ 200 nJ. Note that we only analyze the surface temperature along the centerline of the NSOM probe (i.e., polar angle of the NSOM coordinates equal to zero). Under such a condition, the recorded TR signal is mainly from specular reflection in the normal direction[58]. Since the NSOM probe is cylindrically symmetric and so is the surface temperature distribution, the recorded centerline surface temperature of the NSOM is representative of surface temperature distribution at different polar angles of the NSOM probe. From the Figure 9a, the temperature of the NSOM probes increases monotonically with respect to time during the laser pulse. The maximum temperature of the probe occurs at the end of the laser pulse (i.e., 4 μs) and then decreases monotonically when the time is increased. The location of the peak temperature of the NSOM probe is fixed during the laser pulse and gradually shifts away from the tip after the laser pulse. Also, the heat affected zone (HAZ, defined as the length of the NSOM probe within 1/e of the peak temperature) becomes broader and shifts away from the tip after the laser pulse. Figure 9b shows the evolution of temperature at a fixed ~ 10 μm location away from the NSOM tip. The local temperature increases almost linearly with respect to time during the laser pulse (c.f., Figure 9b). The cooling history of the specific location, though showing an exponential decay, cannot be well-fitted with a simple exponential function (i.e., Ae^{-at}, where A and a are constants; the simple exponential curve, fitted with a least squares method is represented by the blue dashed line in Figure 9b).

The energy storage and transfer mechanisms in a NSOM probe can be applied to explain the heating and cooling behavior of the NSOM probe driven by a μs laser pulse. The energy from the pumping μs laser pulse, except the portion that is reflected, will be stored in the NSOM probe as thermal energy causing temperature increment and mechanical energy in the form of thermal stress mainly at the metal/dielectric interface of the NSOM probe. The energy transfer in the NSOM probe can be due to (a) lateral conduction along the thin metal film, (b) normal conduction from the thin metal film to the silica substrate,

(c) conduction from the NSOM probe to the surrounding gas, (d) radiation from the surface of the NSOM probe to the surrounding, and (e) thermoelastic (TE) waves along the NSOM probe [59, 60]. Out of the above five mechanisms of energy transfer, radiation and conductive heat transfer from the NSOM probe to the surrounding gas is commonly small compared with conduction within the NSOM probe [4]. TE waves cause the transport of the mechanical energy stored in thermal stresses and do not affect the heat transfer. Between the two types of conduction along and normal to the surface of NSOM probe (i.e., mechanisms a and b), normal conduction from the gold thin film to the silica substrate is much slower than the lateral conduction along the gold thin film due to the smaller diffusion coefficient of silica compared to the gold metal thin film as well as the additional contact resistance at the gold/silica interface. As a result, 1D conduction along the gold film dominates the heat dissipation in an NSOM probe.

Based on the above picture for energy storage/transport in NSOM probes, the small deviation from linear temperature increment of the NSOM probe with respect to time during the μs laser pulse can be attributed to the lateral heat diffusion as well as a portion of laser energy stored in thermal stress when the temperature becomes higher. The cooling history of the NSOM process, which is dominated by 1D lateral heat diffusion along the metal coating, can be well-fitted with a $A\frac{\exp(-a/t)}{\sqrt{t}}$ function (green line in Figure 9b). The $A\frac{\exp(-a/t)}{\sqrt{t}}$ function describes 1D transient conduction along a thin metal film under pulsed heating, where '*a*' is a constant at a fixed location in the gold film and 'A' is a constant that depends on the material properties of the film [61]. The lateral conduction also explains the broadening of the HAZ after the laser pulse as observed in Figure 9a. The shift of the high temperature region away from the tip can be attributed to the small heat conduction from the tip to the surrounding gas as observed in the previous numerical simulation [26].

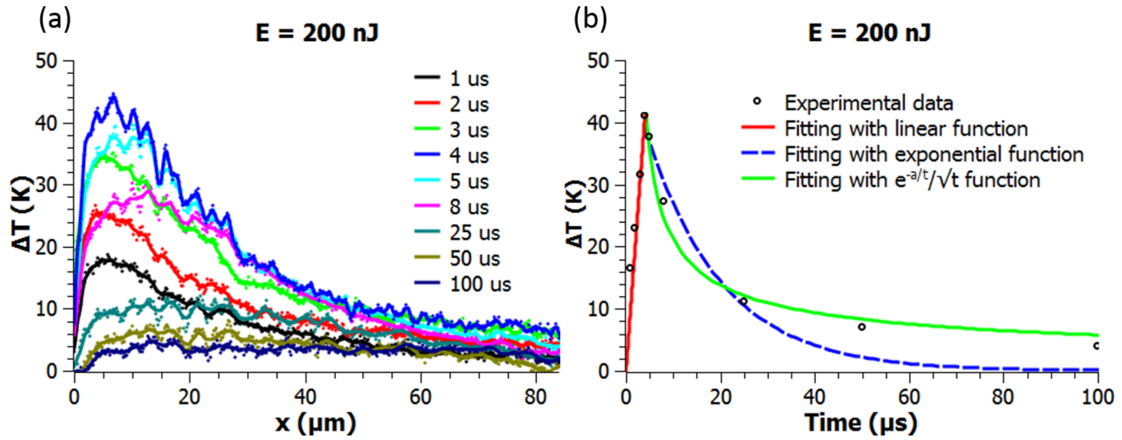

Figure 9: (a) Transient temperature profile of 150 nm aperture NSOM probe driven by 4 μs laser pulse with λ ~ 450 nm and E ~ 200 nJ. (b) Temperature history at a fixed ~ 10 μm away from the tip under the same conditions indicating the different curve fits.

To better understand the contributions of probe geometry and laser conditions on the transient heating of NSOM probes [28], variations of the transient temperature profiles as functions of laser energy, laser wavelength, laser pulse width, and aperture diameter are measured with the ns time resolved TR and are discussed in the following sections.

3.3.1 Case 1: Contributions of laser energy (100 nJ, 200 nJ, 300 nJ)

The transient temperature profiles of the same NSOM probe (i.e., with ~ 150 nm aperture) under two additional different energies (i.e., E=100 nJ and 300 nJ) are measured in this section. The heating/cooling processes of both energies show the same general trend as that with E=200 nJ (Figure 10a and Figure 10b). The temperature of the NSOM probe increases almost linearly with respect to time during the laser pulse for both pumping laser energies (solid red lines in Figure 10c and Figure 10d). The cooling history of both laser energies can be well fitted with $\frac{\exp(-a/t)}{\sqrt{t}}$ function (green line in Figure 10c and Figure 10d) indicating that lateral thermal diffusion along the gold metal coating is still the dominant heat transfer mechanism for both laser energies.

In addition to showing the same general trend, the temperature of the NSOM probe at each location and time increases almost linearly with respect to the input laser energy. The small deviation from a linear E vs. T correlation during the laser pulse can be attributed to the lateral heat diffusion during the laser pulse as well as a portion of laser energy stored in thermal stress especially when the laser energy is increased and the associated NSOM probe temperatures are higher.

In addition to increasing the laser energy, the heating can also be increased by improving the laser-thermal energy conversion efficiency in the NSOM probes. Two parameters reported to have significantly affected the laser-thermal energy conversion efficiency in the NSOM probes are the laser wavelength and the aperture size of the NSOM probe [4, 48]. Contributions of these two factors are studied in cases 2 and 3.

3.3.2 Case 2: Contributions of laser wavelength (450 nm vs. 650 nm)

Transient temperature profiles of the same NSOM probe (i.e., a ~ 150 nm aperture) operating at $\lambda = 650$ nm, E ~ 300 nJ and pulse duration ~ 4μs are presented in Figure 11a. Compared with the thermal response of the same NSOM probe at $\lambda = 450$ nm, E ~ 300 nJ, and pulse duration ~ 4μs, the transient temperature profiles under the longer laser wavelength show the same trend of heating/cooling (i.e., an almost adiabatic heating during the laser pulse and a $A\frac{\exp(-a/\mathrm{t})}{\sqrt{t}}$ temperature decay trend after the laser pulse) as that with shorter laser wavelength at $\lambda = 450$ nm. However, the temperature of the NSOM probe at each time and location becomes lower when the laser wavelength is increased.

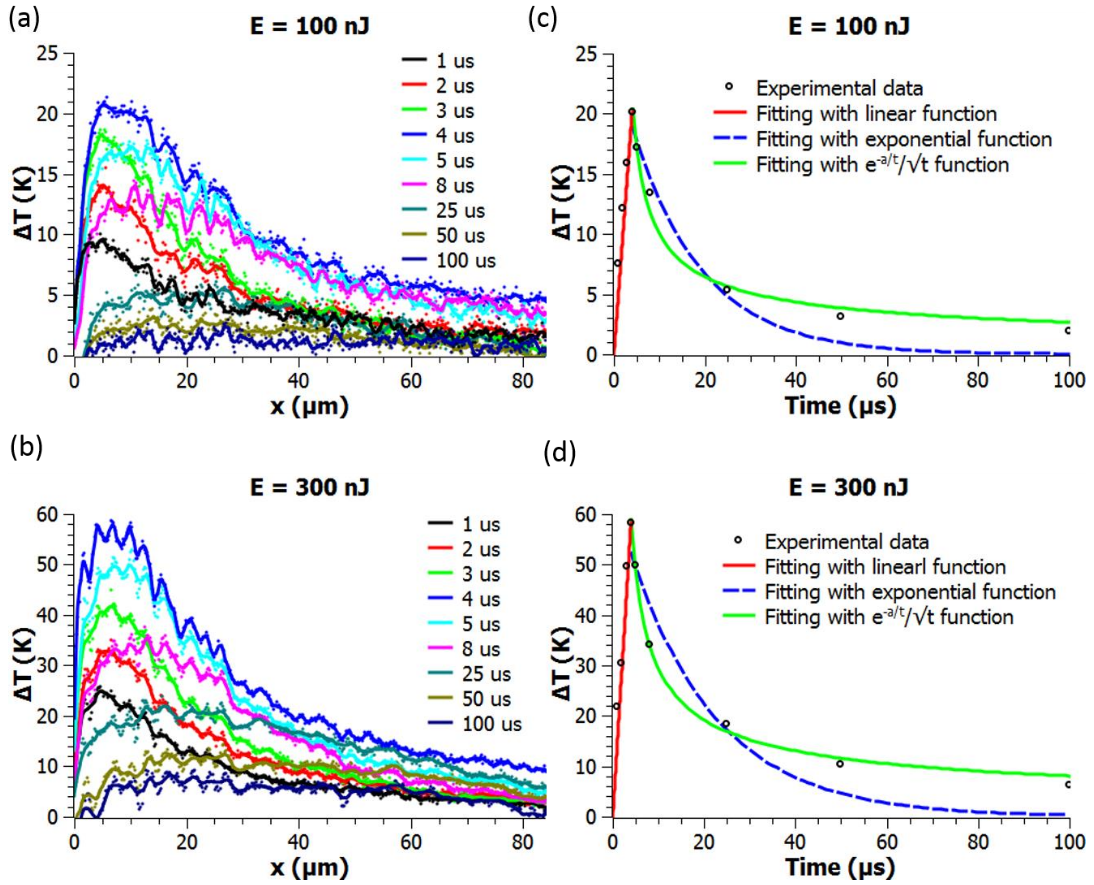

Figure 10: Transient temperature profiles of a 150 nm apertured NSOM probe driven by 4 μs laser pulse with λ ~ 450 nm, and (a) E = 100 nJ or (b) E = 300 nJ. The corresponding temperature histories at a fixed ~ 10 μm away from the tip are presented in (c) and (d) respectively.

For example, the peak temperature of λ = 650 nm at the end of the laser pulse is ~ 3 times lower than that with λ = 450 nm (Figure 10d and Figure 11b). The significant decrease in the temperature of the NSOM probe with the longer laser wavelength can be attributed to the sharp decrease of the reflectivity of the gold thin film at the perimeter of the NSOM probe when the wavelength is less than 480 nm [62]. As a result, the laser-thermal energy conversion in the NSOM probe is less efficient when the laser wavelength is increased from 450 nm to 650 nm, which leads to lower joule heating and the resulting temperature in the NSOM probe during and after the laser pulse.

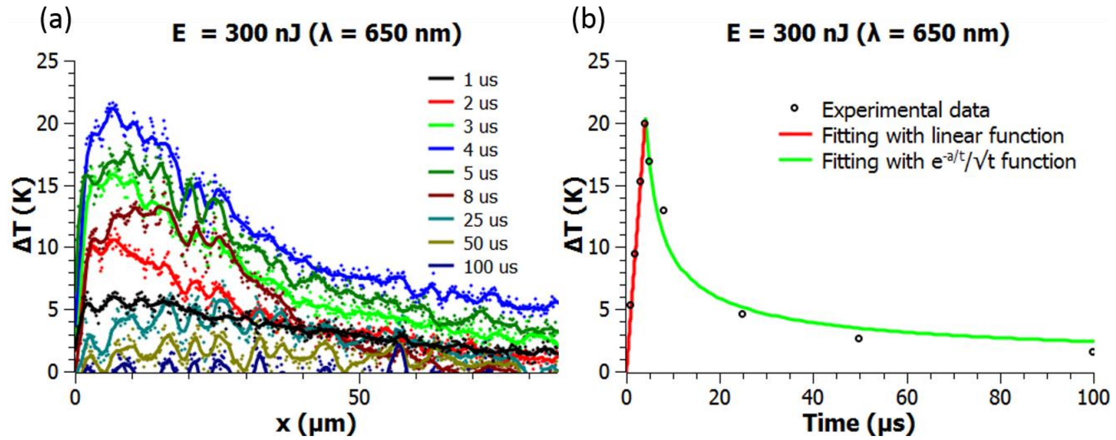

Figure 11: (a) Transient temperature profiles of 150 nm aperture NSOM probe driven by 4 μs laser pulse with λ ~ 650 nm and E ~ 300 nJ. The corresponding temperature history at a fixed ~ 10 μm away from the tip is presented in (b).

The aperture size of the NSOM probe, which is another parameter that can affect the laser–thermal energy conversion efficiency in the NSOM probe is studied in the next section.

3.3.3 Case 3: Effect of aperture size of NSOM probe (100 nm and 150 nm)

Transient temperature profiles of an NSOM probes with smaller aperture size (~ 100 nm) driven by blue laser (λ = 450 nm) with a pulse duration ~ 4μs and E ~ 300 nJ are measured in this section. Figure 12a shows the resulting temperature profile of the NSOM probes (experimental data in black dots and Savitszky-Golay fitting in a black curve) at the end of the laser pulse (i.e. 4 μs). For comparison purpose, the transient temperature profile of a larger apertured NSOM probe (~ 150 nm) under the same laser condition (presented in Figure 10b) is reproduced in the same Figure 12 (experimental data in red dots and Savitszky-Golay fitting in a red curve). The peak temperature occurs at ~ 3- 4 μm rather than ~ 6-7 μm away from the tip when the NSOM aperture is reduced from ~ 150 nm to ~ 100 nm. In addition, the peak temperature of the ~100 nm apertured NSOM probe at the end of the laser pulse is ~ 70 K, which is ~ 1.2 times higher than the peak temperature of the ~ 150 nm apertured NSOM probe at the end of the laser pulse. The change in the location of the peak temperature can be attributed to the increase in the tapering angle of

the NSOM probe with smaller aperture when the NSOM probes are prepared with fiber pulling method [1, 26]. The larger tapering angle causes the sub-diffraction limited cross-sectional area of the NSOM probe, and the hotspot of the probe during laser operation, to occur closer to the tip. The higher peak temperature for the 100 nm probe can be attributed to the higher laser-thermal energy conversion efficiency for smaller apertured NSOM probes when the aperture size is less than the diffraction limit [4, 48]. The cooling process of the smaller apertured NSOM probe, on the other hand, shows the same trend with the larger apertured NSOM probes in Case 1. The green line in Figure 12b shows the fitting curve of the temperature history at ~ 10 μm from the tip of the ~ 100 nm apertured NSOM probe. The good fitting with $A\frac{\exp(-a/\mathrm{t})}{\sqrt{t}}$ function in Figure 12b indicates that the cooling of the smaller apertured NSOM probe is also dominated by lateral thermal diffusion along the metal coating similar to the ~ 150 nm apertured NSOM probe.

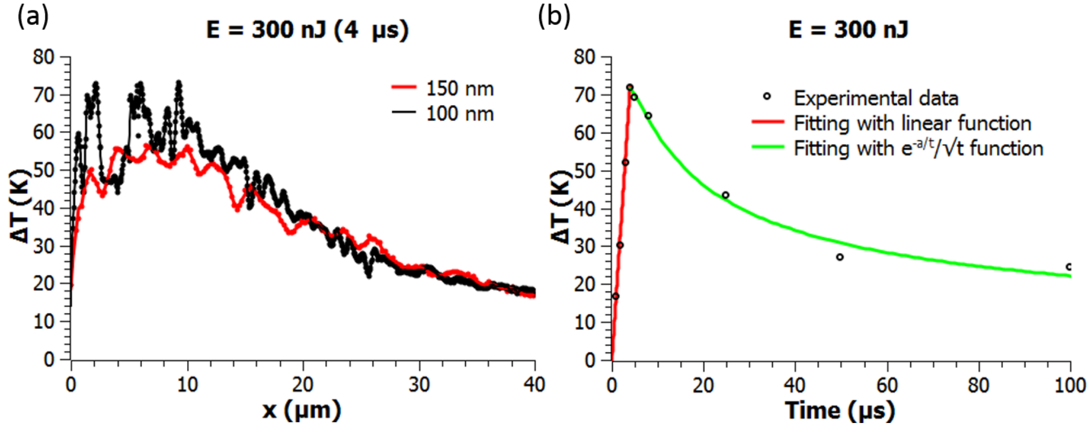

Figure 12: (a) Transient temperature profile of a 100 nm and a 150 nm apertured NSOM at the end of a 4 μs laser pulse with λ ~ 450 nm and E ~ 300 nJ. Temperature history of a 100 nm aperture NSOM probe at a fixed ~ 10 μm location away from the tip under the same laser conditions as part (a).

3.3.4 Case 4: Effect of pulse duration (5 ns vs. 4 μs)

Though it was not mentioned in many publications, we expect that the pulse duration of the driving laser can also affect the transient thermal response of the NSOM probe. From the thermal diffusivity of a ~ 200 nm gold film (6.023 x 10^{-5} m^2/s [63]), the thermal diffusion length is ~ 15 μm during a 4 μs laser pulse. By reducing the pulse width, we expect a decrease in thermal diffusion length, a more adiabatic heating and consequently a higher peak temperature of the NSOM probe during the laser pulse. With the developed ns time resolved TR, we are able to compare the thermal response of NSOM probes under both ns and μs laser pulses.

Figure 13a shows the obtained transient temperature profiles of a ~ 150 nm apertured NSOM probe driven by a ~ 5 ns laser pulse with λ ~ 450 nm and E ~ 100 nJ. Note that since the ns pulse width of the pump laser (i.e. 5 ns) is comparable with the 4 ns pulse width of the probe laser for TDTR, only two temperature profiles, namely, at 0 ns and 5 ns are measured during the laser pulse. The peak temperature increment ~ 25 K at the end of the 5 ns laser pulse is higher than the peak temperature increment ~ 20 K at the end of the 4μs laser pulse. The higher peak temperature can be attributed to a more adiabatic heating during the ns laser pulse as discussed in the last paragraph. Also, due to the more adiabatic heating and less heat dissipation from the NSOM tip to the surrounding gas, the location of the peak temperature for the 5 ns laser pulse is much closer to the tip of the NSOM probe (< 2 μm) compared with that of the 4 μs laser pulse (~ 6 - 8 μm). However, if we consider both the decrease in the size of the heated region (more than 3 times) and the slight increase in the peak temperature (about 1.2 times) when the ns laser pulse is applied, the amount of thermal energy delivered to the NSOM probe with the 4 ns laser pulse is more than 2 times less than that with the 4 μs laser pulse. The decrease in the amount of thermal energy in the NSOM probe during the ns laser pulse can be attributed to a large percentage of the input laser energy being stored in the form of thermal stress, owing to a more localized heating and the resulting steeper temperature gradient in the NSOM probe during a ns laser pulse. The stronger thermal stress and the associated

stronger TE waves with ns laser pulse can also cause damage to the NSOM probe. Figure 14 shows small exfoliation of the metal coating of the NSOM probe around the aperture after ~ 200,000 times of operation, which increases the aperture size of the NSOM probe from 150 nm to ~ 250 nm. Also, black spots appears in the SEM image of the metal coating of the NSOM probe after ~ 200,000 times of operation (Figure 14). The degrading of the NSOM probe under ns laser pulse could also be one of the reasons for the lower laser-thermal energy conversion observed in this case 4 (compared with case 1 with μs laser pulse).

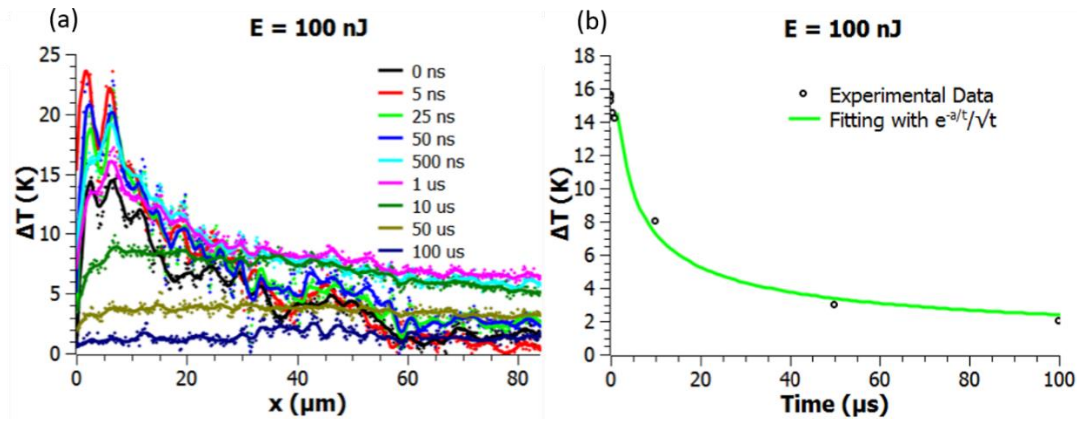

Figure 13: (a) Transient temperature profiles of 150 nm aperture NSOM probe driven by 5 ns laser pulse with λ ~ 450 nm and E ~ 100 nJ. The corresponding temperature history at a fixed ~ 10 μm away from the tip is presented in (b).

Figure 13b shows the cooling history of the NSOM probe at a fixed ~ 10 μm location from the tip after a 5 ns laser pulse. The cooling temperature profile can also be well fitted with the $A\frac{\exp(-a/t)}{\sqrt{t}}$ function indicating that the lateral thermal conduction is still the dominant mechanism of cooling of the NSOM probe, and is not affected by the pulse duration of the pumping laser.

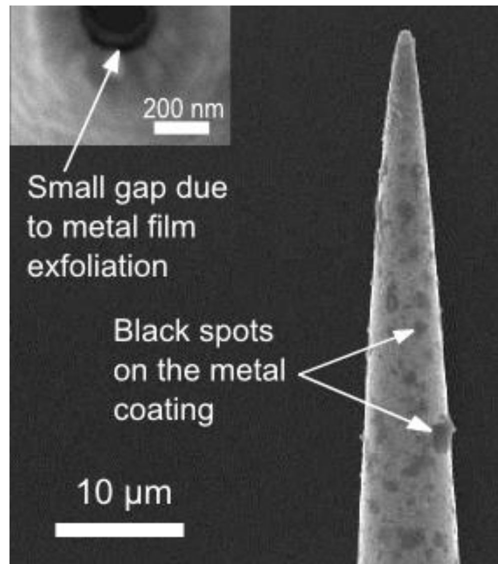

Figure 14: SEM images of the thermally damaged NSOM black spots on the gold thin film coating and small exfoliation of metal film around the aperture of the NSOM probe after ns laser experiments (Inset).

3.4 Summary

Nanosecond time resolved thermoreflectance imaging is applied to study the transient thermal response of NSOM probes. It is observed that the temperature of the NSOM probe can be increased through increasing the input laser energy or increasing the laser-thermal conversion efficiency via reducing the input laser wavelength or decreasing the aperture size of the NSOM probe. The small deviation from linear heating of the NSOM probe with respect to time under a μs laser pulse can be attributed to heat dissipation during the laser pulse as well as the storage of energy in the form of thermal stresses especially at the interfaces of the metal thin film coating on the NSOM probe. During the cooling after the laser pulse, the heat dissipation in the NSOM probe is dominated by the lateral conduction along the metal thin film coating of the NSOM probes. Therefore, the cooling curve of the NSOM probes can be well fitted with $A\frac{\exp(-a/t)}{\sqrt{t}}$ function which represents 1D thermal diffusion in a metal thin film after pulsed heating.

When the NSOM probe is pumped with ns laser pulses, much lower laser-thermal energy conversion efficiency is observed compared with that under μs laser pulse. The lower laser-thermal energy conversion efficiency with ns laser pulse can be due to the larger thermal stresses and the associated mechanical energy storage under the more adiabatic heating of the NSOM probe when ns laser is applied. The degrading of the metal coating and the enlargement of the aperture size of the NSOM probes under long term operation with ns laser pulse can also be attributed to the strong thermal stresses in NSOM probes induced by ns laser pulses.

Based on the transient thermal analysis of the NSOM probe, the major limitation of the NSOM probe during high energy operation is attributed to the joule heating of the metal (gold in this study) thin film coating of the probe and the associated thermal/mechanical damage during operation. In addition, the NSOM probes have low optical throughput which limits the application of NSOM in laser based fabrication/lithography. In the following part of this dissertation, we investigate new optical devices with high optical throughput and/or minimum joule heating that have the potential to overcome the limitations of the NSOM probes in direct fabrication and microscopy applications. In chapter 4, the MZP is first studied, which has advantages in higher optical throughput and longer working distance compared with NSOM probes.

4. DESIGN AND CHARACTERIZATION OF MICRO-ZONE PLATE OPTICAL PROBES

4.1 Introduction

In the previous chapter we studied the heating of NSOM probes under pulsed laser operation. It was observed that under pulsed operation, joule heating of the metal thin film coating of the NSOM probe resulted in large thermal stress which degraded the metal coating and enlarged the aperture due to exfoliation. The low optical throughput of the NSOM probe limits the application of NSOM in laser based machining/fabrication applications. It is therefore desirable to design new micro/nano-optic devices with high optical throughput that are better suited for high energy pulsed operation. In this chapter we investigate a new binary phase plate based optical probe which can achieve high optical throughput and long working distance compared with NSOM probes. Description of the design, fabrication and characterization of the new probe are provided as follows.

In 2010, Huang et al. demonstrated that bright focus spots of sizes ~ 0.4λ which is less than the far field-diffraction limit can be generated at a distance of ~ 10 μm from a nanohole array on a metal screen [64]. The effect was termed as super-oscillations and comes from that fact that superpositions of optical waves of different spatial frequencies and amplitudes can form arbitrarily small spatial localizations that occur far away from the source without the need for evanescent waves [30]. Super-oscillatory localizations however, exhibit a very important characteristic that the super oscillatory features are of very low intensity (~ 10^{-3} to 10^{-5} of the incident light) compared with the surrounding sidebands. To achieve such small localizations a super-oscillatory lens has to be fabricated which consists of a binary phase mask consisting of transparent and opaque rings of

---

Part of this chapter is reproduced with permission from "*Fabrication of micro-optical devices at the end of a multimode optical fiber with negative tone lift-off EBL*", Sundaram, V.M. and S.B. Wen, Journal of Micromechanics and Microengineering, 2012. 22(12).Copyright 2012, IOP Publishing

different widths and diameters (which generate waves of same amplitude but different phase). A binary super-oscillation lens has been demonstrated to achieve ~ 0.3λ spot size with a focal length of 10 μm [65]. The binary super-oscillation lens was fabricated by FIB milling of an aluminum thin film coated on a glass substrate.

Although the binary phase plate super-oscillation lens can generate localized regions with spot size marginally smaller than the far-field diffraction limit, the optical throughput of the lens is very low [66]. As a result, a high input intensity is required for application of the super-oscillation focus in fabrication/detection. Since some of the zones of the binary phase plate have sub-wavelength dimensions significant joule heating puts a limit on the maximum input energy that can be applied.

In this study we design a binary phase plate consisting of transparent and opaque zones named micro-zone plate (MZP). Compared with the traditional super-oscillation lens, the optical throughput of the MZP is very high (due to the diffraction limited focus) with a focus intensity of ~ 100 times that of the incident light. In addition the focus spot does not have significant side lobes resulting in high signal-to-noise ratio when applied in high resolution microscopy. The MZP is fabricated on an optical fiber that can be subsequently mounted in a scanning probe microscopy system to achieve accurate positioning and fast scanning. The design of the MZP is based on the theory of light focusing with traditional Fresnel Zone plates that are commonly used for focusing of x-rays and is described in the next section.

4.2 Design of micro-zone plate (MZP)

Consider a plane monochromatic wave incident on structure consisting of alternating, concentric transparent and opaque slits. The location and width of the zones is designed based on the equal optical length principle. Based on Huygens theory, each point on the transparent slit acts as a point source for secondary wavelets. If the path difference between the light from two adjacent transparent and opaque zones is exactly λ, the light

from the different transparent zones will interfere constructively at the designed focus location. A schematic of an MZP following the above design criteria is shown in Figure 15a. The optical path length from the center of the zone plate is denoted by *f* (i.e. the focal length of the MZP). Since the center zone is blocked the width of second zone must be designed such that the light emitted from the central zone destructively interferes with light from the second zone. In other words, light from the point r_1 in the Figure 15a should have a path length of (f + λ/4) and light from r2 should have a path length of (f + 3λ/4). Hence the width of the first zone is given by

$$\Delta r = r_1 - r_2 = \sqrt{\left(f + 3\lambda/4\right)^2 - f^2} - \sqrt{\left(f + \lambda/4\right)^2 - f^2} \quad (14)$$

The width of the remaining zones can be calculated in a similar manner. Note that the above equation considers only the first order focus of the designed MZP and neglects the higher order foci. This approximation is valid when the numerical aperture NA > 0.5 which is applicable for the MZP designed in this study.

Two MZPs with 50 zones (NA ~ 0.99) and 8 zones (NA ~ 0.9) and a focal length of 3 µm are designed in this study to focus light with incident wavelength of λ = 400 nm. The light propagation and focusing of the designed MZPs is verified with a full wave based electrodynamics simulation based on finite element (FEM) method. The simulation conditions are as follows: An 8 zone copper MZP (thickness = 200 nm) is constructed with the zone dimensions obtained from equation 14. A linearly polarized plane wave of wavelength λ = 400 nm is incident on one side of the MZP. The optical properties of copper at this wavelength are obtained from [62]. Figure 15c shows the simulated field distribution after passing through the MZP.

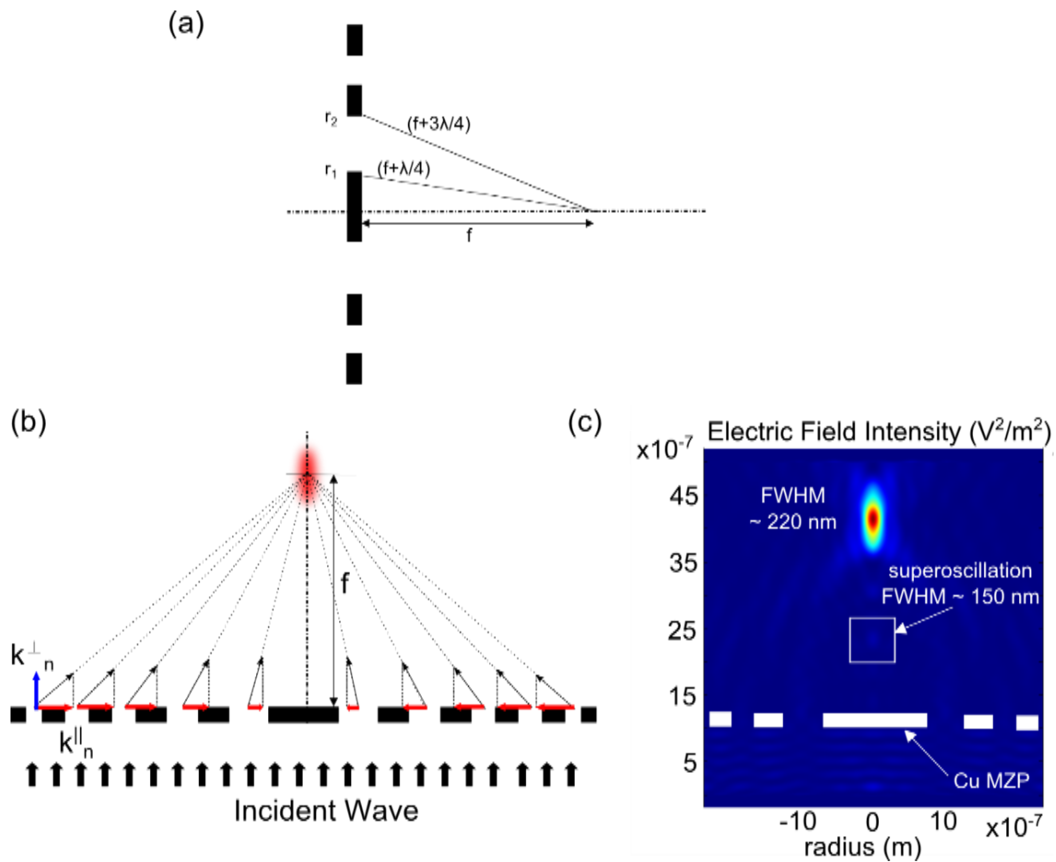

Figure 15: (a) Schematic showing the design of zone widths of MZP. (b) Schematic showing the focusing of light by the MZP. The length of the red arrows indicate the magnitude of the in-plane component of the spatial frequencies from the different zones. (c) Finite element simulation of light focusing with copper MZP consisting of 50 zones with a numerical aperture NA ~ 0.98.

Based on the simulated field distribution, the location of the focus spot (corresponding to the peak intensity of the focused light) occurs at f ~ 3 μm which matches the design focal length of the MZP. The FWHM of the spot is ~ 220 nm, which is smaller than the incident wavelength. Note that light focusing with the designed MZP shows little dependence on the constructing material of the MZP as long as the metal film of the MZP is optically thick. In addition to the designed focus which occurs at ~ 3 μm from the surface of the MZP, an additional super-oscillation focus of lower intensity can be observed at ~ 1.2 μm from the surface. The FWHM of the super-oscillation localization is ~ 150 nm which is

smaller than the far-field diffraction limit. The focusing of light by the MZP can be explained in terms of super-position of plane waves of different spatial frequencies $k_n^{\parallel}$ as shown in Figure 15b. The length of the red arrow in the figure indicates the magnitude of the in-plane component of the spatial frequency $k_n^{\parallel}$ generated at each zone. As shown in the figure, the higher spatial frequencies are generated at the outer zones while the lower spatial frequencies are generated along the axis of the MZP. As the number of zones of the MZP is increased, the contribution of higher spatial frequencies to light focusing increases resulting in smaller focus spot sizes. Compared with the super-oscillation focus that occurs at ~ 1.2 μm, the design focus of ~ 3 μm has a much higher intensity (i.e. ~ 100 times that of the incident light). In addition the focus spot at 3 μm does not have significant side lobes which is important for application of MZP in material processing.

Based on the design dimensions described above, a MZP optical probe (i.e. MZP fabricated at the end face of an optical fiber) is fabricated and focusing characteristics are experimentally characterized. In the next section, we discuss the process that is developed for fabrication of the MZP at the end face of an optical fiber. The MZP fabricated on an optical fiber can then be mounted in a scanning probe microscopy system to achieve accurate positioning and fast scanning for nanoscale microscopy and patterning (Figure 16).

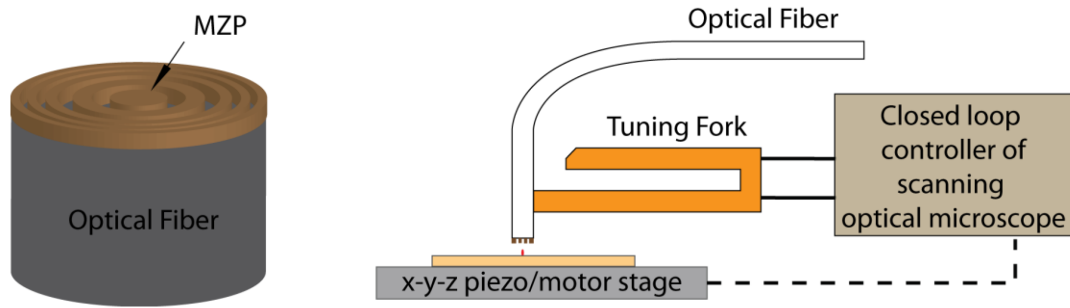

Figure 16: Schematic of MZP fabricated at the end face of an optical fiber which can be mounted on the tuning fork of a scanning probe microscopy system for accurate positioning and scanning.

4.3 Methodology for fabrication of devices at the end faces of optical fibers

4.3.1 Introduction

Optical fiber is a miniature sized refractive optical device which can guide light for a long distance with low losses. Optical fiber based devices can be small, light-weight and portable, which is important in in-situ sensing, imaging and optical trapping applications [67-69]. An important consideration in optical fiber based devices is the transport of the guided light from the end face of the fibers to designated target [70]. Macroscopic optics such as spherical or GRIN (gradient-index) lenses that can be attached to the end of the optical fibers are commercially available and can be applied to properly project the emitted light to the selected target. However, these optical components have sizes much larger than the diameter of the optical fiber, which limits the miniature feature of optical fibers in real applications. There is a great desire to have "microscale lenses" with the same characteristic size as the diameter of optical fiber to fully utilize the size advantages of optical fibers for applications in communication, detection and fabrications [71].

A new methodology to fabricate an MZP [72, 73] at the end of optical fibers is developed. A few existing microfabrication techniques have been demonstrated to construct nano-structures at the end of optical fibers [74, 75]. Focused ion beam (FIB) milling, one of the most common techniques, provides high spatial resolution (~ 10 nm) with minimum

sample preparation. Grating patterning at the end of optical fiber with or without a metal coating has been demonstrated with FIB [76]. However, gallium ions are implanted into the patterned substrate during FIB, which induces undesired change of the refractive index of the substrate and the resulting optical performance of optical fibers [77]. In addition to FIB, pattern transfer methods have been demonstrated to construct nano-patterns at the end of optical fibers. In pattern transfer methods, sacrificial layers are used to transfer metallic nano-patterns from traditional substrates to the facets of optical fibers [78-80]. Other similar methods include nano-imprint lithography with a UV curable resist which has been applied for the fabrication of micro/nano-patterns at the faces of optical fibers [81, 82]. While both transfer and imprint methods are free from ion implantation as in FIB milling, patterns constructed with both methods have lower adhesion with the facet of the optical fiber and may not sustain strong surface stresses (e.g., thermal stresses) under high temperature and high stress operating conditions (e.g., high input laser energy) [79].

It has been demonstrated that e-beam lithography (EBL) can construct robust patterns on dielectric substrates and can be a suitable technique to fabricate nano-structures at the end of optical fibers. To fabricate MZPs, which consist primarily of metal nano-trenches of designed widths on a substrate with a metal thin film coating, two types of EBL methods can be applied, namely, (a) a positive tone process combined with reactive ion etching of the metal thin film or (b) a negative tone process combined with lift-off of the metal thin film. Recently, positive tone e-beam lithography followed with reactive ion etching (RIE) was demonstrated for constructing gold gratings on the end face of optical fibers [83, 84]. Since RIE can damage the facet of the optical fiber during reactive etching, rough pattern edges can result during positive tone processes. To fabricate micro-optical devices on end faces of optical fibers with high precision and little damage to the surface of the optical fiber, negative tone lift-off e-beam lithography at the end of optical fiber is preferred. Note that a positive tone lift-off process (as opposed to positive tone process combined with RIE) in e-beam is also not adequate for patterning nano-cavities or trenches which requires depletion of small regions on a large area metal coating (e.g., the MZP in this study). A

negative tone lift-off process with a negative e-beam resist, on the other hand, is more adequate to fabricate nanoscale depleted regions on the target. In a recent study, we developed a HSQ (hydrogen silsesquioxane) /PMMA (poly methy methacrylate) bi-layer process along with conducting polymer layers (to overcome charging and proximity effects) for high resolution negative tone lift-off fabrication on insulating substrates [85-87]. However, the traditional negative tone e-beam lithography procedure is optimized for nano-structures on large 2D surfaces. It is challenging to extend the negative tone lift-off procedure consisting of multiple resist layers to the fabrication at the end of a dielectric optical fiber with only ~ 100 μm diameter. Challenges to be solved include coating of uniform multiple e-beam resist at the end of the optical fiber with controlled thickness, minimizing of charging and proximity effects on low conducting dielectric optical fibers and the alignment of patterns precisely at the end of optical fibers. The developed approaches in this study that address the above challenges are discussed in the following section.

4.3.2 Fabrication methodology

We first briefly describe the negative tone lift off process based HSQ, PMMA and conducting polymer layers that can be applied for fabrication on insulating structures. The conducting polymer polyaniline (PANI) is introduced as an intermediate conducting layer to minimize that charging and proximity effects associated with e-beam lithography. A schematic of the final process is shown in Figure 17. The substrate to be patterned is spin coated with four polymer layers consisting of HSQ/PMMA/PANI/PMMA. In order to achieve smooth PANI layer with spin coating, the following procedure is applied for the preparation of PANI solutions: Polyaniline emeraldine base (molecular weight=20k, Sigma Aldrich) is ultrasonically dissolved in an 8% weight ratio in N-methyl pyrrolidone (NMP, Sigma Aldrich). The PANI in NMP solution is filtered through a 0.2 μm syringe filter to remove any sediment from the emeraldine base (powder) [88]. The filtered polyaniline solution can be spin coated on to the desired substrate. However the spin coated intrinsic PANI is not conducting and has to be doped by immersing the coated

substrate in protonic acids like HCl or HNO_3 to achieve a conductivity of upto ~ 1S/cm^2 depending on the doping time and the acid pH. After the four layers namely HSQ/PMMA/PANI/PMMA have been coated, e-beam lithography is performed on the HSQ layer. The pattern is then transferred through the remaining polymer layers to the substrate with reactive ion etching in O_2 plasma. The etch time has to be calibrated to provide sufficient undercut for a smooth lift-off process. In our study, high resolution SEM images of undercut profiles at different etch times are used to determine the exact etch time required for enough undercut. The etching is followed by metal deposition and lift-off of the polymer layers with NMP. It is noted that both PMMA and PANI can be etched with the same O_2 RIE process and dissolved with the same resist stripped (i.e. NMP) during lift-off and hence do not complicate the lift off process. In addition, the bottom PMMA layer does not participate significantly in the e-beam writing process and the thickness of the layer can be varied depending on the desired thickness of the metal film required during deposition. Therefore, arbitrary bottom PMMA thickness can be applied in the four layer (HSQ/PMMA/PANI/PMMA) scheme to achieve the required high aspect ratio for the fabrication of desired structures. The next step of fabrication involves extending the negative tone lift off process described above for fabrication on small area surfaces i.e. optical fibers.

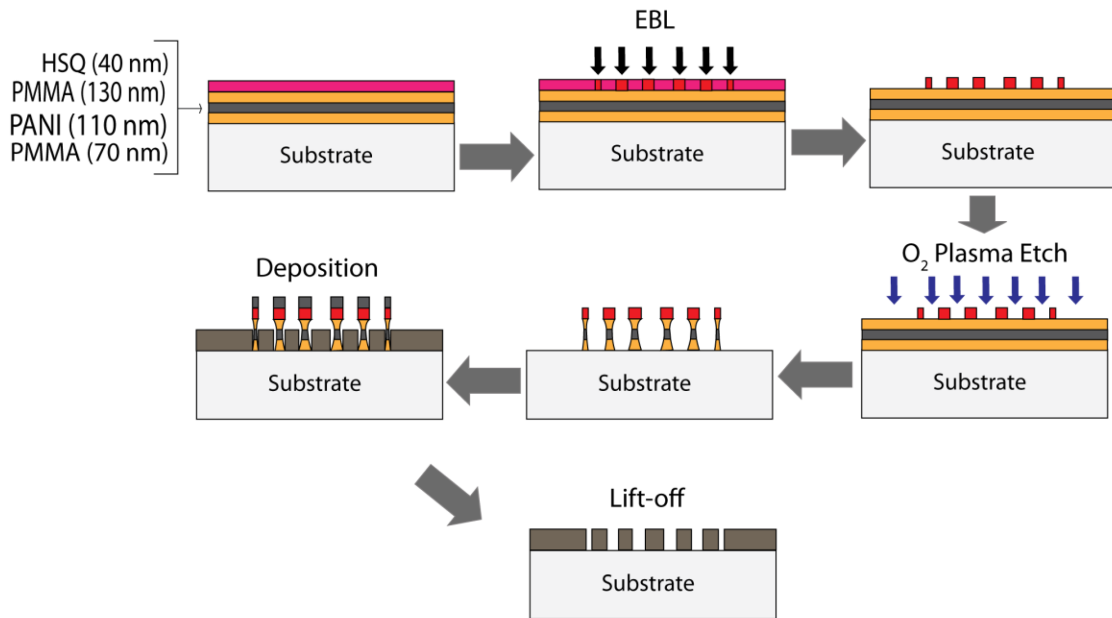

Figure 17: Schematic of fabrication process with PANI as the conducting layer Reprinted with permission .from [89].

Four improvements are established to solve the issues involved in applying negative tone EBL to fabricate nano-patterns at the end faces of the optical fibers. The four improvements are (a) integration of the optical fiber with a fiber optic ferrule to convert a small 3-D structure such as the end of the optical fiber to a larger 2D planar surface required in e-beam patterning; (b) preparation of a conductive multilayer coating on the extended 2D surface of the optical fiber to minimize charging and proximity effects during EBL; (c) alignment of the substrate during e-beam writing of the MZP pattern on the resist; and (d) development of optimized metal coating and lift off conditions for constructing metal nano-patterns at the end of the optical fiber.

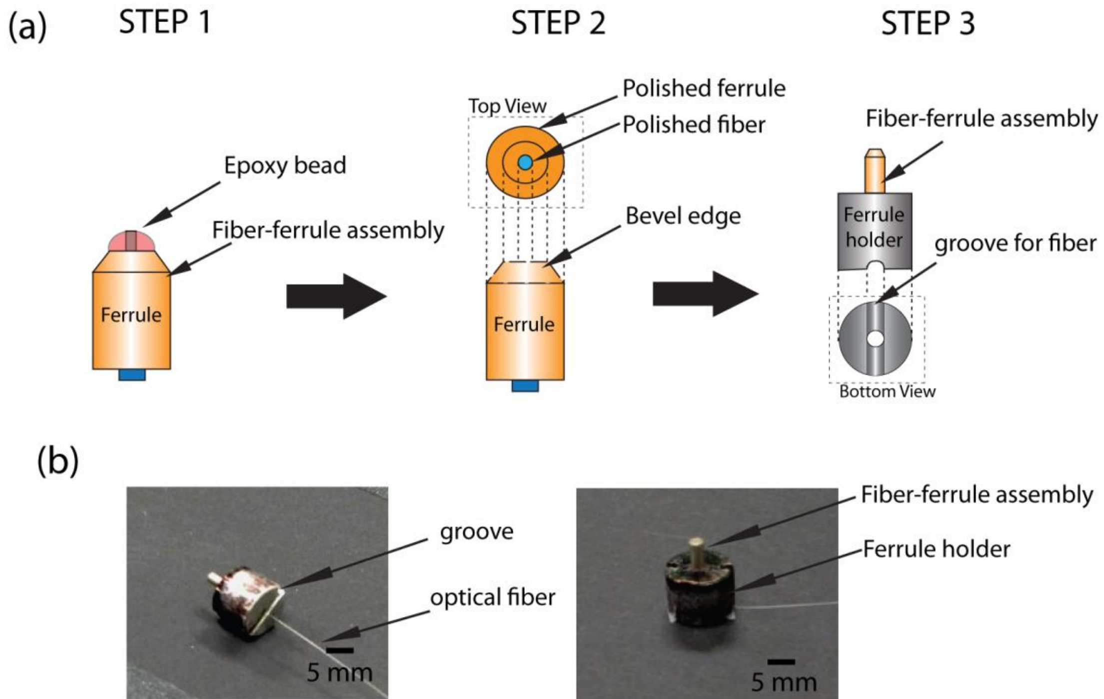

Figure 18: (a) Step 1: insert and fix an optical fiber in a ferrule with epoxy, Step 2: polish the end of the optical fiber with a sequence of 5 µm, 3 µm and 0.3 µm aluminum oxide lapping films and Step 3: mount the fiber-ferrule assembly to a ferrule holder during e-beam lithography. (b) Orthographic projection photos of fiber-ferrule assembly mounted in ferrule holder with extended length of optical fiber bent along the groove.

4.3.2.1 Integration of an optical fiber with a ferrule

A multimode UV-50 fiber (from CeramOptec) with a core diameter of ~50 µm and a cladding diameter of ~ 125 µm is selected in the fabrication. In order to conduct EBL, the diameter of the sample should be large enough to be mounted on a sample holder of an EBL system. To enlarge the effective diameter of the optical fiber during fabrication, the cleaved optical fiber without polymer jacket is inserted into a stainless steel alloy ferrule (FIS Inc.) filled with fiber-optic epoxy (EPOTEK 353ND, Step 1 of Figure 18a). A diamond tipped fiber scribe is applied to score the part of the fiber that extruded out of the epoxy bead. The ferrule is then manually polished with 5 µm, 3 µm and 0.3 µm aluminum oxide lapping films in a sequence until an optically smooth ferrule and fiber surface is obtained (Step 2 of Figure 18a). The quality of the polished surface is traced with a high

numerical aperture microscope (Figure 20). After assembling the optical fiber with the ferrule, the effective diameter is enlarged to ~ 1.5 mm (which is the outer diameter of the assembly) compared to the original 125 μm fiber facet. The entire fiber-ferrule assembly is then large enough to be mounted on an aluminum holder (diameter = 12 mm, height = 10mm) required during EBL. The extended length of optical fiber is bent along a groove machined at the bottom of the aluminum holder (Figure 18b).

4.3.2.2 Preparation of a conductive multilayer coating

Before conducting EBL, smooth layers of e-beam resist of specified thickness should be coated on the surface of the substrate (i.e., the end of the optical fiber). In previous studies, the coating of e-beam resist on a small planar surface such as the end of the optical fiber has been carried out with thermal evaporation [90]. However, such a method is limited to few resists which are compatible with thermal evaporation and most of them suffer from low pattern resolution. Dip and vibration coating is another method that has been applied to coat resist at the end of optical fibers [83]. However, it is difficult to reproduce the same resist thickness with the dip and vibration method.

Spin coating is a traditional method to construct uniform polymer layers of designed thickness on planar surfaces with high reproducibility. The polymer layer thickness from spin coating can be precisely controlled as a function of the spin speed. In this study, the extended surface of the fiber-ferrule assembly prepared in part (a) (~ 1.5 mm in diameter) allowed spin coating to be applied. To diminish the edge bead formed at the periphery of the ferrule during the spin coating which can cause non-uniformity and is an important issue for small surface spin coating, ferrules with beveled edges at the perimeter were used (Figure 18a, Figure 19).

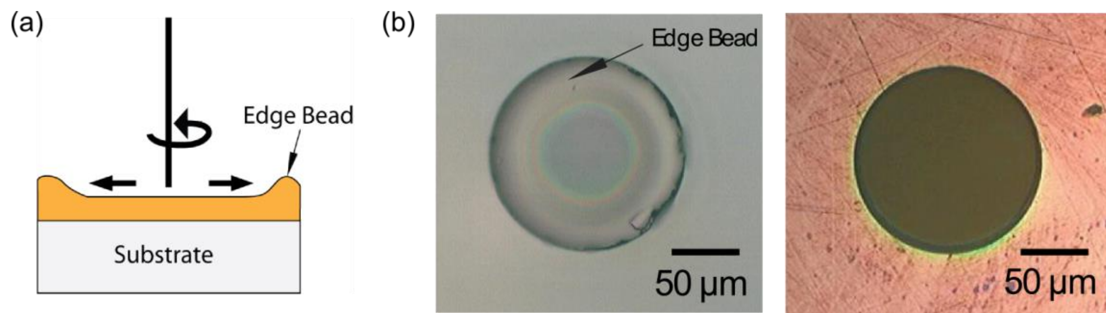

Figure 19: (a) Schematic showing edge bead formation during spin coating process on small area substrates. (b) Optical microscope images of edge bead formed by direct spin coating on optical fiber and removal of edge bead by spin coating on fiber-ferrule assembly with bevel edged ferrule.

The charging and proximity effects during e-beam patterning on poor conducting substrates such as the dielectric optical fiber were overcome with a multilayer resist containing a conductive polymer layer [85, 89]. The multilayer coating starts with a 90 nm thick PMMA layer (3 % PMMA spin speed: 8000 rpm, spin time: 80 s, prebaked at 150 ^{0}C for 5 min). A 100 nm thick layer of 8 % PANI in N-methyl pyrrolidone (NMP) is coated on top of the PMMA layer (spin speed: 10000 rpm, spin time: 90 s, prebaked at 150 ^{0}C for 5 min). The PANI layer is then doped by immersing the coated fiber-ferrule assembly into pH 1.3 HNO3 for 30 min. The doped PANI layer served as a conducting layer to discharge electrons. On top of the doped PANI is another PMMA layer of thickness 70 nm (2 % PMMA spin speed: 8000 rpm, spin time: 80 s prebaked at 150 ^{0}C for 5 min). On top of the second PMMA layer is a 30 nm thick layer of HSQ (available as 6% XR-1541 from Dow Corning, spin speed: 5500 rpm, spin time: 80 s prebaked at 150 ^{0}C for 3 min) for negative tone EBL. Figure 20c shows smooth coating of the four polymer layers on the fiber surface.

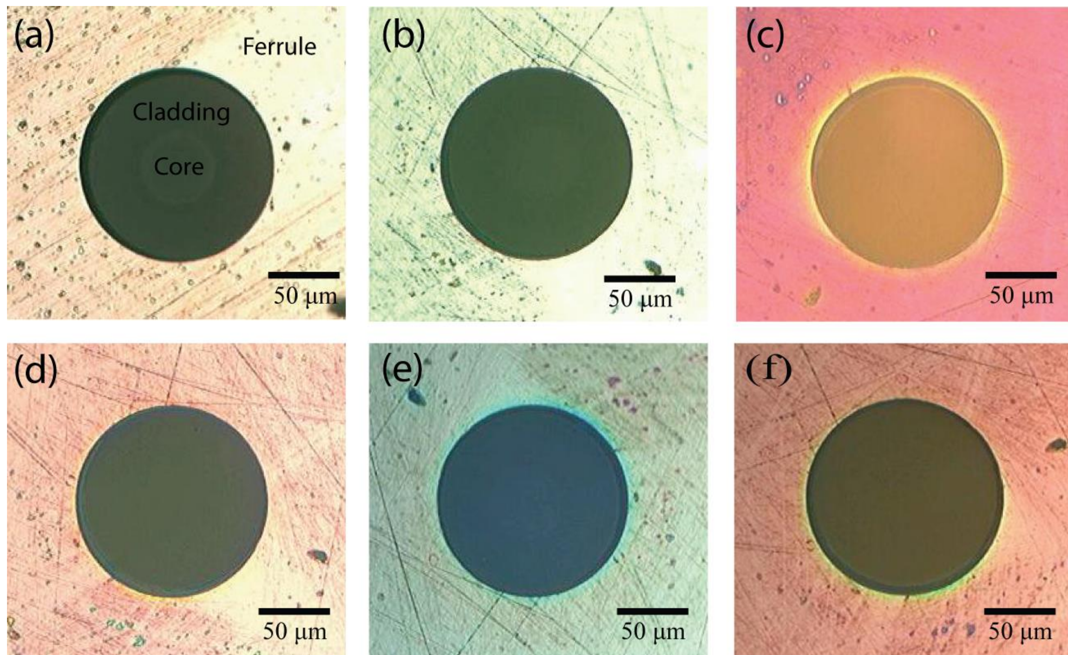

Figure 20: (a) Optical microscope image of polished optical fiber without coating. (b) First spin coated layer of 90 nm PMMA, (c) second spin coated layer of 100 nm PANI (on top of PMMA), (d) doped PANI, (e) third spin coated layer of 70 nm PMMA (on top of doped PANI) and (f) final spin coated layer of 30 nm HSQ (on top of PMMA). The smoothness and variation of the coating thickness of each layer is ~ 5 nm based on AFM measurement.

4.3.2.3 Alignment of the substrate during e-beam writing

The patterns written at the end of the optical fiber with EBL should be precisely aligned with respect to the center, which is also the symmetric axis, of the optical fiber. To achieve a precise alignment, low magnification scanning electron microscope (SEM, JEOL-6460 SEM system adopted for EBL) imaging with low current (700x, 8 pA) is applied to monitor the position of the sample in the window of the e-beam writing. With the in-situ inspection, the center of the MZP pattern precisely overlapped with the center of the optical fiber and then the e-beam writing is carried out with a beam current of 9 pA under optimized dose at a magnification of 2000x. The exposed HSQ is developed in 0.23 N TMAH (Shipley MF-319) at room temperature for 60 s followed by a rinsing and blow drying with DI water and N2 respectively.

4.3.2.4 Metal coating and lift-off

The developed sample is etched with O2 plasma (March Plasma System CS-1701. The O2 plasma etching parameters for the process were: pressure = 100 mTorr, O2 flow rate = 20 sccm, RF power = 150 W and etch time = 40 s). The etch time is calibrated with high resolution SEM images of undercut profiles obtained after different etching times as shown in the Figure 21. The patterned HSQ layer acted as an etch mask during plasma etching allowing the designed pattern to be transferred to the underlying resists (i.e., PMMA/PANI/PMMA trilayer). A 200 nm thick metal film (i.e. copper in this study) is then deposited on the entire region (BOC Edwards 306 vacuum thermal deposition at a pressure of 10-6 Torr and at a deposition rate of ~ 0.02–0.1 nm/s). The metal deposited on top of the HSQ patterns is lifted-off with NMP which can dissolve both PMMA and PANI. To achieve optimized life-off process with minimum metal re-deposition, the sample is first immersed in NMP at 80 ^{0}C for 5 min and then immersed in an inverted form in an NMP ultrasonic bath for 5 s. The sample is cleaned with acetone and blow dried in N2 at the end of the lift-off.

The fabrication results of the MZP at the end face of the optical fiber along with the characterization of its optical performance are described as follows:

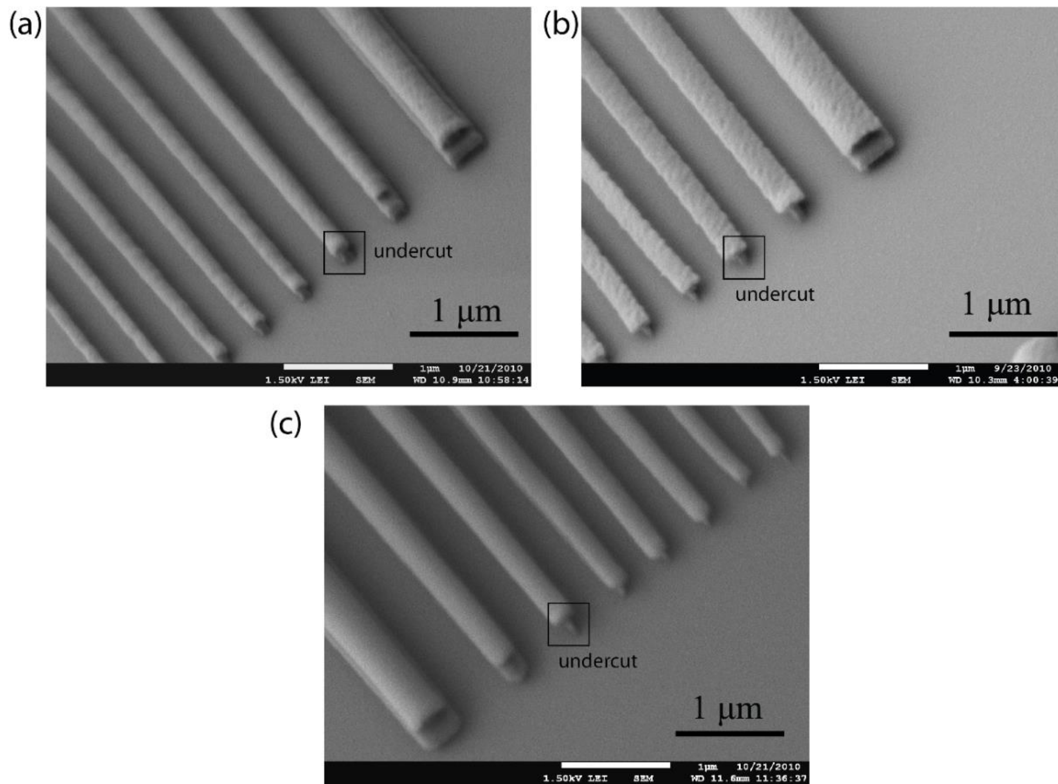

Figure 21: SEM image depicting undercut of the PMMA/PANI/PMMA trilayer after an etch time of (a) 60 s (b) 70 s (c) 80 s.

4.4 Fabrication of MZP optical probe

The fabrication procedure described in the previous section is applied for fabricating a copper MZPs consisting of 50 zones and 8 zones at the end face of a multimode optical fiber (core diameter ~ 50 μm and cladding diameter ~ 125 μm). The width of the outermost zone of the MZP (which is also the smallest structure of the designed MZP) is ~ 200 nm. Figure 22 shows the SEM image of the fabricated MZP. The width of the zones of the MZP after the fabrication is within an error of < 5 % compared to the design values. The center of the MZP is exactly at the center of the optical fiber. The accuracy and precision of the fabrication suggests that the four layered method adopted in this study can effectively minimize the possible charging and proximity effects that occur during the e-beam patterning on dielectric optical fibers. The resulting structure can sustain long time

sonic cleaning with acetone and formic acid (MS-111 from Miller Stephenson Inc., a solvent for epoxy). The removal of the fiber from the ferrule is achieved by thermally softening the epoxy with a propane flame applied to the sidewall of the ferrule assembly. The fabricated fiber can be easily detached from the ferrule once the epoxy is softened. An optical microscope image and SEM image of the detached fabricated optical fiber without polymer jacket is shown in Figure 22.

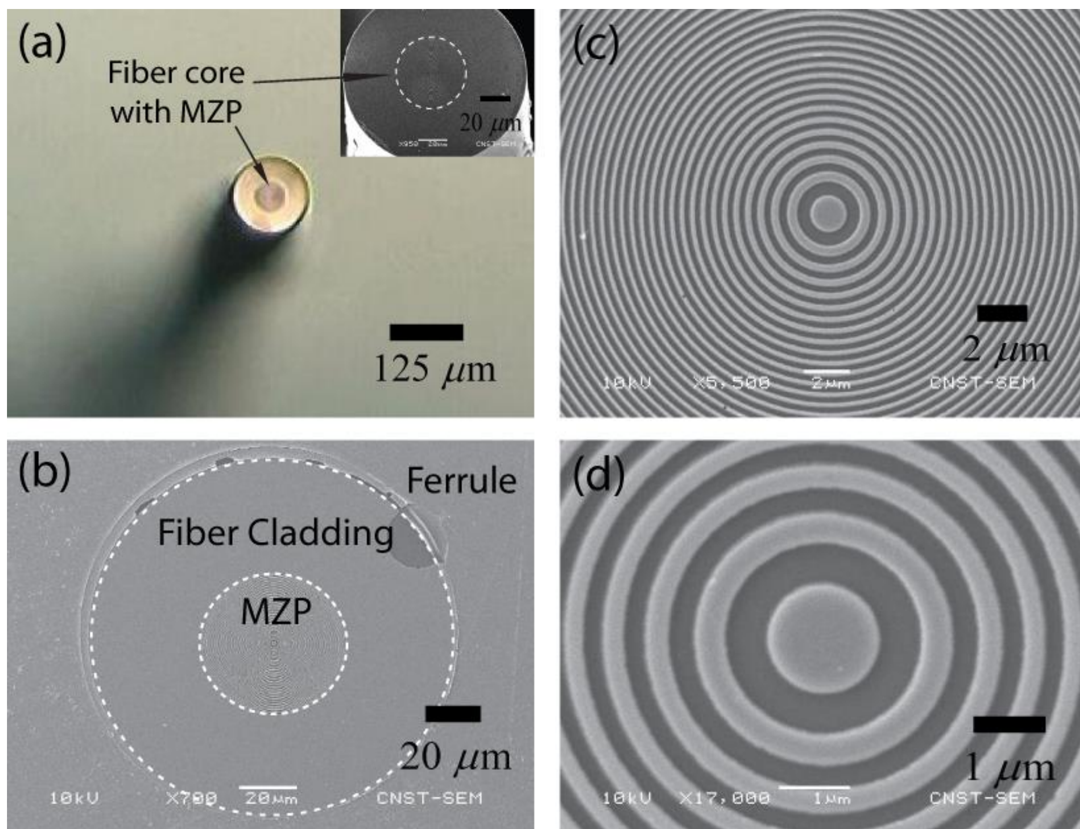

Figure 22: (a) Optical image of detached optical fiber with fabricated MZP (inset) corresponding SEM image. (b), (c), (d) SEM images of the fabricated MZP on the face of the optical fiber at different magnification ratios.

4.5 Light focusing with MZP Probe

4.5.1 Theoretical prediction of light focusing with MZP probe

The light propagation and focusing of the designed MZPs at the end of the optical fiber is characterized with a full wave based electrodynamics simulation based on finite element (FEM) method. A commercially available finite element Maxwell equation solver is adopted in the numerical simulation. A 2D axis symmetric domain is applied consisting of a multimode optical fiber with 50 μm diameter core and 40 μm thick cladding. A 50 zone copper MZP is constructed at the end of the optical fiber with the zone dimensions obtained from equation 14. TM01 mode is applied as the input field to the optical fiber. Figure 23 shows the simulated field distribution after passing through the MZP. Based on the simulated field distribution, the location of the focus spot (corresponding to the peak intensity of the focused light) occurs at f ~ 3.1 μm which is a little shifted from the design focal length of f = 3 μm. The FWHM of the spot is ~ 300 nm, which is smaller than the incident wavelength. The efficiency of the MZP working with the fundamental mode TM01 is ~ 15% based on the FEM simulation, which is close to the efficiency of regular Fresnel zone plate with plane wave illumination (< ~ 20%). Note that light focusing with the designed MZP showed little dependence on the constructing material of the MZP as long as the metal film of the MZP is optically thick.

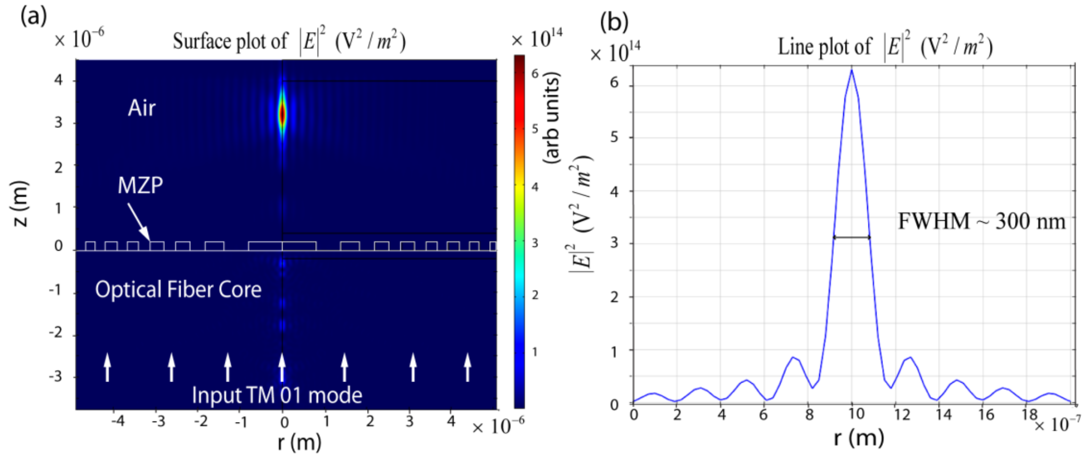

Figure 23: (a) Intensity distribution after passing through the MZP. (b) Intensity profile at the focal length (i.e. z = 3 μm) of the MZP. The FWHM obtained from simulation is ~ 300 nm.

4.5.2 Experimental performance of fabricated MZP

The focusing capability of the fabricated MZP at the end of the optical fiber is experimentally measured with two different methods namely (a) confocal laser scanning microscope (CLSM, Leica TCS SP5 coupled with 0.9 NA objective lens) and (b) collection mode NSOM imaging (Nanonics Multiview 2000, aperture diameter ~ 150 nm). A detailed description of the experimental setup and imaging methodology using each of these techniques can be found in the Appendix. Both imaging techniques provide the light intensity profile at each plane in parallel to the surface of the MZP [91, 92]. The 2D intensity profiles of the focused light at different focusing distances with the CSLM for a 50 zone copper MZP when λ = 400 nm are illustrated in Figure 24. The highest intensity (which is the location of the focus spot) appears at z ~ 3 μm, which is consistent with the results of the numerical simulation.

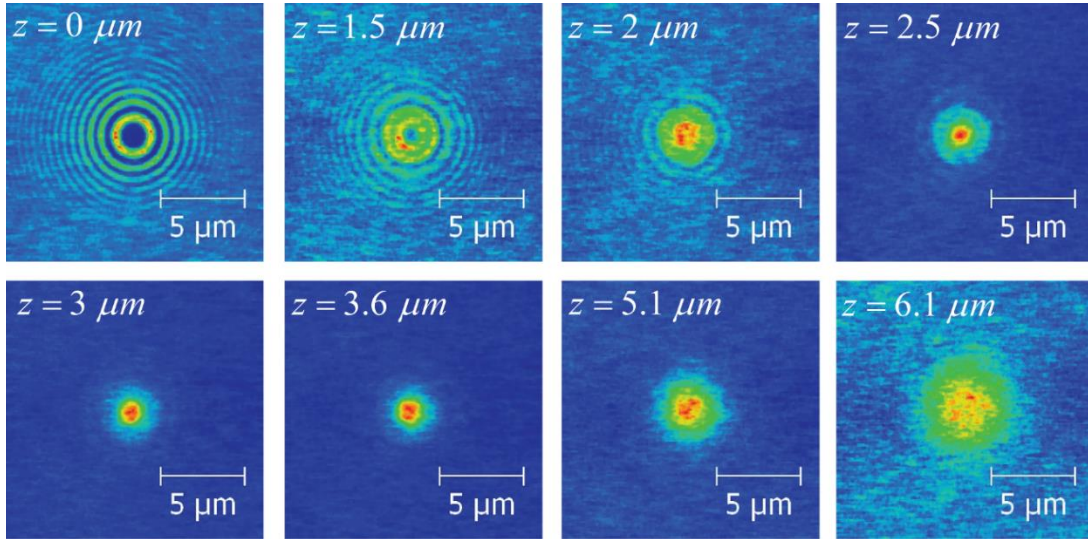

Figure 24: Confocal image of 2D light intensity distribution at different focusing z planes of the MZP.

Figure 25 shows the intensity distribution at different z planes after passing through a copper MZP consisting of 8 zones when the incident wavelength λ = 400 nm. The experimentally measured focal length (location of highest intensity) agrees with the design value of f ~ 3 µm. In Figure 26 the copper MZP is replaced with a phase MZP with 8 zones. Note that in a phase MZP the dark zones (which block the light) are replaced with transparent fused silica zones, the thickness of which is designed to provide the required additional 180º phase shift for constructive interference at the focus. In order to fabricate the phase MZP, the traditional MZP is first fabricated with the negative tone lift-off of 100 nm thick Cr film on a fused silica substrate. The Cr film acts as an etch mask for the pattern transfer of the zone to the underlying fused silica substrate (or optical fiber) by reactive ion etching with CHF_3 plasma (pressure: 10 mT, power 150 W, flow rate: 20 sccm). The chromium film is then removes by wet etching with Cr etchant. To prevent leakage of light through the sides of the phase MZP, the region surrounding the phase MZP is coated with Cr thin film which serves as an absorbing layer. This is accomplished by first coating the entire sample with 200 nm thick Cr film by thermal evaporation

followed by a selective chemical wet etching process called the Fulton-Dolan process [93]. The phase MZP offers a higher transport efficiency and hence higher light intensity at the focus spot as shown in Figure 26. The experimentally measured focal length of the phase MZP also agrees well with the design focal length of f ~ 3 μm.

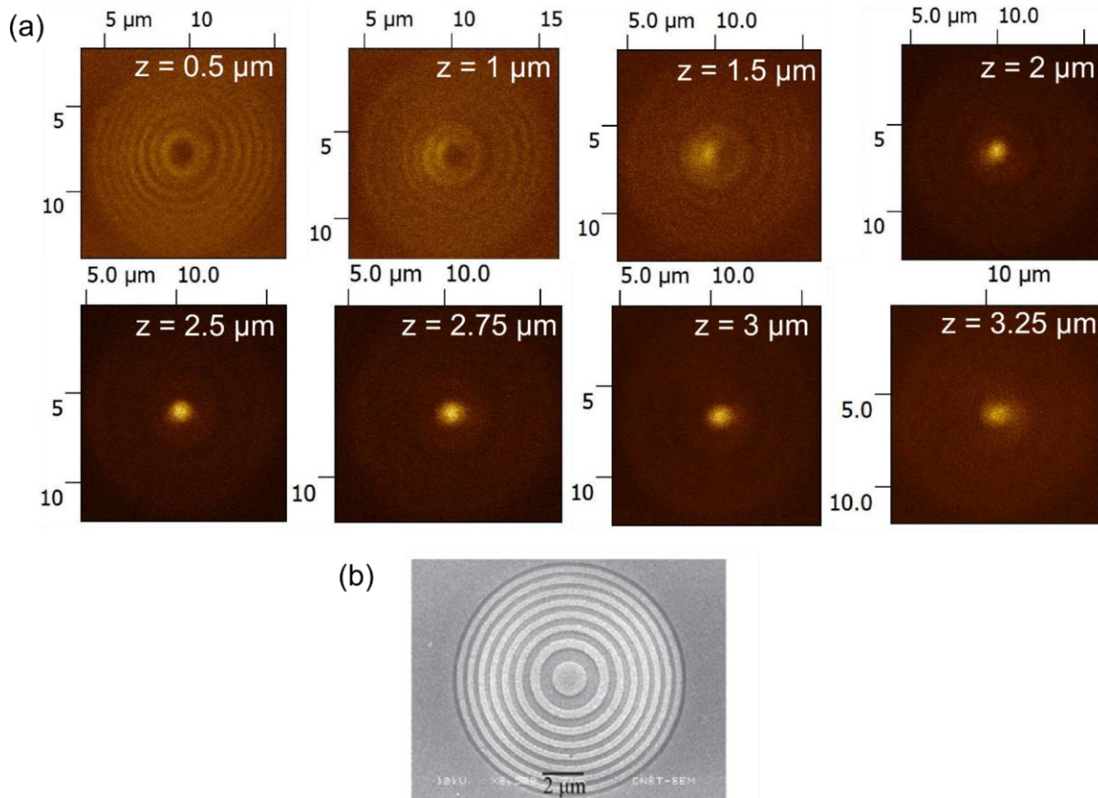

Figure 25: (a) NSOM images of light intensity distribution at different z planes after passing through the MZP (b) SEM image of MZP used for the NSOM images.

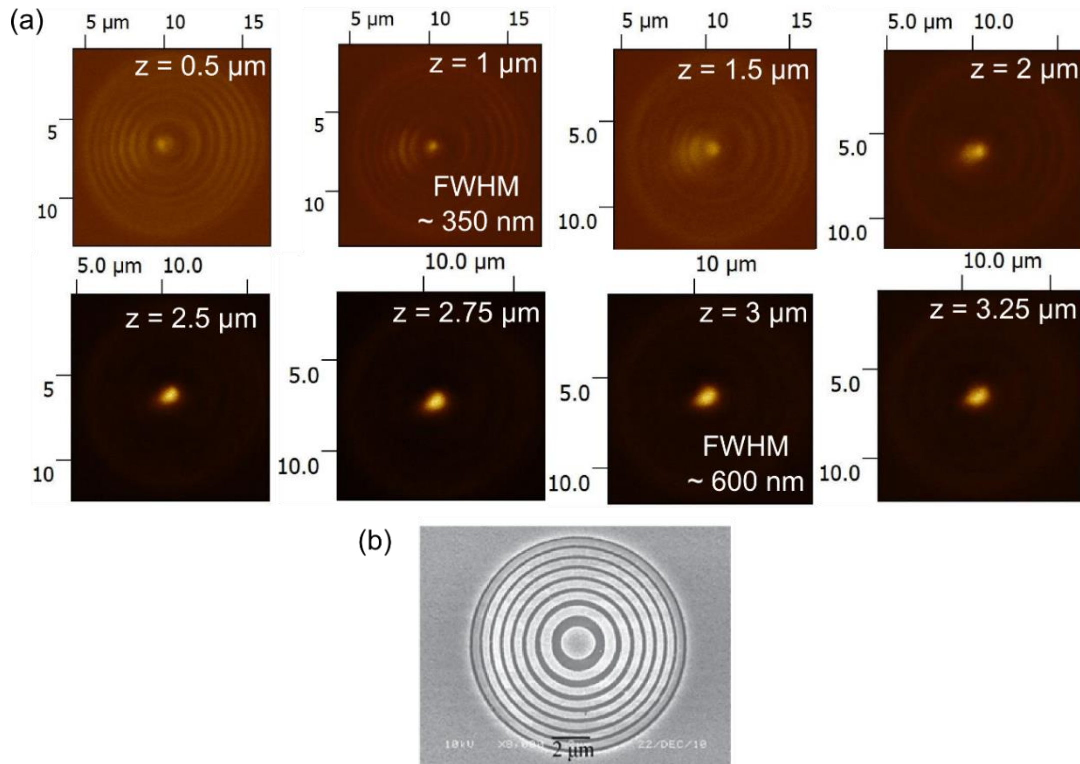

Figure 26: (a) NSOM images of light intensity distribution at different z planes after passing through the phase MZP (b) SEM image of phase MZP used for the NSOM after CHF3 etching and Fulton Dolan process.

4.6 Summary

A binary phase plate diffractive optical device, MZP, consisting of transparent and opaque zones is designed, fabricated and characterized. The focusing characteristics of the MZP designed based on optical ray theory is verified with a full wave based electrodynamics simulation.

In order to fabricate the designed MZP as a probe on the end face of an optical fiber, a novel fabrication method for constructing nano-patterns at end faces of optical fibers based on negative tone e-beam lithography is developed. The new method provides two main advantages compared to existing techniques: (a) the fabrication causes minimum damage of the base substrate (i.e., optical fiber) and (b) the constructed nano-patterns, through a

standard deposition process, have a strong adhesion to the optical fiber suitable for high temperature and high stress operation conditions. Note that, in addition to fabricating MZP probes, the proposed fabrication technique can be applied to fabricate surface plasmon resonators, localized plasmon resonators, photonic crystals and micro lenses at the end faces of optical fibers which have applications in optical-trapping and guiding, remote sensing, detection, optical processing and microscopy.

Copper MZP probes consisting of 50 zones and 8 zones are fabricated at the end face of a multimode optical fiber with this new technique and show a good consistency with the designed dimensions. The focusing characteristics of the fabricated MZP probes are verified with CSLM and collection mode NSOM imaging. The location of highest intensity (i.e. focal length), as well as size of the focus spot are consistent with results obtained from numerical simulations. A phase MZP with higher optical throughput is also constructed with the same technique and characterized with the NSOM. The MZP probes can be attached on to micro tuning forks used in NSOM systems as high energy throughput scanning optical probes for nanoscale direct fabrication and scanning microscopy.

While the MZP probe has advantages such as high energy throughput and long working distance (~ 5-10λ), it is primarily composed with metallic structures which can undergo joule heating. Also, the MZP probe is not suitable for sub 50-150 nm nanoscale light focusing since it does not rely on evanescent waves. Hence, in the following chapters, we investigate high energy throughput probes with < ~ 150 nm spatial resolution and composed purely with dielectric materials, thereby eliminating problems of joule heating during operation.

5. DESIGN AND CHARACTERIZATION OF DIELECTRIC OPTICAL PROBES

5.1 Introduction

The MZP probes designed and fabricated in the previous chapter have advantages such as long working distance (~ 10's λ) and sub-micron localization of light with high optical throughput. Compared with NSOM probes, the location of the metallic nanostructures on the MZPs is away from the focus region due to its longer focal length. However, the metallic zones of the MZP can still undergo joule heating during high intensity operation thereby limiting its application. In addition, the MZP is not suitable for deep sub-wavelength nanoscale light focusing when coupled with UV/visible light since it does not make use of evanescent waves. In some applications such as nanoscale scanning microscopy and direct fabrication, a high energy throughput probe with deep sub-wavelength spatial resolution that does not suffer from problems of joule heating is desired. Also, since the dielectric materials have almost constant optical properties (i.e. refractive index) over a wide range of visible wavelengths there are more suitable for construction of broad-band nano-optic devices operating for a wide range of wavelengths for nanoscale detection/microscopy. To prevent the above undesirable side-effects, dielectric structures can be better choices of material in constructing nano-optics. In the next part of this study, we investigate all-dielectric optical probes that can achieve nanoscale resolution.

Dielectric optics can be used as light focusing devices to achieve focus spots of different sizes ranging from 10's down to less than 0.5λ. The size of the focus spot depends on the mechanism of light focusing such as refraction, solid immersion, Mie scattering and near-field Rayleigh scattering. Among the four mechanisms listed, the dominant mechanisms

---

Part of this chapter is reproduced with permission from "*Nanoscale high-intensity light focusing with pure dielectric nonspherical scatterer*", Sundaram, V.M. and S.B. Wen, Optics Letters, 2014. 39(3): p. 582-585.Copyright 2014, The Optical Society

involved depend on different factors such as size of the dielectric optic, size of the incident beam relative to the optic, diverging/converging properties of the incident beam and polarization of the incident beam. Due to nanoscale spot sizes that can be achieved, light focusing devices based on dielectric optics of different size may be suitable candidates for the construction of broad-band optical devices for high energy throughput light focusing with minimum joule heating. In order to design the devices we first give a detailed description of the different mechanisms involved in focusing of light by dielectric optics of different sizes in the following section.

5.2 Focusing with dielectric optics

The dominant mechanisms in the focusing of light by dielectric optics depends both the size of the optic as well as the size of the illumination relative to the optic. In this section we analyze the focusing by different mechanisms namely refraction, solid immersion and scattering. In order to make the description more general, all sizes are expressed in units of the wavelength of light used i.e. λ. The light source used in the analysis has a diameter of ~ 20λ and emits a low divergence parallel beam of different polarizations namely radial and linear. Such a source can be an optical fiber which emits different modes of light with different polarization. We study three different cases depending on the diameter of the optic, d, namely, (a) d > ~ 20λ, (b) d ~ 5-10λ, and (c) d < < λ for both linearly polarized and radial polarized illumination.

5.2.1 Case (a) d > ~ 20λ

When the diameter of the optic is larger than that of the incident beam (~ 20λ), the focusing of light is mainly due to refraction of the paraxial light rays at the two spherical interfaces of the dielectric optic (Figure 27a) which focus outside the optic. Such a dielectric optic can be a ball lens with focal length (also called effective focal length, EFL, measured from the center of the lens) that is approximately predicted with geometric optics as $EFL \sim nD/4(n-1)$, where n is the refractive index of the sphere and D is the sphere diameter. The focus spot size for linearly polarized illumination is the diffraction limited Rayleigh spot size of $\sim 0.61\lambda/\sin\theta$, where θ is the half angle of the focusing light cone.

The focus spot size can be reduced further to $\sim 0.45\lambda / \sin\theta$ when the incident light is radially polarized. When the refractive index of the optic is increased, the focus spot shifts closer to the surface of the optic. For a certain refractive index, the focus spot occurs exactly at the outer surface of the optic (Figure 27b). Such a condition results in a further reduction in the spot size by a factor of n due to solid immersion effect. Note that the solid immersion spot of size $\sim 0.61\lambda / n\sin\theta$ occurs in the near field of the outer surface of the optic. The solid immersion focus spot can also be obtained when the parallel beam illumination is replaced by a focused beam. The focused beam has the additional advantage of increasing the angle θ such that sin θ ~ 1. This idea of using focused illumination to achieve a high numerical aperture will be applied in the design of the solid immersion probe in the next section of this chapter.

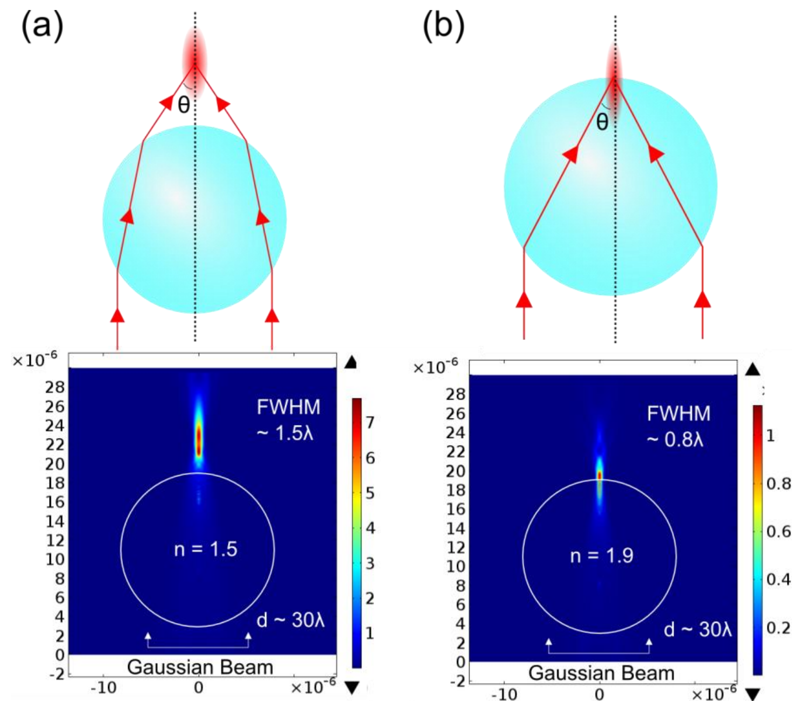

Figure 27: (a) Focusing of light by refraction with a dielectric sphere. (b) Focusing of light by refraction and solid immersion with a dielectric microsphere of high refractive index. The size of the focus spot is reduces by a factor of n due to solid immersion.

5.2.2 Case (b) d ~ 5-10λ

When the diameter of the optic is smaller than the incident beam (~ 20λ) , the illumination is similar to that of a plane wave. In this micro-optic size range of few times the wavelength of light, focusing of light is dominated by Mie scattering. Compared with case (a), the diffraction of light by the outer edges of the optic also contributes to light focusing by scattering resulting in smaller spot sizes than that predicted with geometric optics which is based on paraxial approximation. The focusing of light by dielectric microspheres to spot sizes smaller than the Rayleigh diffraction limit with Mie scattering has attracted significant attention recently and is referred to in literature as photonic jet [94-102]. The photonic jet has the following key properties, namely, The depth of focus of the photonic jet can extend more than ~2λ beyond the dielectric sphere, (2) the waist of the compressed beam can be as small as ~ λ/3, and (3) the intensity of the compressed light in the photonic jet can significantly exceed (i.e., thousand times) that of the illuminating wave.[31, 32]. Figure 28 shows the photonic jet generated with dielectric microspheres predicted with semi-analytical Lorentz Mie theory formulation (Appendix). As indicated in the figure, the focus spot size decreases with diameter of the sphere to ~ 0.37λ for sphere of diameter ~ 4λ.

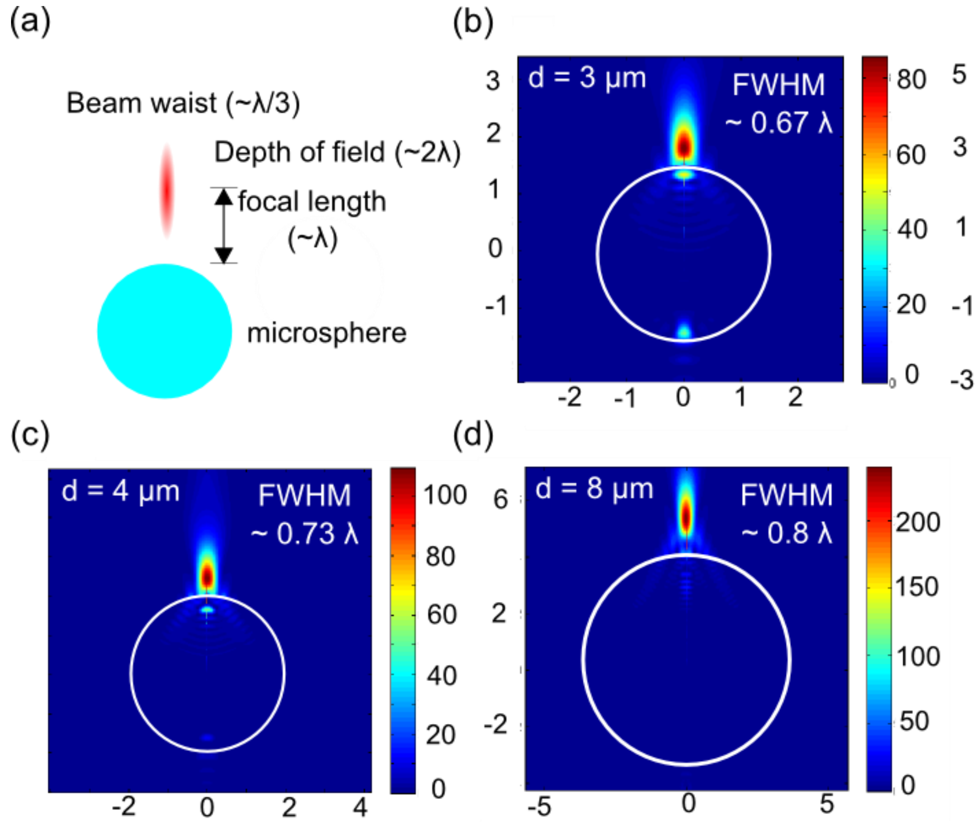

Figure 28: (a) Schematic showing focusing of light by Mie scattering with a sphere. Mie scattering results obtained from Lorentz-Mie theory for scattering of light by a sphere of diameter (a) 10λ, (b) 8λ, and (c) 4λ.

5.2.3 Case (c) d < < λ

When the optic diameter is much smaller than the incident wavelength as well as the incident beam, the interaction of the light with the micro/nano-optic is dominated by near-field Rayleigh scattering. Near-field Rayleigh scattering results in the enhancement of light intensity on the surface of the nano-optic with a spot size < ~ 10's λ. The spot size decreases with the diameter of the nano-optic. The location of the intensity enhancement depends on the polarization of the incident light. Figure 29 shows results of near-field Rayleigh scattering by dielectric nanospheres of diameter ranging from 1 μm to 60 nm. When the incident light is polarized mainly along the transverse direction (such as linearly polarized Gaussian beam) as shown in Figure 29a, for sphere diameter d < 0.6 μm, the location of the intensity

enhancement moves to the sides. For the case of longitudinal polarization (such as focused radially polarized beam) as shown in Figure 29b, the strong longitudinal field results in intensity enhancement in the forward direction. In applications of microscopy and nano-patterning, a strong confined field in the forward direction is desirable which requires the incident light to have a strong axial component such as focused radially polarized beam. This idea will be used in the construction of the scattering dielectric probe based on near-field Rayleigh scattering from dielectric scatterers in the last section of this chapter.

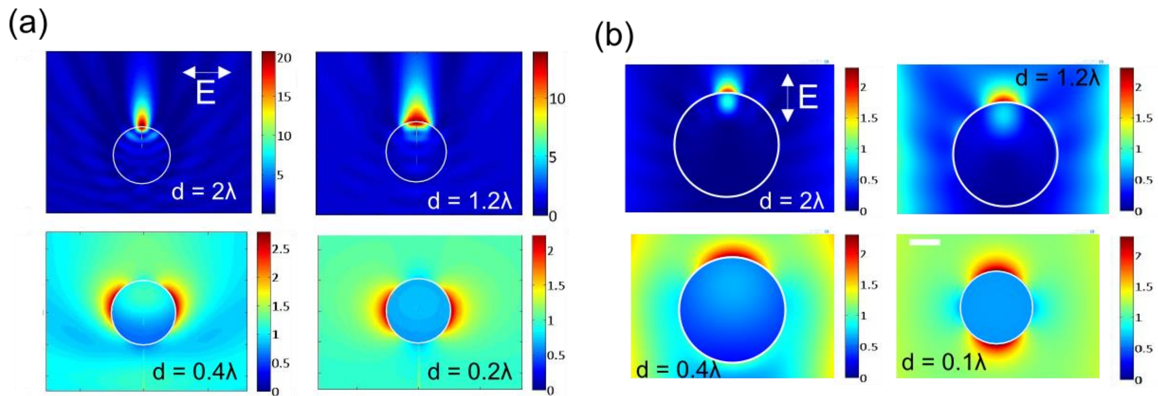

Figure 29: Focusing of light by near-field Rayleigh scattering with dielectric nanospheres of different diameters when the polarization is (a) transverse and (b) longitudinal. The polarization direction is indicated in the figure with an arrow.

The above paragraphs showed that light focusing with dielectric optics involves different mechanisms (i.e. refraction, solid immersion and scattering effects) depending on the optic size as well as size and polarization of the illumination beam. In this chapter we design optical probes with multiple dielectric spheres based on a combination of the different mechanisms described above, to achieve high energy throughput nanoscale confinement of light for applications in nanoscale patterning and microscopy. Two types of optical probes are designed and investigated, namely, (a) solid immersion probe which uses a

refractive focusing and solid immersion effect in a cascade configuration, and (b) scattering dielectric probe which uses a combination of solid immersion effect and near-field Raleigh scattering from a nanoscale dielectric scatterer.

In the following sections we provide detailed descriptions of the design and fabrication of the above two dielectric optical probes namely the solid immersion probe and scattering dielectric probe. Full wave FEM simulations are applied to validate/optimize the design of each of the probes. Both probes are assembled directly on the end face of an optical fiber which acts as the light source. The optical fiber has the advantage of providing both radially polarized (TM01 mode) and linearly polarized (HE11 mode) illumination by controlling the input mode. In addition, the resulting device on the optical fiber can be attached to a micro tuning fork in the same manner as commercial NSOM probes thereby allowing nanoscale positioning with respect to the target.

Detailed description of the design and fabrication of the first probe i.e. solid immersion probe is provided in the next section.

5.3 Solid immersion probe

In this section we construct a dielectric probe based on cascade focusing with dielectric spheres that incorporates the solid immersion effect. The probe, called as a solid immersion probe, is based on the idea that reduced spot size due to refraction based focusing combined with solid immersion effect can be achieved when a focused illumination is incident on a dielectric sphere. Since the illumination is focused the refractive index of the sphere does not have to be high as shown in the previous section. In addition, the focused illumination can provide a focusing cone angle of ~ 90 ° i.e. $\sin\theta \sim 1$. The solid immersion probe is based on a two stage cascade focusing as illustrated in the schematic ray diagram in Figure 30a. In the first stage, a dielectric sphere (referred to as ball lens) is used to focus all the light emitted from an optical fiber to a focus spot outside the lens. Since the size of the ball lens is larger than the core of the optical fiber,

the focusing is dominated by refraction on the front and back spherical surfaces. The size of the focus spot obtained from the first stage in air is ~ 0.61λ/sin θ for linear polarized illumination. The second stage of the probe is a smaller dielectric sphere (referred to as microsphere) placed close to the focus location of the ball lens such that the combined focus occurs on the outer surface of the microsphere resulting in solid immersion. The gap between the two spheres is filled with an index matching material that minimizes refraction and also holds the microsphere at the desired separation from the ball lens. The second stage with a microsphere provides two reductions in the size of the focus spot, namely (a) the solid immersion effect reduces the focus spot by a factor of n, the refractive index of the microsphere, and (b) the two stage focusing with the ball lens and the microsphere pushes the focusing cone angle to ~ 90 °. The resulting spot size from the probe is expected to be ~ 0.61λ/n for linear polarized illumination. If the illumination light from the optical fiber is changed to a radially polarized mode (i.e. TM01 mode), the spot size can be ~ 0.45λ/n. For silica sphere with n ~ 1.5, the focus spot obtained from the solid immersion probe can be ~ 0.3λ.

In the actual construction of the solid immersion probe in this study, we use an optical fiber with core diameter ~ 25 μm and the ball lens of the diameter of ~ 29 μm (refractive index ~ 1.9) (Figure 30b). A microsphere of diameter ~ 3 μm and refractive index n = 1.5 is used as the second stage of the solid immersion probe. A photopolymer pedestal structure is generated above the ball lens to hold the microsphere. In order to achieve the smallest possible focus spot from solid immersion effect, the separation distance between the ball lens and the microsphere i.e. the height of the photopolymer pedestal structure has to be accurately determined. We perform parameterized full wave electromagnetic simulations using FEM to determine the exact height of the photopolymer pedestal structure (i.e. the separation distance between the ball lens and the microsphere) to achieve the smallest solid immersion focus spot. A detailed description of the simulation condition and results is provided in the next sub-section.

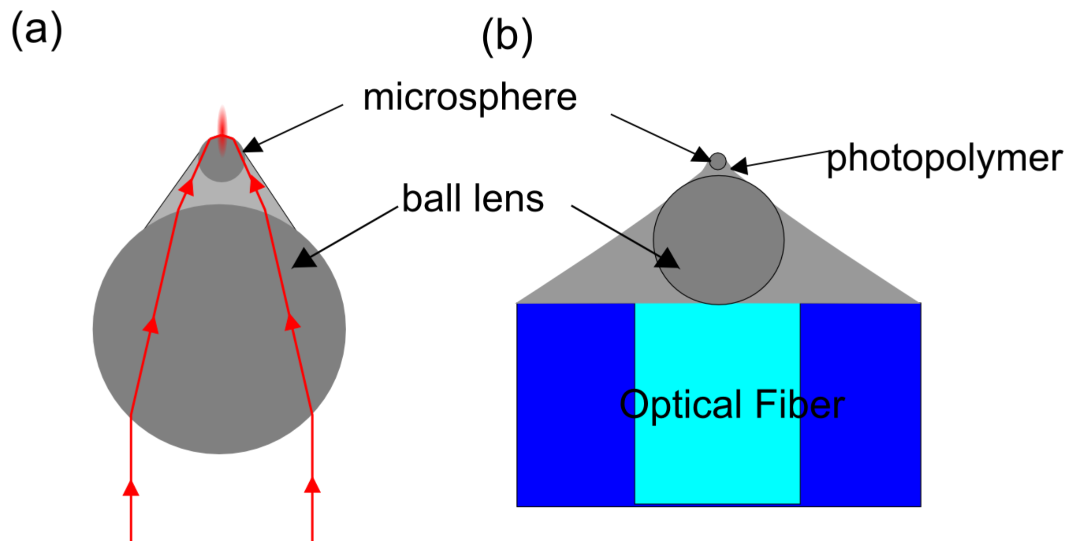

Figure 30: Schematic showing (a) focusing of a light ray by a cascade arrangement of two dielectric spheres used in the solid immersion probe and (b) the constructed solid-immersion probe on an optical fiber

5.3.1 Numerical analysis of solid immersion probe

FEM based full wave simulation is used to numerically determine the focusing characteristics of the solid immersion probe. The simulation domain consists of an optical fiber with a core diameter of 25 μm and cladding diameter of 125 μm. A high refractive index ball lens (barium titanate glass, n = 1.9) of diameter 29 μm is mounted on the core of the optical fiber. In order to match the simulation conditions with the real experiment, the region surrounding the ball lens is filled with a material of refractive index n = 1.42 (i.e. the index matches that of NOA-142 which is used in the probe construction as described in the next section). The photopolymer used to construct the pedestal structure to hold the microsphere is also composed of the same material with refractive index n = 1.42. A silica microsphere (n = 1.47) is mounted on top of the photopolymer structure. The microsphere is semi-immersed in the same epoxy of refractive index n = 1.42 which holds the microsphere on top of the photopolymer structure. The height of the photopolymer structure is varied to determine the height that will produce the smallest focus spot. TM01 mode of wavelength λ = 500 nm is applied as the input field to the

optical fiber. Figure 31 shows the simulated intensity distribution of the solid immersion probe. Based on the simulation, the highest intensity focus spot of FWHM ~ 150 nm (i.e. ~ 0.3λ) occurs on the surface of the microsphere. The corresponding height of the photopolymer pedestal structure can be between 5-6 μm from the surface of the ball lens. The intensity at the focus spot is 4 orders higher than that of the incident light in the optical fiber.

In the next section we describe the methodology for construction of the solid immersion probe. In addition, the focusing characteristics of the probe are characterized with CSLM.

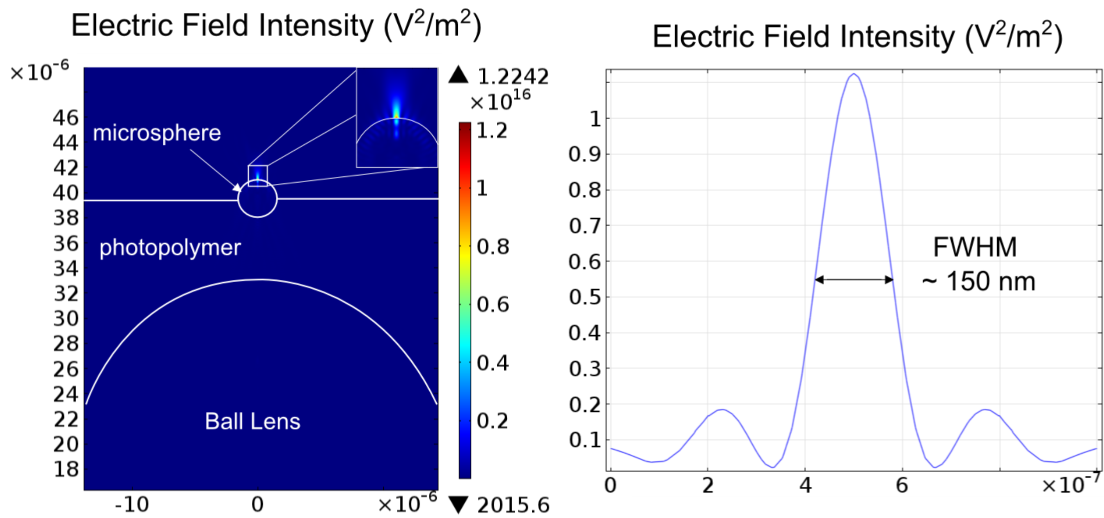

Figure 31: Simulated intensity distribution of light focusing by solid immersion probe. The intensity profile at the focus region is also shown.

5.3.2 Fabrication and characterization of solid immersion probe

The fabrication of the solid immersion probe consists of three main steps, namely, (a) mounting of the ball lens on the core of the optical fiber, (b) generation of the photopolymer pedestal structure of desired height, and (c) mounting of the microsphere

on the photopolymer pedestal structure. A detailed description of the procedure used for each of these steps is described in the following paragraphs.

Before assembly of the solid immersion probe, the end face of the optical fiber has to be both flat and clean. In order to achieve an optically flat fiber face, the fiber is integrated with ferrule and manually polished with 5 µm, 2 µm and 0.2 µm lapping films. The polished fiber is detached from the ferrule and washed in piranha solution (3:1 ratio of H_2SO_4 and H_2O_2) for 5 min. The polished and cleaned fiber is used to construct the solid immersion probe. Figure 32 is a schematic illustration of the procedure that is followed to mount the ball lens on the core of the optical fiber. The ball lens is attached to the optical fiber with a UV curable epoxy NOA 142 (Norland Optical Adhesives, n ~ 1.42 after curing). The ball lens used in this study is a 29 µm diameter barium titanate ($BaTiO_3$) glass sphere or bead (Corpuscular Inc) with a refractive index of ~ 1.9. In order to attach the ball lens to the optical fiber, the entire optical fiber is first immersed into the epoxy (NOA-142) solution resulting in a droplet that covers the entire face of the optical fiber (Step 1 in Figure 32). Next, the epoxy coated optical fiber face is made to approach the surface of a teflon wafer with a mono-disperse single layer of 28 µm spheres. The optical fiber is approximately centered to one of the spheres with the help of a precision translation stage (Step 2 in Figure 32). After centering, the epoxy coated fiber is made to come in contact with the sphere which is grasped onto the surface by the epoxy (Step 3 in Figure 32). The surface tension forces of the epoxy automatically center the sphere on the optical fiber surface. The alignment of the ball lens along the center axis of the optical fiber can be verified by coupling light through the optical fiber and checking the symmetry of the focused light.

After the epoxy holding the ball lens has set on exposure to UV light, the photopolymer pedestal structure has to be generated. Figure 33 illustrates the procedure applied to generate the photopolymer structure of height ~ 5-6 µm as predicted from the numerical simulation. A self-aligned process is used which ensures that the generated photopolymer

is centered along the optical axis of the ball lens as well as the optical fiber. This is done by immersing the optical fiber with the ball lens into the photopolymer (NOA 142, Norland Optical adhesives, refractive index = 1.42) solution. The ball lens is first made to contact the silicon wafer at the base of the photopolymer solution (Step 1 in Figure 33). A precision z-axis translation stage with resolution of < ~ 100 nm retracts the ball lens to a distance of ~ 5-6 μm which corresponds to the height of the photopolymer required for the solid immersion probe. A 365 nm wavelength UV LED is coupled through the optical fiber to expose the photopolymer solution for ~ 10s resulting in a pedestal structure with a flat top surface (Step 2 in Figure 33). The optical fiber is then retracted from the solution cleaned with isopropyl alcohol to remove the excess unexposed photopolymer solution (Step 3 in Figure 33).

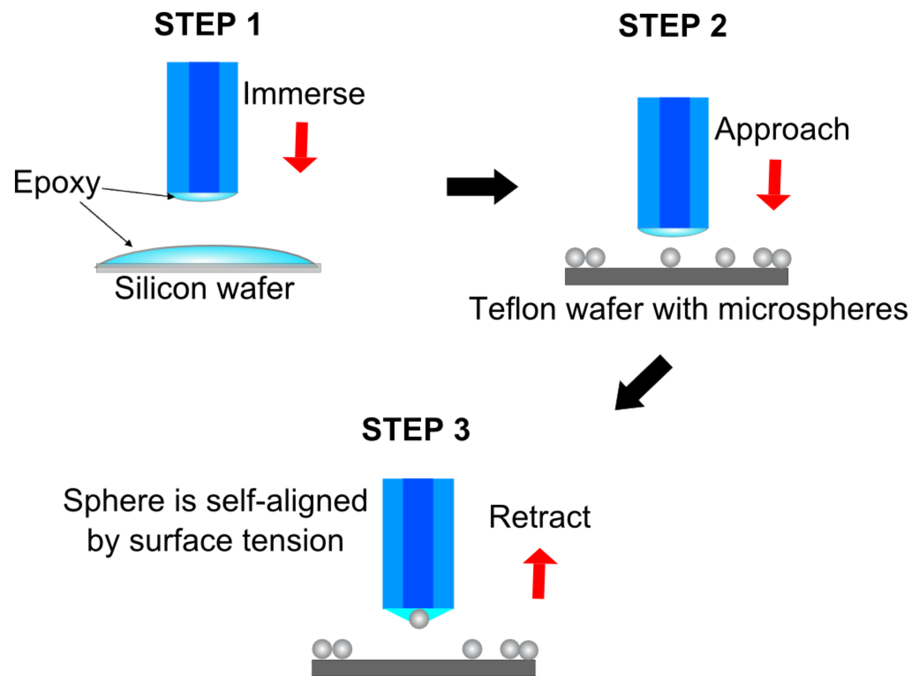

Figure 32: Illustration showing the steps to be followed for mounting of the ball lens on the optical fiber. Step 1: The fiber is immersed in epoxy to generate an epoxy droplet at the end face. Step 2: The optical fiber with the epoxy droplet is centered on one of the microspheres with a precision translation stage. Step 3: The fiber comes in contact with the sphere which is grasped onto the fiber surface by the epoxy.

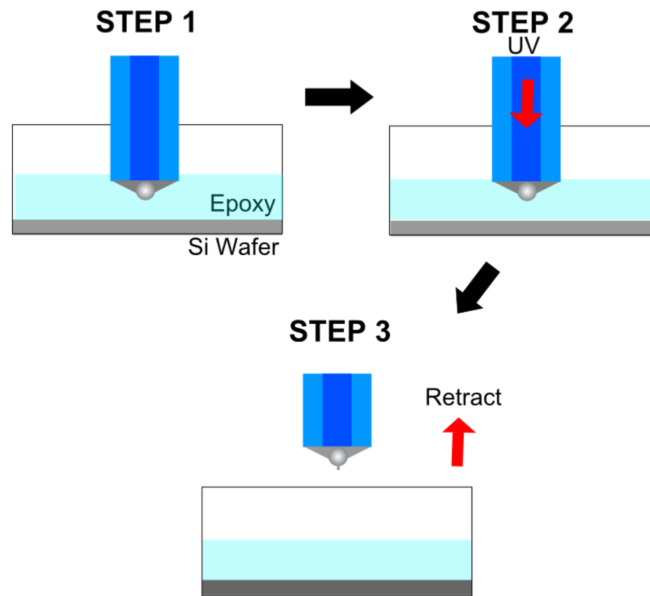

Figure 33: Illustration showing the steps to be followed for generation of the photopolymer pedestal structure. Step 1: The fiber with the ball lens is immersed into the epoxy and made to contact the silicon wafer at the bottom. Step 2: The fiber is retracted with a precision z-translation stage to ~ 5-6 µm which corresponds to the height of the photopolymer structure to be generated. UV light is coupled to the optical fiber to generate the structure. Step 3: The fiber is retracted from the solution and cleaned to remove excess uncured epoxy.

Note that since the refractive index of the ball lens is larger than that of the photopolymer, the light is focused in the photopolymer solution by the ball lens giving the cured photopolymer a tapered structure. The diameter of the top surface of the pedestal structure is ~ 3 µm when a ~ 29 µm ball lens is used to focus the light emitted from an optical fiber of core diameter ~ 25 µm. The diameter of the top surface can be reduced by reducing the size of the ball lens. The next step in the fabrication of the solid immersion probe is to mount a microsphere on the photopolymer structure. The size of the microsphere is chosen such that all the light emitted from the photopolymer structure is delivered to the microsphere to form an intense focus spot on the forward surface of the microsphere. The microsphere is mounted on the pedestal structure with the same approach followed for the ball lens as indicated in Figure 32 using the same epoxy.

Figure 34c shows an SEM image of the fabricated solid immersion probe. The microsphere is semi-immersed in the epoxy over the photopolymer structure which was also assumed in the design of the probe.

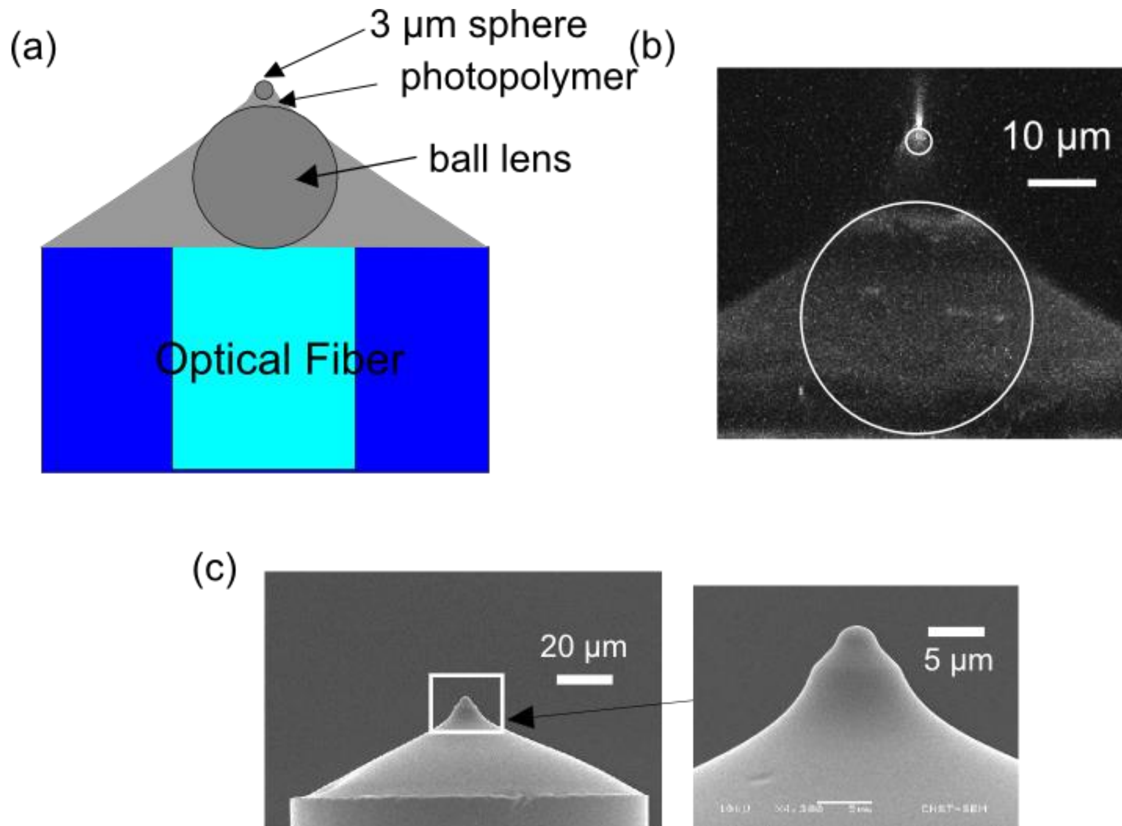

Figure 34: (a) Schematic of solid immersion probe. (b) Intensity distribution of light of wavelength λ ~ 450 nm focused by the solid immersion probe obtained from CLSM (confocal laser scanning microscope). (c) SEM image of the fabricated solid immersion probe.

The focusing of light by the solid immersion probe is experimentally verified with a confocal laser scanning microscope (CLSM). Figure 34b shows stacked images obtained from 2D intensity profiles with the CSLM for the probe with the ball lens and the photopolymer structure as well as the complete two sphere probe. The FWHM at the focus

spot which is located on the surface of the 3 μm diameter sphere is ~ 350 nm for an incident wavelength ~ 450 nm. The spatial resolution limit of the CLSM prevents the measurement of the actual spot size which is expected to be smaller due to solid immersion effect. The light from the optical fiber is focused in a cascade manner by both the ball lens and the microsphere resulting in minimum leakage as well as negligible background noise. In addition, the solid immersion probe has a gradually tapering structure with the 120 μm diameter optical fiber followed by the ~ 30 μm diameter ball lens, ~ 5 μm diameter photopolymer pedestal, 3 μm diameter microsphere and the probe diameter reaching zero at the apex of the microsphere. The gradually tapering tip-like structure of the solid immersion probe allows easy positioning of the probe with a tuning fork based scanning probe microscopy system.

Probes based on solid immersion effect designed in this section can achieve spot sizes ~ $0.45\lambda/n$ on the surface of the microsphere with radially polarized illumination. However to get sub-50 nm spot sizes with visible light we have to make use of near-field effects which are generated by near-field Rayleigh scattering of light from dielectric nanostructures of sizes $< \sim \lambda$. In the next section we design probes based on a combination of solid immersion and near-field Rayleigh scattering which can achieve nanoscale spot sizes.

5.4 Scattering dielectric probe

In this section, probes based on near-field Rayleigh scattering are examined to achieve nanoscale light confinement below the diffraction limit with evanescent waves. While dielectric nanospheres with diameters smaller than or comparable to the wavelength of the incident light can achieve nanoscale confinement by near-field Rayleigh scattering, the spherical geometry of the nanoscale dielectric scatterer may not be the best optimized shape for high intensity nanoscale focusing. The goal of this part of the first part of this section is to find the geometry of dielectric scatterers that can provide nanoscale forward scattering with high focusing intensity. The resulting dielectric scatter, with minimum

joule heating, will allow high intensity high throughput nanoscale light focusing which cannot be achieved with other nano optical devices. Such dielectric scatters can be applied in establishing new scanning optical probes for super-resolution imaging, nanoscale direct-writing, nanoscale mask-free lithography, nanoscale laser spectroscopy and nano-optical tweezing which cannot be easily achieved with existing scanning optical probes [23, 103, 104]. Once the shape of the dielectric scatterer has been optimized, the scatterer is combined with a ball lens to form a scattering dielectric probe that uses both solid immersion effect and near-field Rayleigh scattering to get a focus spot ~ 10's nm.

A radially polarized beam, results in axial intensity enhancement along the propagation direction of the incident light due to forward scattering from nano-structures as described in the first section and is selected as the far field illumination [105]. More specifically, radially polarized Bessel beam, which can be generated with axicons and optical phase plates is adopted [106, 107]. The electric field of the radially polarized Bessel beam can be expressed as [108]

$$E_r\left(r,z\right) = E_o \cos(\alpha)\sin(\alpha)J_1\left(k\sin(\alpha)r\right)e^{-j\left(k\cos(\alpha)-\omega t\right)}, \tag{15}$$

$$E_\phi(r,z) = 0, \tag{16}$$

$$E_z\left(r,z\right) = -iE_o \sin^2(\alpha)J_0\left(k\sin(\alpha)r\right)e^{-j\left(k\cos(\alpha)-\omega t\right)} \tag{17}$$

where α is a parameter determining the period of the Bessel beam. In this study, $\alpha = 3.5°$ corresponds to an axicon angle of 173° which is used in many Bessel beam experiments. The wavelength of the light is selected as $\lambda = 532$ nm and the dielectric constant of the scatterer is $\varepsilon = 1.96$ (close to silica) at $\lambda = 532$ nm. A full wave analysis with finite element method (FEM) is adopted to determine scattered field distribution of spherical dielectric spheres with radial polarized illumination.

5.4.1 Case 1: Light scattering from dielectric nanospheres

Table 2 is the summary of the FEM results (Figure 35) for scattering from dielectric spheres with different radii (10 nm < r < 500 nm). The spot size is defined as the full width

at half maximum (FWHM) at the focusing plane of maximum intensity (henceforth referred to as the focus spot). The intensity enhancement is defined as the ratio between the intensity at the focus spot and incident intensity. The depth of field is defined as the distance from the focus spot to the position along the optical axis where the spot size is doubled in scattered field. The scattering cross-section is computed from the Mie solution which governs the scattering behavior of spheres of all diameters [109, 110].

Table 2: Scattering from dielectric spheres.

Sphere Radius (nm)	**Intensity Enhancement**	**Spot Size (nm)**	**Depth of Field (nm)**	**Scattering Cross Section (μm^2)**
10	2.18	10	10	9.5×10^{-9}
30	2.28	30	35	6.9×10^{-6}
50	2.45	45	50	1.47×10^{-4}
100	3.26	80	60	7.56×10^{-3}
300	32.5	170	160	0.872
400	97.5	180	180	2.03
500	240.0	180	220	2.96

The FEM results fit well with previous published data [95]. The results in Table 2, indicate that the spot size of forward scattering, depth of focus, scattering cross-section as well as the intensity enhancement increase monotonically with respect to the radius of the sphere.

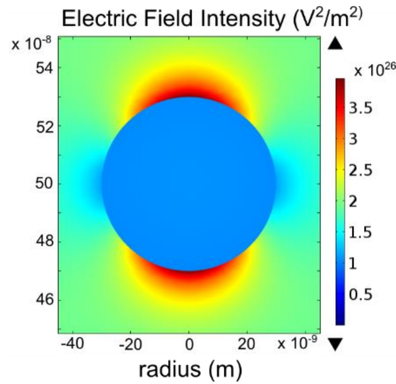

Figure 35: Plot of electric field intensity distribution of a spherical scatterer with a radius= 30 nm. Reprinted with permission from [111].

Based on the results, for a dielectric sphere, a small spot size can be achieved by reducing the diameter of the spherical scatterer. On the other hand, maximum intensity enhancement at the confined spot can be achieved by choosing spherical scatterers with larger diameter. To achieve the goal of this study which is to construct a dielectric based scatterer that can achieve both small spot size and high focusing intensity, a non-spherically symmetric scatterer will be required. With an assumption that the spot size is mainly determined by the forward area of the scatterer and the intensity enhancement is mainly determined by the backward area when the scatterer radius is around or less than the incident wavelength, we propose that a 'snowman' scatterer, which is a combination of a large and small spheres, can provide large backward scattering area and small forward scattering area to achieve small spot size with high focusing intensity. In the next section, we examine the snowman scatterers with different geometric configurations (i.e., different forward and backward radii) for nanoscale light focusing.

5.4.2 Case 2: Light scattering from snowman scatterers

To verify the idea that the spot size of forward scattering with a scatterer is determined by its forward area, the snowman structure is simulated for top spheres with different radii (10 nm < r < 50 nm) when the radius of the bottom sphere is fixed at 200 nm (Figure 36a).

On the other hand, to verify the idea that the intensity enhancement of forward scattering depends on its backward area, the intensity enhancement of snowman structures is simulated for different bottom sphere radius (100 nm < r < 500 nm) when the radius of the top sphere fixed at 10 nm. The results in Table 3 and

Table 4 are in agreement with the proposed idea: for a fixed radius of the bottom sphere (200 nm diameter), the spot size increases linearly from ~ 10 nm – 50 nm when the radius of the top sphere increases from 10 nm to 50 nm (i.e. forward area of the scatterer increases); for a fixed radius of top sphere and the associated fixed focus spot size, the intensity enhancement increases from ~ 6 times to ~ 450 times when the bottom sphere radius increases from 100 nm to 500 nm (i.e. the backward area of the scatterer increases). The depth of field shows dependence only on the forward area but not the backward area. The depth of field increases monotonically with the diameter of the top sphere as observed for a single spherical scatterer in case 1. In conclusion, the spot size and depth of field of a snowman shaped scatter are mainly determined by the forward area of the scatterer when the radius of the top sphere is within the range of Rayleigh scattering (i.e., 10 nm < r < 50 nm for λ ~ 532 nm) [112]. In this size range, the focus spot and the depth of field are both reduced by decreasing the size of the top sphere in the snowman shaped scatterer. On the other hand, the intensity enhancement at the focused spot depends only on the backward area of the scatterer when the radius of the bottom sphere is within the range of Mie scattering (i.e., 100 nm < r < 500 nm for λ ~ 532 nm) [112]. The intensity enhancement can be increased by increasing the diameter of the bottom sphere in this size range.

Table 3: Scattering from snowman scatterers with different bottom sphere radii.

Radius of Bottom Sphere (nm)	**Intensity Enhancement**	**Spot Size (nm)**	**Depth of Field (nm)**
100	5.7	10	10
200	16.7	10	10
300	60	10	10
400	187.4	10	10
500	450	10	10

Table 4: Scattering from snowman scatterers with different top sphere radii.

Radius of Top Sphere (nm)	**Radius of Top Sphere (nm)**	**Radius of Top Sphere (nm)**	**Radius of Top Sphere (nm)**
10	10	10	10
20	20	20	20
30	30	30	30
40	40	40	40
50	50	50	50

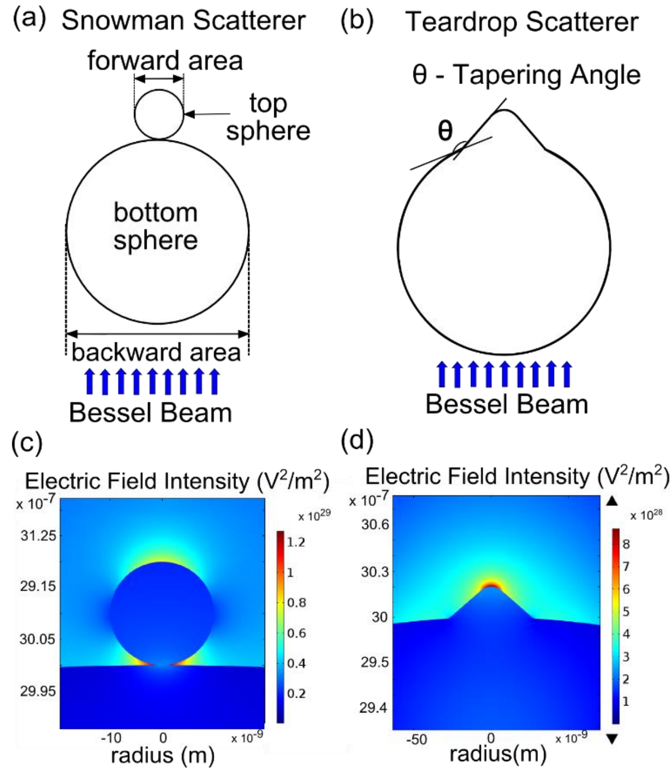

Figure 36: (a) Schematic of snowman configuration of scatterer (b) Schematic of teardrop configuration indicating th tapering angle. (c) Plot of electric field intensity of snowman scatterer with top sphere radius 10 nm and bottom 500 nm. (d) Plot of electric field intensity of teardrop scatterer with top sphere radius 10 nm and bottom 500 nm and tapering angle of 145°.Reprinted with permission from [111].

Figure 36c shows the light intensity distribution when the radius of the top and bottom sphere of the snowman scatterer are 10 nm and 500 nm respectively. Light is confined at the apex of the snowman structure to a spot size of ~ 10 nm with an intensity enhancement of ~ 450 times. However, the highest intensity occurs at the gap between the top and bottom sphere where the geometric angle is the smallest. This strong localized field enhancement away from the apex of the snowman structure is not desired in most applications. Therefore, a modification of the snowman configuration has to be implemented to shift this highest intensity region from the side of the scatter to the apex of the snowman structure. A direct approach which does not affect the forward/backward

radius as well as the forward/backward scattering area of the snowman scatter would be filling the side gap of the snowman scatter with dielectric material. The resulting modified snowman scatter has a teardrop shape as in (Figure 36b), and is named as teardrop scatter in the following discussions. In the next case, we examine the field distribution of teardrop structures under the same radially polarized illumination.

5.4.3 Case 3: Light scattering from teardrop scatterers

To prevent the occurrence of the off-axis intensity enhancement as in the snowman shaped scatterer, the side gaps of the snowman structure (where the highest intensity occurs) are filled with dielectric material. The filling with different tapering angles is obtained by drawing a tangent to the top sphere of the snowman scatterer from different locations on the circumference of the bottom sphere (Figure 36b). The scattered fields of the resulting teardrop structures with bottom and top sphere radii of 500 nm and 10 nm respectively and tapering angle varying from 90° to 160° are examined with FEM simulation. Figure 36d shows the resulting intensity distribution when the tapering angle is 145°. As observed in the figure, the field distribution is similar to that from a snowman scatterer with the same top and bottom radii. The only difference between the two shapes of scatterers is the diminishing of the off-axis field enhancement in the teardrop scatterer (Figure 36d) compared with a snowman scatterer (Figure 36c). Table 5 lists the spot size and intensity enhancement in the forward scattering under the different tapering angles tested in the FEM simulation. While the spot size shows no significant dependence (~ 10 nm), the intensity enhancement (> ~ 450) shows a weak dependence on the tapering angle filling the gap.

To achieve high energy transport efficiency focusing with a teardrop scatterer, external illumination delivered to the teardrop scatterer should be highly focused with a high numerical aperture lens. Light focusing with the resulting two- stage optics (macro/micro lens + teardrop scatterer) is presented in the next section.

5.4.4 Case 4: Light focusing with a combination of a teardrop scatterer and a ball lens (i.e. combined solid immersion and scattering focusing)

To provide intense illumination to induce a strong forward scattering, the teardrop scatterer is placed as the focus region of a ball lens with a radius 5 μm and dielectric constant n = 1.5 to form a scattering dielectric probe (Figure 37a). The radius of the ball lens is chosen such that the first peak of the radially polarized Bessel beam lies within the ball lens to ensure a high light intensity at the focus spot by refraction from the front and back spherical surfaces. The separation distance between tear –drop scatterer and the ball lens is adjusted to achieve a solid immersion focus spot at the location of the scatterer (which is ~ 7 μm based on the simulation). Figure 37a shows the light intensity distribution of a teardrop scatterer with a forward radius 10 nm, backward radius 500 nm, and tapering angle 145°. The total intensity enhancement at the apex of the teardrop scatterer is ~ 150000 compared with the intensity of the incident light. The spot size around the apex remains ~ 10 nm.

Table 5: Scattering from teardrop scatterer with different taper angles

Tapering Angle	Intensity Enhancement	Spot Size (nm)
90°	468	10
125°	495	10
145°	502	10
155°	490	10

Based on the above design of the combined focusing with the solid immersion and near-field Rayleigh scattering by a ball lens and dielectric scatterer, a schematic of scattering dielectric probe is provided in Figure 37b. The probe can be considered as a modified version of the solid immersion probe described in the previous section with a small dielectric protrusion on the top surface of the microsphere which acts as a teardrop

scatterer. The scattering dielectric probe can focus all the light emitted by the optical fiber to an ~ 10 nm spot with an intensity enhancement of ~ 10^5. Such a probe can be a valuable tool for high energy throughput nanoscale fabrication and scanning microscopy.

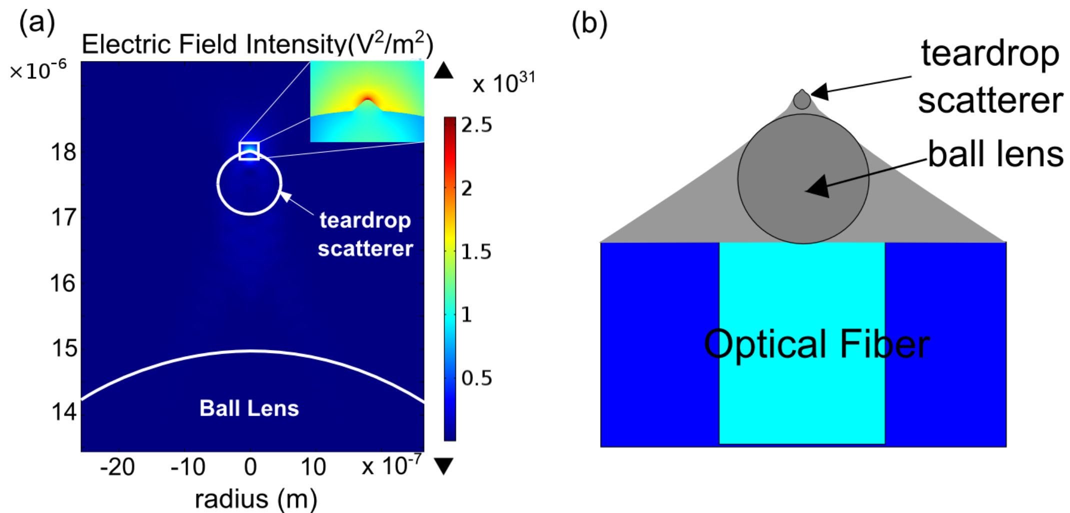

Figure 37: (a) Plot of electric field intensity distribution for cascade focusing configuration consisting of the teardrop scatterer placed at the focus region of 5 µm diameter microsphere (b) Schematic of scattering dielelctric probe that combines a tear drop scatterer with a solid-immersion probe. Reprinted with permission from [111].

5.5 Summary

In this portion of study, we design all-dielectric optical probes that achieve nanoscale confinement by focusing of the incident light with a combination of reflection, solid immersion and scattering effects. Two types of optical probes are investigated, namely a solid immersion probe and a scattering dielectric optical probe. The solid immersion probe which used a refraction based focusing can achieve a diffraction-limited spot size of ~ 0.45λ/n on the surface of the microsphere with radially polarized illumination. The solid immersion probe is fabricated and the focusing characteristics are characterized with CSLM which show good agreement with numerical simulations.

To further reduce the spot size to sub-50 nm scales, near–field Rayleigh scattering from dielectric nanostructures is investigated as a potential mechanism for nanoscale confinement. Numerical simulation is used to optimize the shape of the dielectric scatterer that can achieve an intense nanoscale focus spot for radially polarized illumination. A corresponding teardrop scatterer composing a large bottom radius (r = 200 nm) and a small top radius (r = 10 nm) can serve as an efficient dielectric scatterer to achieve small spot size with high scattering intensity. The teardrop scatterer when combined with a ball lens to form a scattering dielectric probe that combines solid immersion focusing and near-field Rayleigh scattering effect to achieve an intensity enhancement of ~ 10^5 with a ~ 10 nm spot size at the apex of the teardrop scatterer. The scattering dielectric probe can be valuable in high energy throughput nanoscale light detection, fabrication and material manipulation (e.g., nano-optical tweezing).

Both optical probes in this chapter are constructed with dielectric spheres and use a combination of refraction, solid immersion and near-field scattering effects to achieve deep sub-micron focus spot sizes with negligible joule heating. The deep sub-micron focusing resolution achieved with dielectric spheres with effects such as solid immersion and near-field scattering can be extended to imaging based on the reciprocity of linear optics. Such an application of dielectric microspheres in high resolution imaging has drawn significant attention in the recent years and has been experimentally demonstrated by many groups. In the next chapter, we investigate the mechanisms for deep sub-micron imaging with dielectric microspheres.

6. ANALYSIS OF DEEP SUB-MICRON RESOLUTION IN MICROLENSES BASED IMAGING

6.1 Introduction

In the previous chapter optical probes with dielectric spheres that use a combination light focusing mechanisms of refraction, solid immersion and near-field scattering effects to achieve deep sub-micron focus spot sizes were studied. The deep sub-micron focusing resolution achieved with dielectric spheres can be extended to imaging based on the reciprocity of linear optics. In this chapter we investigate the mechanisms of high resolution imaging with dielectric spheres.

Deep sub-micron imaging resolution with dielectric microspheres, better than that with high NA objectives, has been demonstrated by many groups in the recent years [113-119]. In most of the demonstrations, a dielectric microsphere of diameter ~ 4 – 50 μm and refractive index n ~ 1.45 is placed on the target plane as the first lens. Slightly better than ~ λ/4 spatial resolution has been consistently reported by different groups under similar experimental conditions when a high numerical aperture (NA) objective is placed along the imaging path of the microsphere to further magnify the real/virtual images from the microspheres [120].

Even with the numerous successes in deep sub-wavelength imaging with microspheres, the mechanisms providing the high spatial resolution are still under debate. Compared with macroscale lenses, microspheres have larger radius of curvature and corresponding almost zero front focal distance (FFD). As a result, the refractive index of the lens can contribute to the spatial resolution of the target (i.e., solid immersion effect) [121-123]. Also, due to the almost zero FFD, the acceptance angle of the microsphere from the target plane is ~ 90° , which results in an effective numerical aperture ~ n when the microsphere is applied in the imaging [124]. In addition, since the microsphere is in direct contact with

the target, the refractive index of the base material of the target can also affect the light diffraction and the associated imaging resolution [113, 125].

To verify the contribution of each mechanism, namely, solid immersion effect of microsphere and refractive index of base material of the target in the deep sub-micron scale imaging resolution with microspheres, numerical experiments of the light propagation from the target through a microsphere, an objective lens and then to the imaging plane are performed in this study. Compared with the hand-on experiments, the numerical experiment allows us to adjust each parameter, including the polarization of light, independently to identify their contribution to the spatial resolution in microsphere based imaging. Description of the arrangement and conditions studied with the numerical experiments are listed in the following section.

6.2 Theoretical analysis

In this study, we use full wave finite element method (FEM) simulation to identify the contributions of the refractive indices of microspheres, target and the polarization direction of the collected light on the spatial resolution of a microsphere imaging system. A schematic of the simulation domain is in Figure 38. A dipole (either x-y transverse dipole or z longitudinal dipole as illustrated in Figure 38) on the target plane with close proximity to the microsphere is selected as a point source on the target. In order to form a real image with the microsphere, a lens pair is placed above the microsphere to mimic the function of high numerical aperture objective lens in reported microsphere imaging experiments [126]. The dielectric microsphere has a diameter ~ 6 μm. The two lenses in the lens pair have diameters equal to 20 μm and 40 μm with refractive index n ~ 1.5 and n ~ 1.4 respectively. The position of the lens pair is adjusted such that the first lens collimates the light diffracted by the microsphere and the second lens focuses the collimated light to form an image on its focal plane. To study the microsphere imaging at visible wavelength, λ ~ 500 nm is selected. The simulation domain is surrounded by a perfect matching layer to approximate an open domain. Triangular mesh elements with size less than ~ λ/15 are applied around the imaging plane. For other regions, the mesh

size is less than ~ λ/10. The size of the focus/image spot is determined by measuring the FWHM of light intensity (i.e., point spread function, PSF) at the imaging plane where the FWHM of the PSF achieves its minimum value. The magnification ratio of the imaging system is determined by transverse displacement ratio between the PSF and the point dipole in the x direction when the dipole is away from the optical axis. The obtained magnification values are almost the same as the ratio between the backward focus numerical aperture (at target plane) and forward focus numerical aperture (at the imaging plane) [1, 127]. Since the microsphere is in contact with the target, the backward focus numerical aperture from the target to the microsphere is ~ n with 'n' equal to the refractive index of the microsphere. A two-point resolution criterion for point dipoles (i.e., minimum resolvable separation distance between two dipoles is equal to FWHM of point spread function (PSF) divided by the magnification ratio M) is used to determine the point dipole spatial resolution in this study [127]. The obtained results from the full wave FEM simulations along with the corresponding discussions are presented in the next section.

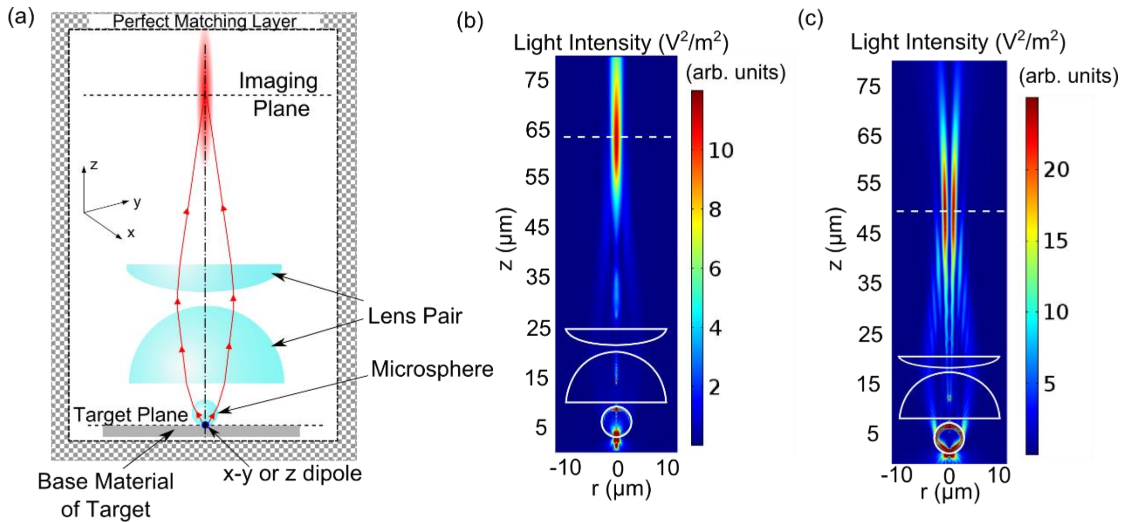

Figure 38: (a) Schematic of the simulation domain consisting of the target, microsphere and lens pair. Light intensity (~ $|E|^2$) distribution induced by (b) a transverse dipole (x-y dipole), and (c) a longitudinal dipole (z-dipole), in air with a microlens of diameter ~ 6 μm and refractive index n = 1.4. The dashed lines indicates the imaging plane

6.3 Results and discussion

Simulated imaging resolution of microspheres as a function of the refractive index of the microsphere, the refractive index of base material of the target, and the polarization of light are as follows:

6.3.1 Refractive index of microsphere

Focal plane of a spherical lens is inside the lens when its refractive index n is larger than ~ 1.5. Therefore, n < 1.5 is studied in this portion of analysis. A transverse dipole in air is selected as the point target. Light emitted from the transverse dipole, when collimated by the first lens of the lens pair in Figure 38, resembles a linearly polarized Airy beam which commonly appears in most imaging. The focus/image spot of a linearly polarized Airy beam is not axisymmetric - larger FWHM in the polarization direction and smaller normal to the polarization direction (Figure 39a). This difference becomes smaller for larger magnification ratio. Due to the limited simulation power, the magnification ratio in limited to < 10, to prevent oversized simulation domain and the correspondingly overwhelming simulation time in this study. Table 6 lists the simulated FWHM of the PSF, magnification M, and the dipole resolution at the imaging plane of the microsphere based imaging system (i.e., FWHM of the PSF divided by M) with refractive index of the microsphere n = 1.3, 1.35, 1.4 and 1.45. Based on the listed results, the imaging resolution increases monotonically with refractive index of the microsphere. The best obtained imaging resolution is ~ 0.38λ in the direction normal to the polarization which happens when n = 1.45. The improvement in resolution with refractive index of the microsphere can be attributed to solid immersion effect of the microsphere. The high refractive index of the microsphere, compared with air, results in the coupling of higher spatial frequency components ($\frac{2\pi}{\lambda} < k < \frac{2\pi n}{\lambda}$, where n is the refractive index of the sphere) from the emitter to the far field through the microsphere, thereby increasing the imaging resolution.

Table 6: Simulated FWHM of the PSF, magnification M, and the dipole resolution at the imaging plane of the microsphere based imaging system for different refractive index of the microsphere

n	FWHM of the PSF (parallel to polarization/normal to polarization)	M	Point Dipole spatial resolution (parallel to polarization/normal to polarization)	Point dipole spatial resolution in terms of λ (parallel to polarization/normal to polarization)
1.3	1.54 μm/1.32 μm	6.1	252 nm/216 nm	0.51λ/0.43λ
1.35	1.59 μm/1.33 μm	6.4	248 nm/208 nm	0.5λ/0.42λ
1.4	1.66 μm/1.38 μm	6.8	244 nm/203 nm	0.49λ/0.4λ
1.45	1.7 μm/1.4 μm	7.2	236 nm/194 nm	0.47λ/0.38λ

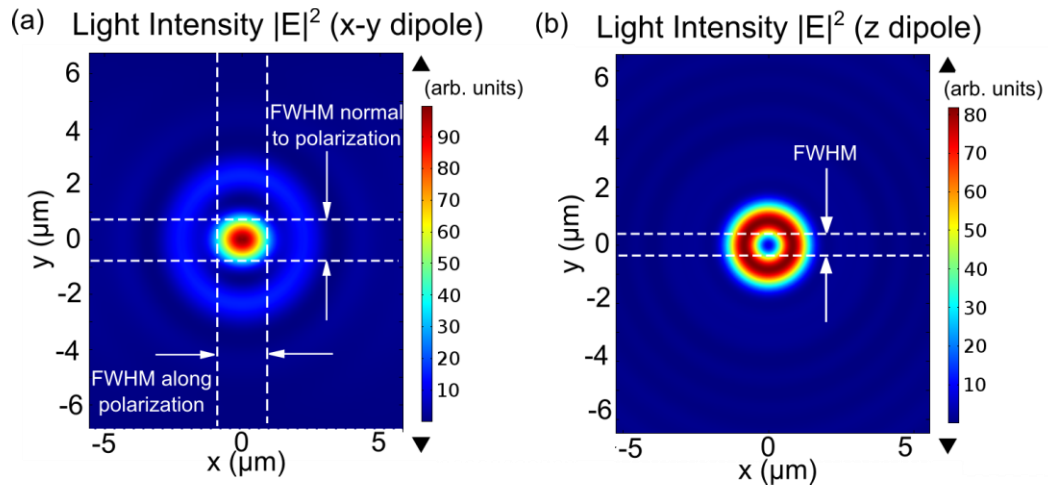

Figure 39 : Light intensity distribution at the image plane of (a) a transverse dipole (i.e., x-y dipole) and (b) a longitudinal dipole (i.e., z dipole)

6.3.2 Refractive index of base material of the target

Fused silica (FS) with refractive index 1.45 and aluminum oxide (AO) with refractive index 1.77, which are the two common target base materials in published microsphere imaging experiments, are selected in this portion of analysis to identity the contributions of the refractive index of the base material of the target in the imaging resolution with an

adjacent microsphere with n = 1.45 (close to fused silica). A lens pair is placed on top of the microsphere for generating real images on the image plane is as illustrated in Figure 38. A transverse dipole is again selected as a point source on the target as in the previous analysis. Each target has a thickness ~ 2λ to prevent the interference from the bottom surface of the target during the imaging process. Table 7 lists the simulated FWHM of the PSF, magnification M, and the dipole resolution at the imaging plane of the microsphere based imaging system when the transverse point dipole is placed on selected targets. For both AO and FS as the target material, the obtained dipole spatial resolution is better than that in air. Among AO and FS, AO with a higher refractive index provides a slightly better resolution for the transverse point dipoles placed on top of it. The improvement in the spatial resolution can be considered as an immersion effect when the microsphere, the point dipole and the target are almost in contact in the near field. The solid immersion effect from the target does not happen in regular far field imaging with macroscale lenses.

Table 7: Simulated FWHM of the PSF, magnification M, and the dipole resolution at the imaging plane of the microsphere based imaging system when the transverse point dipole is placed on different targets

Base material of Target	FWHM of the PSF (parallel to polarization/normal to polarization)	M	Point dipole spatial resolution (parallel to polarization/normal to polarization)	Point dipole spatial resolution in terms of λ (parallel to polarization/normal to polarization)
Air	1.73 μm/1.4 μm	7.2	236 nm/194 nm	0.47λ/0.38λ
AO	1.3 μm/1.19 μm	7.6	171 nm/156 nm	0.34λ/0.3λ
FS	1.56 μm/1.3 μm	7.4	210 nm/175 nm	0.42λ/0.35λ

6.3.3 Polarization of the emitter

In this portion of the analysis, a longitudinal dipole (or z-dipole) is selected as the emitter to be imaged by a microsphere of diameter ~ 6 μm and refractive index n = 1.45. The light emitted from a longitudinal dipole is a radially polarized beam similar to diffraction free

Bessel beams [128]. The light intensity distribution of the radially polarized beam has a doughnut shape at the focal/image spot with low numerical apertures (i.e. NA < 0.8) lenses. The doughnut shape intensity distribution arises due to the dominant transverse fields at low NA which have a phase singularity at the center of the beam [37]. For NA > 0.9, the longitudinal component is more dominant resulting in a central peak in the intensity distribution at the focus [129, 130]. Due to the low numerical aperture of most imaging lens, the PSF of a longitudinal dipole at the imaging plane has a symmetric doughnut shape intensity distribution. The FWHM of the doughnut shaped PSF is defined as FWHM of the central hole in the doughnut intensity distribution obtained at the imaging plane as indicated in Figure 39b. Table 8 lists the simulated FWHM of the PSF, magnification M, and the dipole resolution at the imaging plane of the microsphere based imaging system when the longitudinal point dipole is placed on selected targets (air, FS and AO). The imaging resolution of the longitudinal dipole with a microsphere follows the same trend as that with the transverse dipole i.e. the highest resolution occurs when the dipole is placed on the AO target (~ 0.24λ) due to the high refractive index and the associated stronger solid immersion effect. Compared with transverse point dipole, longitudinal point dipole provides better spatial resolution under the same microsphere and target conditions. The higher resolution with the longitudinal dipole can be attributed to the increased amplitude of higher spatial frequency components collected by the microsphere and the correspondingly larger effective collecting angle (Figure 38c) when it is compared with a transverse dipole (Figure 38b). Note that due to the smaller acceptance angle (< ~ 70°) of most far-field objective lens, the emission from the longitudinal dipole cannot be affectively captured with far-field macroscale lenses compared with near field microlenses as in the microsphere imaging.

Table 8: Simulated FWHM of the PSF, magnification M, and the dipole resolution at the imaging plane of the microsphere based imaging system when the longitudinal point dipole is placed on different targets

Base material of Target	FWHM of the PSF	Magnification (M)	Point dipole spatial resolution	Point dipole spatial resolution in terms of λ
Air	860 nm	6	143 nm	0.28λ
AO	790 nm	6.6	120 nm	0.24λ
FS	840 nm	6.4	131 nm	0.26λ

From the discussion in the above sections, it can be concluded that the best achievable resolution for incoherent point sources with dielectric microsphere of n = 1.45 and diameter ~ 6 μm is ~ 0.3λ for transverse point dipole and ~ 0.24λ for longitudinal point dipole on an AO target. The imaging resolution is not sensitive to the diameter but is sensitive to the refractive index of the microsphere. In a real imaging process, emitters are finite size nanostructures. Radiation from each location of a finite size nanostructure under reflected or transmitted illumination may not be incoherent as assumed in many publications. To verify the coherence of emission from finite size emitters, FEM simulation is conducted to study the electric field phase distribution in gold nanostructures of different widths. Two types of nanostructures are examined, namely, a thin film gold nanostructure of thickness ~ 30 nm (Figure 40a) and an elongated gold nanostructure (i.e., width much less than the thickness) of thickness ~ λ (Figure 40b), both of which are common nanostructures in microsphere imaging The nanostructures are exposed to linearly polarized illumination along the x-z plane from an external lens with a NA ~ 0.7. The nanostructures are ~ 1 μm before focal point of the external illumination to have a larger than 1 μm illumination region. The nanostructures are displaced ~ 250 nm away from the optical axis, which is around the middle between the center and the edge of the illumination region. For the thin film nanostructure with a thickness ~ 30 nm, it is observed from the simulation that the electric field inside the nanostructure is mainly in the transverse direction (i.e., $E_x > \sim 10E_z$) (Figure 40a). Also observed in the simulation is that

the electron oscillation inside the thin film gold nanostructure is almost spatially coherent (within 15 degree of phase lag [131]) when the width of the nanostructure is < ~ 0.2λ. Hence, the induced re-emission from a gold thin film nanostructure of width < ~ 0.2λ under an external illumination is similar to emission from a finite size transverse dipole with its length equal to the width of the nanostructure. Since the image spread function of a finite size transverse dipole with a length < ~ 0.2λ is equal to the point spread function of a point transverse dipole on the image plane (which can be understood from diffraction theory or from a direct FEM simulation as shown in Table 9), the image pattern of two thin film gold nanostructures with width less than 0.2λ is the same as two point transverse dipoles located at the center of the two thin film nanostructures. Therefore, for any gold thin film nanostructure with a width less than 0.2λ, the minimum resolvable center to center separation distance of the nanostructure on AO is ~ 0.3λ determined in Table 7. This statement can be used to explain the published microsphere imaging results with thin film gold nano-patterns [116, 120].

For the elongated nanostructure with a thickness ~λ, it is observed from the similar simulation that the electric field inside the nanostructure is mainly in the longitudinal direction (i.e. $E_z > \sim 5E_x$) (Figure 40b). The electron oscillation inside the elongated nanostructure is almost spatially coherent when the width of the nanostructure is < ~ 0.1λ. Hence, the induced re-emission from an elongated gold nanostructure of width < ~ 0.1λ under an external illumination is similar to emission from a finite size longitudinal dipole (with length equal to the thickness of the nanostructure). Since the image spread function of any finite size longitudinal dipole is equal to the point spread function of a point longitudinal dipole on the image plane (Table 9), the image pattern of two elongated gold nanostructures with width less than 0.1λ is the same as two point longitudinal dipoles located at the center of the two elongated nanostructures. Therefore, for any elongated gold nanostructure with a width less than 0.1λ, the minimum resolvable center to center separation distance of the nanostructure on AO is ~0.24λ determined in Table 8. This

statement may be used to explain the 50-100 nm resolution of gold coated anodized aluminum oxide (AAO) structures in previous experiments [113].

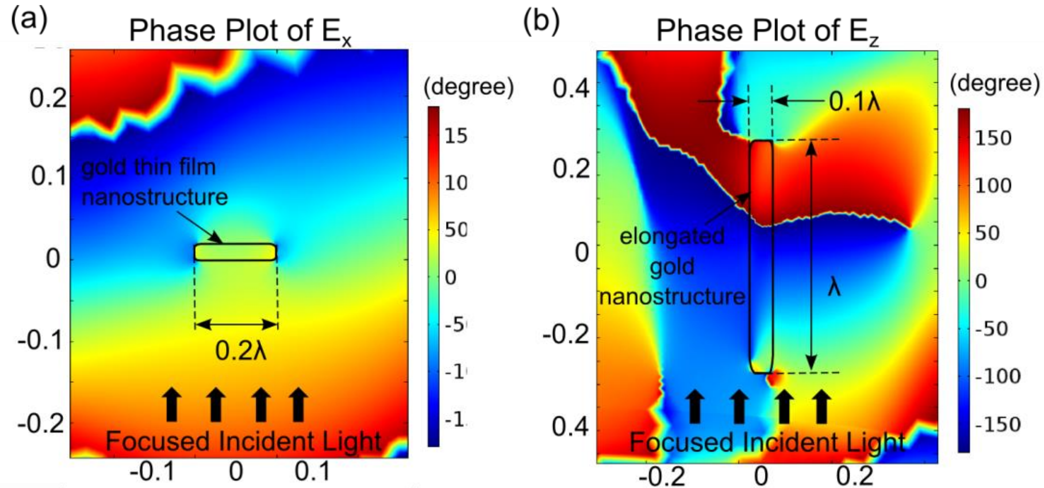

Figure 40: (a) Phase plot of x component of electric field when focused light (NA ~ 0.7) is incident on a gold thin film nanostructure with a width ~ 0.2 λ and thickness ~ 30 nm. (b) Phase plot of z component of electric field when focused light (NA ~ 0.7) is incident on an elongated gold nanostructure with a width ~ 0.1 λ and thickness ~ λ.

Table 9: Simulated FWHM of the PSF at the imaging plane of the microlens of refractive index n = 1.4 for transverse dipoles of different sizes

Polarization	Width of coherent region	FWHM of the PSF (parallel to polarization/normal to polarization)
Transverse	Point Dipole	1.66 µm/1.38 µm
	0.3λ	1.68 µm/1.42 µm
Longitudinal	Point dipole	895 nm
	0.3λ	905 nm

6.4 Summary

Compared with traditional microsphere imaging, microsphere images provides two main characteristics, namely, a highest possible acceptance angle (~90°) of the emission from the target as well as the contributions of the refractive index of the microsphere and the target in the imaging process. The highest spatial resolution for point sources on an AO target is ~ 0.3λ for transverse dipole and ~ 0.24λ for longitudinal dipole imaged with a fused silica microsphere. For finite size thin film nanostructures, when the width of the nanostructure is < ~ 0.2λ, the emission from the nanostructure is similar to a transverse point dipole located at the center of the nanostructure due to the highly coherent emission under reflected or transmitted illumination. Similarly, for finite elongated nanostructures, when the width of the nanostructure is < ~ 0.1λ, the emission from the nanostructure is similar to a longitudinal point dipole located at the center of the nanostructure. Therefore, the minimum resolvable center to center separation distance for thin film nano-patterns on AO is ~0.3λ (as point transverse dipoles) with a silica microsphere. The minimum resolvable center to center separation distance for elongated nano-patterns on AO is ~0.24λ (as point longitudinal dipoles) with the same silica microsphere.

7. CONCLUSIONS AND FUTURE WORK

7.1 Conclusions

There is a strong demand of nano-optical devices that can achieve deep-subwavelength spatial resolution with high energy throughput for optical based imaging and direct fabrication. In the past decade, nano-optic devices of different designs such as nano-apertures, scattering from metallic nano-structures and surface plasmons to achieve deep-sub wavelength light confinement have been proposed and studied by different groups. However, these existing devices suffer from several limitations such as vulnerability to high energy operation, low optical throughput and lower than expected spatial resolution. Among these three problems, vulnerability to high energy operation remains the most limiting factor in the application of nano-optic devices in nanoscale imaging and direct machining applications. A detailed study of the optical energy transport in nano-optic devices and the associated heat transfer mechanisms that occur can provide useful information for the future design of nano-optic devices, which is the motivation and beginning of this Ph.D. study that are better suited for high energy operation.

In the first part of this Ph.D study, the heating behavior of a commercially available nano-optic probe, NSOM, under pulsed laser operation with non-contact temperature measurement technique based on thermoreflectance method is studied. It is observed that under nanosecond pulsed illumination, degrading of the metal coating and the enlargement of the aperture size of the NSOM probes occurs. The damage of the thin metal coating of the NSOM probe is attributed to thermal stresses induced by joule heating of the metal coating and the resulting steep temperature gradients. Based on the conclusions from the transient thermal analysis of NSOM probes, in the subsequent of this Ph.D study, new optical probes are designed, that relieve some of the limitations observed in NSOM probes and are better suited for high energy pulsed operation.

The first probe examined is a diffraction-based binary phase plate consisting of transparent and opaque zones named micro-zone plate (MZP). The MZP optical probe has advantages of smaller joule heating, high optical throughput and long working distance compared with NSOM probes. The designed MZP is fabricated at the end face of an optical fiber with a newly developed fabrication methodology in this Ph.D study based on negative tone e-beam lithography. The focusing of light by the fabricated MZP is characterized with confocal laser scanning microscopy. The MZP can achieve spot sizes ~ 0.7λ at a focus distance of ~ 6λ with an optical transport efficiency of ~ 20 %, which is more than 3 orders higher than that of NSOM. MZP probes are suitable for fabrication and detection applications which require sub-wavelength resolution and long working distance such as biological imaging.

To further reduce the spot size to deep sub-wavelength scales, evanescent fields have to be included in light focusing. Two new optical probes made entirely of dielectric materials that can achieve deep sub-wavelength resolution are designed and constructed, namely, (a) solid immersion probe and (b) scattering dielectric probe. Both probes are constructed with micro/nano-optics stacked at the end face of an optical fiber to focus light by combining multiple mechanisms of light focusing with dielectric materials (such as reflection, solid immersion Mie scattering and near-field Rayleigh scattering). The solid immersion probe combines refraction and solid immersion focusing to achieve a diffraction-limited spot size of ~ 0.45λ/n on the surface of the microsphere with radially polarized illumination. A solid immersion probe composed with a ball lens (d ~ 29 μm) and microsphere (d ~ 3 μm) stacked on the end face of an optical fiber is constructed. The focusing characteristics of the solid immersion probe are characterized with confocal laser scanning microscopy and verified with numerical simulations. To further reduce the spot size, the scattering dielectric probe is proposed through combining the solid immersion based probe with Rayleigh scatterer. Numerical simulation is applied to optimize the shape of the dielectric scatterer that can achieve an intense nanoscale focus spot for radially polarized illumination. A corresponding teardrop scatterer composed with a large bottom

radius (r = 200 nm) and a small top radius (r = 10 nm) can serve as an efficient dielectric scatterer to achieve small spot size with high scattering intensity. It is verified with numerical simulations that the scattering dielectric probe that combines solid immersion and near-field Rayleigh scattering effects can achieve an intensity enhancement of ~ 10^5 with a ~10 nm spot size at the apex of the teardrop scatterer. Both dielectric probes in this study provide a significant improvement to commercially available NSOM probes in terms of spot size as well as optical throughput. Since the probes are constructed with dielectric material, they experience negligible joule heating during high energy operation. In addition, since the probes are designed and constructed on optical fibers, they can be easily integrated with commercial tuning-fork based scanning probe microscopy systems to achieve accurate position and fast scanning. The high optical throughput of these probes will ensure high signal to noise ratio with fast scanning speeds for nanoscale bio-microscopy, optical based fabrication and material manipulation (e.g., nano-optical tweezing) applications.

At the end of the Ph.D study, mechanisms for deep sub-wavelength imaging resolution with microspheres, which has been recently demonstrated by different groups, are identified with full wave electrodynamics simulations. It is found that the high spatial imaging resolution of point sources with microspheres can mainly be attributed to refractive index of the microsphere (i.e. solid immersion effect). In addition, the optical properties of the base material of the target beneath the point source also contribute to improvement in resolution through immersion effects. Further improvement in resolution can be achieved by considering longitudinal polarization of the emitter on the target plane. The highest spatial resolution of ~ 0.3λ is achieved for transverse point dipole (~0.24λ for longitudinal dipole) on an aluminum oxide target. In order to extend the imaging resolution achieved with point dipoles to real imaging of nanostructures, the spatial coherence of gold nanostructures under high focused illumination is studied. For finite size thin film nanostructures, the minimum resolvable center to center separation distance for thin film nano-patterns on AO is ~0.3λ (as point transverse dipoles) with a silica

microsphere. The minimum resolvable center to center separation distance for elongated nano-patterns on AO is ~0.24λ (as point longitudinal dipoles) with the same silica microsphere.

7.2 Future work

The current study can be extended in the following ways for future research:

1. The solid immersion and scattering dielectric probes can be coupled with nanoscecond pulsed lasers to perform nanoscale laser direct machining by ablation on semiconducting and metallic targets. The high energy throughput of the probes with negligible joule heating provides sufficient intensity at the focus spot to generate nanoscale plasma for applications in nanoscale laser spectroscopy.
2. A fabrication methodology has to be developed to generate the scatterer of desired shape for scattering dielectric probe. Once fabricated and assembled, the scattering dielectric probe can be applied for sub-20 nm spatial resolution in optical imaging with high signal to noise ratio compared with current apertureless NSOM systems. The high signal to noise ratio will be useful in high sensitivity biological and chemical detection such as tip-enhanced Raman spectroscopy (TERS).
3. The design of the scattering dielectric probe can be further improved to minimize the background noise by introducing a metallic scatterer at the apex, which is important in microscopy applications.
4. The developed standard procedure for precise fabrication of the end faces of optical fibers with e-beam lithography in Chapter 3 of this dissertation can be extended to fabricate surface plasmon resonators, localized plasmon resonators, photonic crystals and micro lenses at the end faces of optical fibers which have applications in optical-trapping and guiding, remote sensing, detection, optical processing and microscopy.

REFERENCES

[1] Novotny L and Hecht B 2012 *Principles of nano-optics* (Cambridge, UK: Cambridge University Press)

[2] Betzig E, Trautman J K, Harris T D, Weiner J S and Kostelak R L 1991 Breaking the diffraction barrier - Optical microscopy on a nanometric scale *Science* **251** 1468-70

[3] Grigoropoulos C P, Hwang D J and Chimmalgi A 2007 Nanometer-scale laser direct-write using near-field optics *Mrs Bull* **32** 16-22

[4] Hwang D J, Chimmalgi A and Grigoropoulos C P 2006 Ablation of thin metal films by short-pulsed lasers coupled through near-field scanning optical microscopy probes *J Appl Phys* **99** 044905

[5] Hwang D J, Jeon H and Grigoropoulos C P 2007 Laser ablation-induced plasma characteristics in optical near-field *Proceedings of the Asme/Jsme Thermal Engineering Summer Heat Transfer Conference 2007, Vol 2* 357-64

[6] Hwang D J, Grigoropoulos C P, Yoo J and Russo R E 2006 Optical near-field ablation-induced plasma characteristics *Appl Phys Lett* **89** 254101

[7] Herndon M K, Collins R T, Hollingsworth R E, Larson P R and Johnson M B 1999 Near-field scanning optical nanolithography using amorphous silicon photoresists *Appl Phys Lett* **74** 141-3

[8] Riehn R, Charas A, Morgado J and Cacialli F 2003 Near-field optical lithography of a conjugated polymer *Appl Phys Lett* **82** 526-8

[9] Zorba V, Mao X and Russo R E 2009 Laser wavelength effects in ultrafast near-field laser nanostructuring of Si *Appl Phys Lett* **95** 041110

[10] Betzig E and Trautman J K 1992 Near-field optics: Microscopy, spectroscopy, and surface modification beyond the diffraction limit *Science* **257** 189-95

[11] Zenobi R and Deckert V 2000 Scanning near-field optical microscopy and spectroscopy as a tool for chemical analysis *Angewandte Chemie International Edition* **39** 1746-56

[12] Hayazawa N, Inouye Y, Sekkat Z and Kawata S 2002 Near-field Raman imaging of organic molecules by an apertureless metallic probe scanning optical microscope *The Journal of Chemical Physics* **117** 1296-301

[13] Alkaisi M M, Blaikie R J, McNab S J, Cheung R and Cumming D R S 1999 Sub-diffraction-limited patterning using evanescent near-field optical lithography *Appl Phys Lett* **75** 3560-2

[14] Tarun A, Daza M R H, Hayazawa N, Inouye Y and Kawata S 2002 Apertureless optical near-field fabrication using an atomic force microscope on photoresists *Appl Phys Lett* **80** 3400-2

[15] Pan L, Park Y, Xiong Y, Ulin-Avila E, Wang Y, Zeng L, Xiong S M, Rho J, Sun C, Bogy D B and Zhang X 2011 Maskless plasmonic lithography at 22 nm Resolution *Scientific Reports* **1** 175

[16] Hartschuh A 2008 Tip-enhanced near-field optical microscopy *Angew Chem Int Edit* **47** 8178-91

[17] Chimmalgi A, Grigoropoulos C P and Komvopoulos K 2005 Surface nanostructuring by nano-/femtosecond laser-assisted scanning force microscopy *Journal of Applied Physics* **97** 104319

[18] Chimmalgi A, Choi T Y, Grigoropoulos C P and Komvopoulos K 2003 Femtosecond laser aperturless near-field nanomachining of metals assisted by scanning probe microscopy *Appl Phys Lett* **82** 1146-8

[19] Murphy-DuBay N, Wang L, Kinzel E C, Uppuluri S M V and Xu X 2008 Nanopatterning using NSOM probes integrated with high transmission nanoscale bowtie aperture *Optics Express* **16** 2584-9

[20] Liu Z W, Steele J M, Srituravanich W, Pikus Y, Sun C and X Z 2005 Focusing surface plasmons with a plasmonic lens *Nano Lett* **5** 1726-9

[21] Srisungsitthisunti P, Ersoy O K and Xu X F 2011 Improving near-field confinement of a bowtie aperture using surface plasmon polaritons *Appl Phys Lett* **98** 223106

[22] Maier S A 2007 *Plasmonics : fundamentals and applications* (New York, USA: Springer)

[23] Srituravanich W, Pan L, Wang Y, Sun C, Bogy D B and Zhang X 2008 Flying plasmonic lens in the near field for high-speed nanolithography *Nat Nanotechnol* **3** 733-7

[24] Steele J M, Liu Z W, Wang Y and Zhang X 2006 Resonant and non-resonant generation and focusing of surface plasmons with circular gratings *Optics Express* **14** 5664-70

[25] Novotny L and Hecht B 2006 *Principles of nano-optics* (New York, USA: Cambridge University Press)

[26] Wen S B 2010 Optical and thermal energy transport from a NSOM probe to a pure silicon target under intense ns pulsed light *J Phys D Appl Phys* **43** 285502

[27] Meenashi Sundaram V 2010 Direct nano-patterning with nano-optic devices *Master's thesis, Texas A&M University. Available electronically from http://hdl. handle. net/1969* **1**

[28] Sundaram V M, Soni A, Russo R E and Wen S B 2010 Analysis of nanopatterning through near field effects with femtosecond and nanosecond lasers on semiconducting and metallic targets *J Appl Phys* **107** 074305

[29] Meyer E, Jarvis S R and Spencer N D 2004 Scanning probe microscopy in materials science *Mrs Bull* **29** 443-8

[30] Huang F M, Chen Y, de Abajo F J G and Zheludev N I 2007 Optical super-resolution through super-oscillations *J Opt a-Pure Appl Op* **9** S285-S8

[31] Heifetz A, Kong S C, Sahakian A V, Taflove A and Backman V 2009 Photonic nanojets *Journal of Computational and Theoretical Nanoscience* **6** 1979-92

[32] Devilez A, Stout B, Bonod N and Popov E 2008 Spectral analysis of three-dimensional photonic jets *Optics Express* **16** 14200-12

[33] Hecht E 1998 *Optics* (Reading, Mass., USA: Addison-Wesley)

[34] Houston W V 1927 A compound interferometer for fine structure work *Phys Rev* **29** 0478-84

[35] Sparrow C M 1916 On spectroscopic resolving power *Astrophys J* **44** 76-86

[36] Potton R J 2004 Reciprocity in optics *Rep Prog Phys* **67** 717-54

[37] Quabis S, Dorn R, Eberler M, Glockl O and Leuchs G 2000 Focusing light to a tighter spot *Opt Commun* **179** 1-7

[38] Zhan Q W 2010 Magnetic field distribution of a highly focused radially-polarized light beam: comment *Opt Express* **18** 765-6

[39] Quabis S, Dorn R, Eberler M, Glockl O and Leuchs G 2001 The focus of light - theoretical calculation and experimental tomographic reconstruction *Appl Phys B-Lasers O* **72** 109-13

[40] Foreman M R and Torok P 2011 Computational methods in vectorial imaging *J Mod Optic* **58** 339-64

[41] Hwang D J, Jeon H, Grigoropoulos C P, Yoo J and Russo R E 2008 Laser ablation-induced spectral plasma characteristics in optical far- and near fields *J Appl Phys* **104** 013110

[42] Jahncke C L, Paesler M A and Hallen H D 1995 Raman imaging with near-field scanning optical microscopy *Appl Phys Lett* **67** 2483-5

[43] Wen S B, Greif R and Russo R E 2007 Background gas effects on the generation of nanopatterns on a pure silicon wafer with multiple femtosecond near field laser ablation *Appl Phys Lett* **91** 251113

[44] Soni A, Sundaram V M and Wen S B 2010 The generation of nano-patterns on a pure silicon wafer in air and argon with sub-diffraction limit nanosecond laser pulses *J Phys D Appl Phys* **43** 145301

[45] Schmitz T A, Gamez G, Setz P D, Zhu L and Zenobi R 2008 Towards nanoscale molecular analysis at atmospheric pressure by a near-field laser ablation ion trap/time-of-flight mass spectrometer *Anal Chem* **80** 6537-44

[46] Stockle R, Setz P, Deckert V, Lippert T, Wokaun A and Zenobi R 2001 Nanoscale atmospheric pressure laser ablation-mass spectrometry *Anal Chem* **73** 1399-402

[47] Wen S B and Greif R 2009 Combined wave based optical analysis and particle based thermal analysis of nanoscale ultrafast target heating of silicon utilizing a

near-field scanning optical probe and a femtosecond laser *Journal of Physics D-Applied Physics* **42** 075502

[48] Soni A and Wen S B 2012 Non-intrusive temperature measurement of NSOM probes with thermoreflectance imaging *J Phys D Appl Phys* **45** 185101

[49] Stockle R M, Schaller N, Deckert V, Fokas C and Zenobi R 1999 Brighter near-field optical probes by means of improving the optical destruction threshold *J Microsc-Oxford* **194** 378-82

[50] Kavaldjiev D I, Toledocrow R and Vaeziravani M 1995 On the heating of the fiber tip in a near-field scanning optical microscope *Appl Phys Lett* **67** 2771-3

[51] Farzaneh M, Maize K, Luerssen D, Summers J A, Mayer P M, Raad P E, Pipe K P, Shakouri A, Ram R J and Hudgings J A 2009 CCD-based thermoreflectance microscopy: principles and applications *J Phys D Appl Phys* **42** 143001

[52] Hong M H, Lin Y, Chen G X, Tan L S, Xie Q, Lukyanchuk B, Shi L P and Chong T C 2007 Nano-patterning by pulsed laser irradiation in near field *Cola'05: 8th International Conference on Laser Ablation* **59** 64-7

[53] Zorba V, Mao X L and Russo R E 2010 Optical far- and near-field femtosecond laser ablation of Si for nanoscale chemical analysis *Anal Bioanal Chem* **396** 173-80

[54] Zorba V, Mao X L and Russo R E 2009 Laser wavelength effects in ultrafast near-field laser nanostructuring of Si *Appl Phys Lett* **95** 041110

[55] Soni A, Sundaram V M and Wen S B 2013 A methodology for nanosecond (or better) time resolved thermoreflectance imaging with coherence control of laser pulses *Appl Phys Lett* **102** 203112

[56] Mayer P M, Luerssen D, Ram R J and Hudgings J A 2007 Theoretical and experimental investigation of the thermal resolution and dynamic range of CCD-based thermoreflectance imaging *J Opt Soc Am A* **24** 1156-63

[57] Tessier G, Hole S and Fournier D 2001 Quantitative thermal imaging by synchronous thermoreflectance with optimized illumination wavelengths *Appl Phys Lett* **78** 2267-9

[58] de Freitas L R, da Silva E C, Mansanares A M, Tessier G and Fournier D 2005 Sensitivity enhancement in thermoreflectance microscopy of semiconductor devices using suitable probe wavelengths *J Appl Phys* **98** 063508

[59] Dimitriou V, Kaselouris E, Orphanos Y, Bakarezos M, Vainos N, Tatarakis M and Papadogiannis N A 2013 Three dimensional transient behavior of thin films surface under pulsed laser excitation *Appl Phys Lett* **103** 114104

[60] Wang X and Xu X 2001 Thermoelastic wave induced by pulsed laser heating *Appl Phys a-Mater* **73** 107-14

[61] Özışık M N 1993 *Heat conduction* (New York, USA: Wiley)

[62] Palik E D and Ghosh G 1998 *Handbook of optical constants of solids* (San Diego, USA: Academic Press)

[63] Chen G and Hui P 2000 Thermal conductivities of evaporated gold films on silicon and glass (vol 74, pg 2942, 1999) *Appl Phys Lett* **76** 936

[64] Huang F M, Zheludev N, Chen Y F and de Abajo F J G 2007 Focusing of light by a nanohole array *Appl Phys Lett* **90**

[65] Rogers E T F and Zheludev N I 2013 Optical super-oscillations: sub-wavelength light focusing and super-resolution imaging *J Optics-Uk* **15** 094008

[66] Rogers E T F, Savo S, Lindberg J, Roy T, Dennis M R and Zheludev N I 2013 Super-oscillatory optical needle *Appl Phys Lett* **102** 031108

[67] Smythe E J, Dickey M D, Bao J M, Whitesides G M and Capasso F 2009 Optical antenna arrays on a fiber facet for in situ surface-enhanced Raman scattering detection *Nano Lett* **9** 1132-8

[68] Abouraddy A F, Bayindir M, Benoit G, Hart S D, Kuriki K, Orf N, Shapira O, Sorin F, Temelkuran B and Fink Y 2007 Towards multimaterial multifunctional fibres that see, hear, sense and communicate *Nat Mater* **6** 336-47

[69] Schonbrun E, Rinzler C and Crozier K B 2008 Microfabricated water immersion zone plate optical tweezer *Appl Phys Lett* **92** 071112

[70] Kim J, Jeong Y, Lee S, Ha W, Shin J S and Oh K 2012 Fourier optics along a hybrid optical fiber for Bessel-like beam generation and its applications in multiple-particle trapping *Opt Lett* **37** 623-5

[71] Camou S, Fujita H and Fujii T 2003 PDMS 2D optical lens integrated with microfluidic channels: principle and characterization *Lab Chip* **3** 40-5

[72] Menon R, Gil D and Smith H I 2006 Experimental characterization of focusing by high-numerical-aperture zone plates *J Opt Soc Am A* **23** 567-71

[73] Kim H C, Ko H and Cheng M S 2009 High efficient optical focusing of a zone plate composed of metal/dielectric multilayer *Opt Express* **17** 3078-83

[74] Callegari V, Iwaniuk D, Bronnimann R, Schmid E and Sennhauser U 2009 Optimized fabrication of curved surfaces by a FIB for direct focusing with glass fibres *J Micromech Microeng* **19** 107003

[75] Cabrini S, Liberale C, Cojoc D, Carpentiero A, Prasciolu M, Mora S, Degiorgio V, De Angelis F and Di Fabrizio E 2006 Axicon lens on optical fiber forming optical tweezers, made by focused ion beam milling *Microelectron Eng* **83** 804-7

[76] Petrusis A, Rector J H, Smith K, de Man S and Iannuzzi D 2009 The align-and-shine technique for series production of photolithography patterns on optical fibres *J Micromech Microeng* **19** 047001

[77] Fu Y Q and Bryan N K A 2005 Investigation of physical properties of quartz after focused ion beam bombardment *Appl Phys B-Lasers O* **80** 581-5

[78] Smythe E J, Dickey M D, Whitesides G M and Capasso F 2009 A technique to transfer metallic nanoscale patterns to small and non-planar surfaces *Acs Nano* **3** 59-65

[79] Schneider G F, Calado V E, Zandbergen H, Vandersypen L M K and Dekker C 2010 Wedging transfer of nanostructures *Nano Lett* **10** 1912-6

[80] Lipomi D J, Martinez R V, Kats M A, Kang S H, Kim P, Aizenberg J, Capasso F and Whitesides G M 2011 Patterning the tips of optical fibers with metallic nanostructures using nanoskiving *Nano Lett* **11** 632-6

[81] Viheriala J, Niemi T, Kontio J, Rytkonen T and Pessa M 2007 Fabrication of surface reliefs on facets of singlemode optical fibres using nanoimprint lithography *Electron Lett* **43** 150-2

[82] Scheerlinck S, Taillaert D, Van Thourhout D and Baets R 2008 Flexible metal grating based optical fiber probe for photonic integrated circuits *Appl Phys Lett* **92** 031104

[83] Lin Y B, Zou Y, Mo Y Y, Guo J P and Lindquist R G 2010 E-beam patterned gold nanodot arrays on optical fiber tips for localized surface plasmon resonance biochemical sensing *Sensors-Basel* **10** 9397-406

[84] Lin Y B, Zou Y and Lindquist R G 2011 A reflection-based localized surface plasmon resonance fiber-optic probe for biochemical sensing *Biomed Opt Express* **2** 478-84

[85] Yang H F, Jin A Z, Luo Q, Li J J, Gu C Z and Cui Z 2008 Electron beam lithography of HSQ/PMMA bilayer resists for negative tone lift-off process *Microelectron Eng* **85** 814-7

[86] Magdenko L, Gaucher F, Aassime A, Vanwolleghem M, Lecoeur P and Dagens B 2009 Sputtered metal lift-off for grating fabrication on InP based optical devices *Microelectron Eng* **86** 2251-4

[87] Tao J R, Chen Y F, Zhao X Z, Malik A and Cui Z 2005 Room temperature nanoimprint lithography using a bilayer of HSQ/PMMA resist stack *Microelectron Eng* **78-79** 665-9

[88] Liao Y H, Angelopoulos M and Levon K 1995 Ring-substituted polyaniline copolymers combining high solubility with high-conductivity *J Polym Sci Pol Chem* **33** 2725-9

[89] Sundaram V M and Wen S B 2011 An easy method to perform e-beam negative tone lift-off fabrication on dielectric material with a sandwiched conducting polymer layer *J Micromech Microeng* **21** 065021

[90] Kelkar P S, Beauvais J, Lavallee E, Drouin D, Cloutier M, Turcotte D, Yang P, Mun L K, Legario R, Awad Y and Aimez V 2004 Nano patterning on optical fiber and laser diode facet with dry resist *J Vac Sci Technol A* **22** 743-6

[91] Liu Y X, Xu H, Stief F, Zhitenev N and Yu M 2011 Far-field superfocusing with an optical fiber based surface plasmonic lens made of nanoscale concentric annular slits *Opt Express* **19** 20233-43

[92] Verslegers L, Catrysse P B, Yu Z F, White J S, Barnard E S, Brongersma M L and Fan S H 2009 Planar lenses based on nanoscale slit arrays in a metallic film *2009 Conference on Lasers and Electro-Optics and Quantum Electronics and Laser Science Conference (Cleo/Qels 2009), Vols 1-5* 3224-5

[93] Gil D, Menon R and Smith H I 2003 Fabrication of high-numerical-aperture phase zone plates with a single lithography exposure and no etching *J Vac Sci Technol B* **21** 2956-60

[94] Chen Z G, Taflove A and Backman V 2004 Photonic nanojet enhancement of backscattering of light by nanoparticles: a potential novel visible-light ultramicroscopy technique *Optics Express* **12** 1214-20

[95] Lecler S, Takakura Y and Meyrueis P 2005 Properties of a three-dimensional photonic jet *Opt Lett* **30** 2641-3

[96] Itagi A V and Challener W A 2005 Optics of photonic nanojets *Journal of the Optical Society of America a-Optics Image Science and Vision* **22** 2847-58

[97] Devilez A, Bonod N, Wenger J, Gerard D, Stout B, Rigneault H and Popov E 2009 Three-dimensional subwavelength confinement of light with dielectric microspheres *Optics Express* **17** 2089-94

[98] Kim M S, Scharf T, Muhlig S, Rockstuhl C and Herzig H P 2011 Engineering photonic nanojets *Optics Express* **19** 10206-20

[99] Theppakuttai S and Chen S C 2004 Submicron ripple formation on glass surface upon laser-nanosphere interaction *Journal of Applied Physics* **95** 5049-52

[100] Battula A, Theppakuttai S and Chen S C 2006 Direct, parallel nanopatterning of silicon carbide by laser nanosphere lithography *Journal of Microlithography Microfabrication and Microsystems* **5** 011009

[101] Lee J Y, Hong B H, Kim W Y, Min S K, Kim Y, Jouravlev M V, Bose R, Kim K S, Hwang I C, Kaufman L J, Wong C W, Kim P and Kim K S 2009 Near-field focusing and magnification through self-assembled nanoscale spherical lenses *Nature* **460** 498-501

[102] McCloskey D, Wang J J and Donegan J F 2012 Low divergence photonic nanojets from Si3N4 microdisks *Optics Express* **20** 128-40

[103] Liu Z W, Lee H, Xiong Y, Sun C and Zhang X 2007 Far-field optical hyperlens magnifying sub-diffraction-limited objects *Science* **315** 1686

[104] Bhushan B 2010 *Scanning probe microscopy in nanoscience and nanotechnology* (Berlin, Germany: Springer)

[105] Bennett B, Goldberg S, Ippolito B, Novotny L, Liu Z H and Unlu M S 2002 Immersion lens microscopy of photonic nanostructures and quantum dots *Ieee J Sel Top Quant* **8** 1051-9

[106] Duocastella M and Arnold C B 2012 Bessel and annular beams for materials processing *Laser Photonics Rev* **6** 607-21

[107] Watanabe T, Fujii M, Watanabe Y, Toyama N and Iketaki Y 2004 Generation of a doughnut-shaped beam using a spiral phase plate *Rev Sci Instrum* **75** 5131-5

[108] Mishra S R 1991 A vector wave analysis of a bessel beam *Opt Commun* **85** 159-61

[109] Bohren C F and Huffman D R 1983 *Absorption and scattering of light by small particles* (New York, USA: Wiley)

[110] Gouesbet G, Lock J A and Grehan G 2011 Generalized Lorenz-Mie theories and description of electromagnetic arbitrary shaped beams: Localized approximations and localized beam models, a review *J Quant Spectrosc Ra* **112** 1-27

[111] Sundaram V M and Wen S B 2014 Nanoscale high-intensity light focusing with pure dielectric nonspherical scatterer *Opt Lett* **39** 582-5

[112] Siegel R and Howell J R 1992 *Thermal radiation heat transfer* (Washington, D.C., USA: Hemisphere Pub. Corp.)

[113] Wang Z B, Guo W, Li L, Luk'yanchuk B, Khan A, Liu Z, Chen Z C and Hong M H 2011 Optical virtual imaging at 50 nm lateral resolution with a white-light nanoscope *Nat Commun* **2** 218

[114] Hao X, Kuang C F, Liu X, Zhang H J and Li Y H 2011 Microsphere based microscope with optical super-resolution capability *Appl Phys Lett* **99** 203102

[115] Vlad A, Huynen I and Melinte S 2012 Wavelength-scale lens microscopy via thermal reshaping of colloidal particles *Nanotechnology* **23** 285708

[116] Darafsheh A, Walsh G F, Dal Negro L and Astratov V N 2012 Optical super-resolution by high-index liquid-immersed microspheres *Appl Phys Lett* **101** 141128

[117] Lee S, Li L, Wang Z B, Guo W, Yan Y Z and Wang T 2013 Immersed transparent microsphere magnifying sub-diffraction-limited objects *Appl Optics* **52** 7265-70

[118] Yan Y Z, Li L, Feng C, Guo W, Lee S and Hong M H 2014 Microsphere-coupled scanning laser confocal nanoscope for sub-diffraction-limited imaging at 25 nm lateral resolution in the visible spectrum *Acs Nano* **8** 1809-16

[119] Hao X, Kuang C F, Gu Z T, Wang Y F, Li S A, Ku Y L, Li Y H, Ge J H and Liu X 2013 From microscopy to nanoscopy via visible light *Light-Sci Appl* **2** 108

[120] Darafsheh A, Limberopoulos N I, Derov J S, Walker D E and Astratov V N 2014 Advantages of microsphere-assisted super-resolution imaging technique over solid immersion lens and confocal microscopies *Appl Phys Lett* **104** 061117

[121] Ghislain L P and Elings V B 1998 Near-field scanning solid immersion microscope *Appl Phys Lett* **72** 2779-81

[122] Ghislain L P, Elings V B, Crozier K B, Manalis S R, Minne S C, Wilder K, Kino G S and Quate C F 1999 Near-field photolithography with a solid immersion lens *Appl Phys Lett* **74** 501-3

[123] Mansfield S M and Kino G S 1990 Solid immersion microscope *Appl Phys Lett* **57** 2615-6

[124] Duan Y B, Barbastathis G and Zhang B L 2013 Classical imaging theory of a microlens with super-resolution *Opt Lett* **38** 2988-90

[125] Ye R, Ye Y H, Ma H F, Cao L L, Ma J, Wyrowski F, Shi R and Zhang J Y 2014 Experimental imaging properties of immersion microscale spherical lenses *Sci Rep-Uk* **4** 3769

[126] Yang H, Moullan N, Auwerx J and Gijs M A M 2014 Super-resolution biological microscopy using virtual imaging by a microsphere nanoscope *Small* **10** 1712-8

[127] den Dekker A J and van den Bos A 1997 Resolution: a survey *J. Opt. Soc. Am. A* **14** 547-57

[128] Zhan Q W 2009 Cylindrical vector beams: from mathematical concepts to applications *Adv Opt Photonics* **1** 1-57

[129] Sheppard C J R and Choudhury A 2004 Annular pupils, radial polarization, and superresolution *Appl Optics* **43** 4322-7

[130] Youngworth K S and Brown T G 2000 Focusing of high numerical aperture cylindrical-vector beams *Opt Express* **7** 77-87

[131] Chartier G 2005 *Introduction to optics* (New York, USA: Springer)

APPENDIX

Scattering of light by dielectric spheres (Lorentz – Mie theory)

The theory of absorption and scattering of light by dielectric spheres can be solved using Mie theory. The mathematical basis of Mie theory will be explained briefly in this section. We begin with the Helmholtz equations for an electromagnetic wave in a homogeneous medium which are given by

$$\nabla^2 \vec{E} + k^2 \vec{E} = 0, \text{ and } \nabla^2 \vec{H} + k^2 \vec{H} = 0, \tag{18}$$

where $\vec{E}$ and $\vec{H}$ are the electric and magnetic fields respectively and k is the wave number such that $k^2 = \omega^2 \varepsilon \mu$ with ε , the permittivity , μ the permeability of the medium and ω is the frequency of the incident light. Note that $\vec{E}$ and $\vec{H}$ are divergence free and are related by the curl Maxwell equations. Consider a scalar function ψ and a constant $\vec{c}$ with which we construct a vector function given by

$$\vec{M} = \nabla \times \left(\vec{c} \psi \right). \tag{19}$$

It can be shown that $\vec{M}$ satisfies

$$\begin{aligned} &\nabla . \vec{M} = 0, \\ &\nabla^2 \vec{M} + k^2 \vec{M} = \nabla \times \left[\vec{c} \left(\nabla^2 \psi + k^2 \psi \right) \right]. \end{aligned} \tag{20}$$

Therefore, if ψ satisfies the scalar wave equation $\nabla^2 \psi + k^2 \psi = 0$, then $\vec{M}$ satisfies the vector wave equation and $\vec{M} = -\vec{c} \times \nabla \psi$ which shows that $\vec{M}$ is perpendicular to $\vec{c}$. If we construct another function from $\vec{M}$ given by

$$\vec{N} = \frac{\nabla \times \vec{M}}{k}, \tag{21}$$

we can show that $\vec{N}$ also satisfies the wave equation $\nabla^2 \vec{N} + k^2 \vec{N} = 0$ and $\nabla \times \vec{N} = k\vec{M}$. Based on the above discussion it can be seen that $\vec{M}$ and $\vec{N}$ satisfy the vector wave equations, are divergence free and the curls of each is related to the other in the same way as $\vec{E}$ and $\vec{H}$ in the Maxwell's equations. Therefore the problem of solving the Maxwell's equations has been reduced to finding the solution to the scalar wave equation

$\nabla^2\psi + k^2\psi = 0$. Here ψ is called the generating function for vector harmonics $\vec{M}$ and $\vec{N}$. Since the Mie theory is used to solve for scattering of an electromagnetic wave by a sphere we consider $\psi(r,\theta,\phi)$ to satisfy the wave equation in spherical coordinates. Also the constant $\vec{c}$ is taken to be the radius vector $\vec{r}$. The solution to the scalar wave equation for $\psi(r,\theta,\phi)$ in spherical coordinates can be even or odd and id given by

$$\begin{aligned}\psi_{emn} &= \cos m\phi P_n^m(\cos\theta) z_n(kr),\\ \psi_{omn} &= \sin m\phi P_n^m(\cos\theta) z_n(kr),\end{aligned} \tag{22}$$

where m, n are the eigenvalues, z_n can be any of the four spherical Bessel functions $j_n, y_n, h_n^{(1)}$ or $h_n^{(2)}$ and $P_n^m(\cos\theta)$ is the associated Legendre polynomial. From the scalar solution we can obtain four vector spherical harmonics as

$$\begin{aligned}M_{emn} &= \nabla\times\left(\vec{r}\psi_{enm}\right),\ M_{omn} = \nabla\times\left(\vec{r}\psi_{onm}\right)\\ N_{emn} &= \frac{\nabla\times M_{emn}}{k},\ M_{omn} = \frac{\nabla\times M_{omn}}{k}.\end{aligned} \tag{23}$$

Any solution to the wave equation can now be expanded in terms of infinite series of the above four vector spherical harmonics.

Now, if we consider a plane wave polarized in the x direction incident on a dielectric sphere of radius *a* and refractive index *n*, the incident plane wave in spherical coordinates can be written as

$$\vec{E}_i = E_0 e^{ikr\cos\theta}\hat{e}_x, \tag{24}$$

where $\hat{e}_x = \sin\theta\cos\phi\hat{e}_r + \cos\theta\cos\phi\hat{e}_\theta + \sin\phi\hat{e}_\phi$. As discussed in the previous paragraph, the incident field which satisfies the vector wave equation can be expressed as a summation of the vector spherical harmonics as

$$\vec{E}_i = \sum_{m=0}^{\infty}\sum_{n=m}^{\infty}\left(B_{emn}M_{emn} + B_{omn}M_{omn} + A_{emn}N_{emn} + A_{omn}N_{omn}\right), \tag{25}$$

where the coefficients B_{emn}, B_{omn}, A_{emn}, and A_{omn} have to be determined from the incident field. By using the orthogonality property of vector spherical harmonics i.e.

(M_{emn}, M_{omn}), (N_{emn}, N_{omn}), (M_{emn}, N_{emn}) and (M_{omn}, N_{omn}) are mutually orthogonal and the known incident field in eq. 24 the coefficients B_{emn}, B_{omn}, A_{emn}, and A_{omn} can be determined. Thus, the expansion of the incident field E_i for an x-polarized plane wave is obtained as,

$$\vec{E}_i = E_0 \sum_{n=1}^{\infty} i^n \frac{(2n+1)}{n(n+1)} \left(\vec{M}_{01n}^{(1)} - i\vec{N}_{e1n}^{(1)} \right), \tag{26}$$

where the superscript (1) is used to indicate that the spherical Bessel function j_n is used for radial dependence denoted by z_n in eq 22. In a similar fashion the scattered field $\vec{E}_s$ and the internal field inside the sphere $\vec{E}_1$ can also be expressed in vector spherical harmonics as

$$\begin{aligned} \vec{E}_1 &= \sum_{n=1}^{\infty} E_n \left(c_n \vec{M}_{01n}^{(1)} - i d_n \vec{N}_{e1n}^{(1)} \right), \\ \vec{E}_s &= \sum_{n=1}^{\infty} E_n \left(-b_n \vec{M}_{01n}^{(3)} + i a_n \vec{N}_{e1n}^{(3)} \right), \end{aligned} \tag{27}$$

where the superscript (3) is used for the scattered field to indicate that the spherical Bessel function $h_n^{(1)}$ of is used for the radial dependence since both j_n and y_n are well behaved outside the sphere region where $r > 0$. The coefficients a_n, b_n, c_n and d_n are known as the scattering coefficients and can be obtained by applying the Maxwell boundary conditions for the electric and magnetic field at the boundary of the sphere i.e. $r = a$.

Since we have determined all the coefficients for the incident, scattered and internal fields, the field distribution around the cylinder can be obtained by plotting the internal filed in the region inside the sphere ($r < a$) and the summation of the scattered and incident field in the region outside the sphere ($r > a$).

Experimental techniques for characterization of light focusing devices

Two different methods were used to experimentally determine the light focusing characteristics of the scanning optical probes developed in this study, namely, (a) confocal laser scanning microscopy (CSLM), and (b) collection mode NSOM imaging. A detailed description of the experimental setup for each of these methods is provided in this section.

Confocal laser scanning microscopy

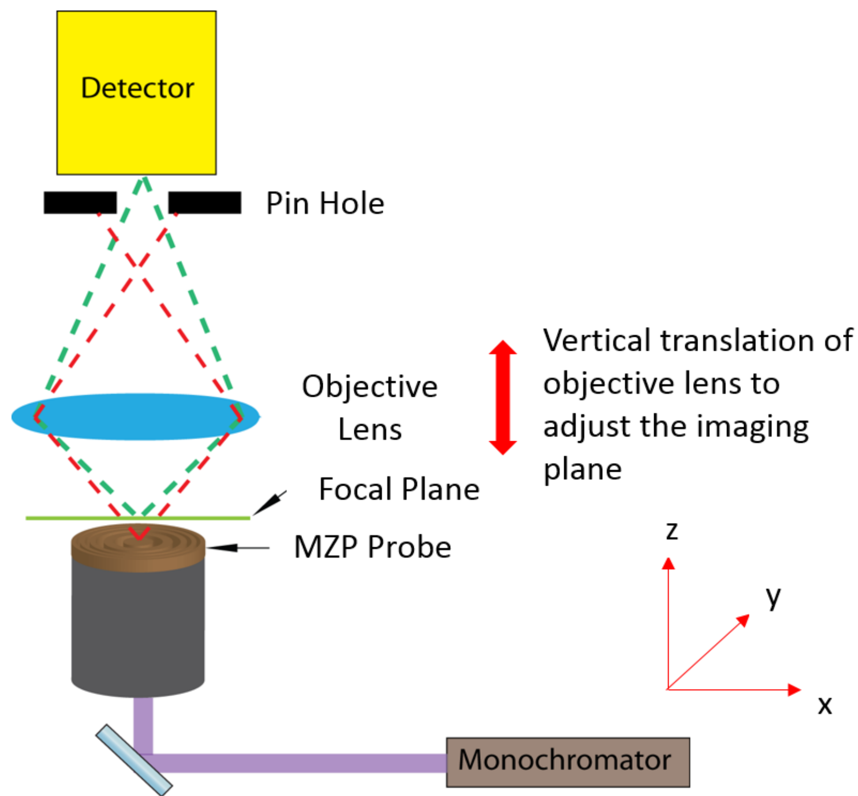

Figure 41: Schematic of experimental setup for characterization of light focusing by MZP probe with confocal laser scanning microscopy.

A modified version of the traditional CSLM can be applied as a useful technique to experimentally characterize the focusing of light by optical probes such as the MZP and

scattering dielectric probe developed in this study. A schematic of the setup is shown in Figure 41. Light is coupled to the MZP optical probe which is mounted on the xy-translation stage of the CSLM. The CSLM is operated in reflection mode. Note that the lasers available in CSLM do not have to be used in this measurement since the light source for the imaging is the light emitted from the MZP probe. By adjusting the position of the objective lens in the z-direction, the location of the imaging plane can be changed. The thickness of the imaging plane (i.e. the axial resolution of the CSLM) is determined by the size of the pin hole that is used in the imaging process. In this study, the pin hole size was set to about half of the Airy disc size resulting in a z-resolution of ~ 600 nm. In order to image the light focusing by the MZP, the xy-scanning images are obtained from the surface of the MZP to ~ 10 μm from the surface in steps of 200 nm. The xy scanning images at the approximate focal length of the optical probe are used to calculate the focus spot size. The xy scanning images can also be stacked together and rotated to obtain the xz or yz profile of light focusing which can be used to determine the approximate focal length of the optical probe.

While the CSLM offers advantages in terms of fast scanning to image the light focusing by optical probes, the lateral imaging resolution is limited by the classical diffraction limit. As a result CSLM is not suitable for more accurate characterization of focus spot sizes for nano-optical devices with sub-diffraction limit spatial resolution. In the next section we describe another technique based on NSOM probes that scans the near-field to characterize the light focusing.

Collection-mode NSOM imaging

In collection mode NSOM imaging, the light emitted from the light focusing device (MZP is Figure 42) is imaged by raster scanning the NSOM probe along the xy plane at a fixed distance from the MZP. The NSOM probe measures the light intensity at each point in the xy plane with the help of a single photon counting module consisting of an avalanche photo-detector (APD) or a photo multiplies tube (PMT). Since the scanning speed of the

NSOM probe is typically about 3-5 s/line, each scan is very slow compared with the CSLM. The spatial resolution of this imaging method is limited by the aperture size of the NSOM probe which can be as small as 100 nm.

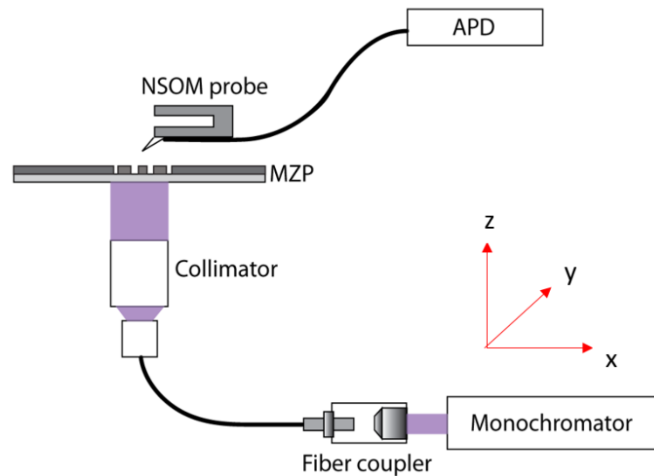

Figure 42: Schematic of experimental setup for characterization of light focusing by MZP probe with collection mode NSOM imaging.

A combination of both methods, namely CSLM and collection mode NSOM can be a very useful tool for characterization of light focusing devices. The CSLM, with its fast scanning, provides the approximate focal length of the light focusing device while the collection mode NSOM, with its sub-diffraction limit spatial resolution, can be used to scan the focal plane to determine the exact spot size at the focus.